GKSS FORSCHUNGSZENTRUM in der HELMHOLTZ GEMEINSCHAFT

Friction Hydro Pillar Processing

Bonding Mechanism and Properties

(Von der Gemeinsamen Fakultät für Maschinenbau und Elektrotechnik der Technischen Universität Carolo-Wilhelmina zu Braunschweig als Dissertation angenommene Arbeit)

Author:

A. Meyer

ISSN 0344-9629

GKSS 2003/4

GKSS 2003/4

Friction Hydro Pillar Processing

Bonding Mechanism and Properties

(Von der Gemeinsamen Fakultät für Maschinenbau und Elektrotechnik der Technischen Universität Carolo-Wilhelmina zu Braunschweig als Dissertation angenommene Arbeit)

Author:

A. Meyer

(Institute for Materials Research)

GKSS-Forschungszentrum Geesthacht GmbH • Geesthacht • 2003

ISSN 0344-9629

GKSS-Forschungszentrum Geesthacht GmbH · Telefon (04152)87-0
Max-Planck-Straße · D-21502 Geesthacht / Postfach 11 60 · D-21494 Geesthacht

GKSS 2003/4

Friction Hydro Pillar Processing – Bonding Mechanism and Properties

(Von der Gemeinsamen Fakultät für Maschinenbau und Elektrotechnik der Technischen Universität Carolo-Wilhelmina zu Braunschweig als Dissertation angenommene Arbeit)

Axel Meyer

132 pages with 131 figures and 26 tables

Abstract

Life extension of engineering structures and large industrial components is a major issue for operators and contractors particularly in the energy and transportation sectors. As a result safe and cost effective repair measures are continuously being sought. Portable friction welding machines and new friction welding repair methods made ”in-situ” solid-state repair technology possible for industrial applications. The method in question is called Friction Hydro Pillar Processing (FHPP) and involves drilling a hole in the crack and filling it by a rotating consumable stud producing a friction weld. Longer cracks are repaired by producing a series of such welds overlapping each other (called friction stitch welding). However, the introduction of such a repair technique to actual applications requires a systematic description of the mechanisms controlling bonding as well as information on the microstructural development and performance of repair welds.

In the present work a large experimental matrix associated to elaborate experimental techniques has been used to describe the mechanisms leading to bonding in FHPP welds. Furthermore, extensive mechanical testing has been carried out in order to describe the bonding quality and the performance of friction stitch welds. The welds have been performed using a hydraulic powered friction welding machine, originally designed and built as a portable stud welding unit, delivering up to 40 kN welding force and 8000 rpm. All welds were monitored, analysed and evaluated using a purpose built data recording system. API 5L X-65 and S235 steel grades have been used in the experimental programme, whereby the respective studs have been machined out of the corresponding base material.

The results obtained in the course of this study have shown that the hole shape, rather than the stud geometry has a major influence in achieving bonding all around the joint. The influence of process parameters on heat generation and bonding quality are similar to that know from conventional friction welding. However, forging force has been shown to have a limited influence on FHPP welds. It could be demonstrated that the shape of the frictional plane defines the distribution of the axial force and the temperature development in a weld. Pressure measurements revealed that bonding takes place at lower compressive forces than expected.

The microstructure of friction stitch welds in a structural steel (S235) consisted of martensitic structures around the bonding line surrounded by mostly acicular ferrite and ferrite with aligned second phase. This microstructure was reflected in the hardness profiles in which approximately 350 HV have been measured at the bonding line whereas the remaining of the joint showed values around 200 HV. These values are substantially reduced by the re-heat treatment imposed through subsequent welds. Transverse tensile testing confirmed the overmatching condition while failures taking place always in the base material. Toughness results in the stud material and at the bonding line were inferior to the base metal. These values however are very much dependent on the weld sequence and depicts worst case conditions.

Friction Hydro Pillar Processing – Bindemechanismen und Eigenschaften

Zusammenfassung

Die Verlängerung der Lebensdauer industrieller Bauwerken ist von übergeordneter Bedeutung für die Betreiber und Hersteller, insbesondere in der Energie- und Transportindustrie. Daher werden ständig neue, sichere und kostengünstige Reparaturverfahren für diese Anwendungsfälle gesucht. Tragbare Reibschweißmaschinen und neue Reibschweiß-Reparaturverfahren machen eine Vor-Ort-Reparatur industrieller Anlagen mit Reibschweißverfahren mittlerweile möglich. Ein in Frage kommendes Verfahren ist das “Friction Hydro Pillar Processing” (FHPP), wobei zunächst ein Sackloch in einen vorhandenen Riss gebohrt wird, welches anschließend mit einem rotierenden Bolzen in einer Reibschweißung verfüllt wird. Ausgedehnte Defekte werden mit Hilfe von überlappend ausgeführten Einzelschweißungen repariert (Friction Stitch Welding). Die industrielle Umsetzung dieses Verfahrens erfordert jedoch noch eine systematische Beschreibung der Bindungsvorgänge, sowie Informationen über die mikrostrukturelle Entwicklung und das Verhalten der Reparaturnähte.

Relevante Prozessvorgänge, Zusammenhänge und Einflussgrößen wurden in der vorliegenden Arbeit mit Hilfe umfangreicher experimenteller Untersuchungen aufgezeigt und beschrieben. Zusätzlich wurden die Bindungsqualität und die Eigenschaften von Schweißnähten (Stitch Welding) experimentell bestimmt. Die Schweißungen wurden mit einer hydraulischen Reibschweißmaschine durchgeführt. Dieses System wurde ursprünglich als tragbare Maschine für das Reib-Bolzenschweißen entwickelt und bietet bis zu 40 kN Reibkraft bei maximal 8000 Umdrehungen pro Minute. Beim Fügen wurden alle relevanten Einflussgrößen überwacht und mit einer speziell entwickelten Datenerfassung zur anschließenden Auswertung aufgezeichnet. Für die Schweißversuche wurden Stähle der Güten API 5L X65 und S235 verwendet, wobei die Schweißbolzen jeweils aus dem selben Werkstoff hergestellt wurden.

Die Ergebnisse dieser Arbeit zeigen, dass vornehmlich die Lochform und nicht so sehr die Bolzenform für eine vollständige Bindung verantwortlich ist. Der Einfluss der Schweißparameter auf die Temperaturentwicklung und die Verbindungsqualität ist grundsätzlich vergleichbar mit dem konventionellen Reibschweißen. Jedoch hat sich gezeigt, dass die Schmiedekraft beim FHPP kaum Einfluss besitzt. Es konnte des Weiteren nachgewiesen werden, dass die Form der Reibfläche sowohl für die Verteilung der axialen Reibkraft, als auch für die Temperaturverteilung während der Schweißung verantwortlich ist. Kraftmessungen in der Bindelinie belegen eine Verbindungsbildung bei niedrigeren Kräften als erwartet.

Die Mikrostruktur von Verbindungen in S235 zeigt martensitische Strukturen im Bereich der Bindelinie mit hauptsächlich nadelförmigem Ferrit und Bainit. Diese Mikrostruktur spiegelt sich auch in den Härtemessungen wieder. Es wurden bis zu 350 HV in Bereich der Bindelinie, sowie 200 HV im restlichen Schweißgut gemessen. Diese Werte konnten beim Stitch Welding durch die erneute Erwärmung des Werkstoffes während der folgenden Schweißungen deutlich reduziert werden.

Querzugversuche bestätigen die höhere Festigkeit des Schweißgutes, wodurch alle Proben im unbeeinflussten Grundwerkstoff versagten. Zähigkeitsuntersuchungen in der Mitte der Naht und in der Bindelinie zeigten geringere Werte als im Grundwerkstoff. Diese Werte weisen jedoch eine hohe Abhängigkeit von der gewählten Schweißfolge auf und wurden in dieser Arbeit nicht gezielt optimiert.

Manuscript received / Manuskripteingang in TDB: 4. März 2003

ACKNOWLEDGEMENTS

Fist of all I would like express my gratitude to Prof. H. Wohlfahrt and Prof. K.-H. Schwalbe for the supervision and appraisal of this work.

I am in debt to GKSS-Forschungszentrum for having offered me the opportunity to perform this research work and in particular to Jorge F. dos Santos for his continuous support, valuable discussions, detailed prove reading and complete confidence in this process and in myself.

I had many useful discussions with a number of colleagues and I should especially like to acknowledge Dirk Pauly and Christoph Schilling, as well as Olav Vennemann and Gustavo Pinheiro. I should particularly like to thank Alexander von Strombeck for his great support with technical drawings, illustrations and many discussions.

I have also received considerable assistance from Petra Fischer and Walli-Vera Schmitz of the GKSS metallographic laboratory, and from Herbert Rosomm, Frank Nickel and Henning Lohmann of the workshop and design departments.

Above all, however, I should like to thank all my colleagues from the Joining Technology Group at GKSS for their support and many stimulating discussions. In addition, I am grateful to Marcelo T. Piza Paes from Petrobras/Cenpes for the support on the microstructural characterisation.

I am in debt to Dr. Frank Hanus and Jürgen Schütz from AG der Dillinger Hüttenwerke for the donation of base materials. I would also like to express my gratitude to Dave Dent and Gordon Blakemore from Circle Technical Services for the ability to use their welding system throughout the whole work, for their support in upgrading and modifying this system as well as for useful discussions. My appreciation also goes to Dave Gibson from NHC for the his continuous support and his efforts to apply the results of this work to industrial applications.

Last but not least, I am grateful to Sigrid Schöttle for her indulgence during all the long weekends and even longer working hours in the last years and my parents for their continuous support throughout this work.

TABLE OF CONTENTS

LIST OF ABBREVIATIONS

AC	Ferrite with aligned MAC
AF	Acicular ferrite
AWS	American Welding Society
DIN	German National Standard
DNV	Det Norske Veritas
DRS	Data Recording System
F	Primary Ferrite
FC	Ferrite-carbide aggregate
FHPP	Friction Hydro Pillar Processing
GF	Grain boundary ferrite
HAZ	Heat Affected Zone
HSLA	High Strength Low Alloy
LC	Load Cell
M	Martensite
MAC	Martensite, austenite or carbide
PF	Intragranular polygonal ferrite
TC	Thermocouple
UTS	Ultimate Tensile Strength
YS	Yield Strength

1 INTRODUCTION

The economic pressures of an increasingly competitive global market have made life extension of engineering structures or large industrial components a major issue for operators and contractors in the energy and transportation sectors [1]. As a result, a number of measures (preventive or otherwise) are continuously being devised, evaluated and implemented with the sole objective to maintain engineering structures in operation. Such measures should, however, be cost effective and avoid endangering operation or introducing any additional risk of failure to the structure in question [2].

As far as repair procedures are concerned standard fusion welding process have been used in the vast majority of cases [3]. However, alternative process have been long sought for in situations which either the environment or the weldabilty of the base material might play a role in the overall quality of the repair weld. This is particularly the case of underwater repair of offshore structures or pipelines [3]. In such situations the simultaneous co-existence of a welding arc and molten steel material in a high humidity (or even totally wet) environment has always been a cause of concern to certification societies and operators alike [4]. Avoidance of the inherent risks can only be achieved by substantial, in some cases even prohibitive, expenditure. A similar situation is found in the repair of structural elements in explosive, toxic or radioactive installations [5]. Solid state welding processes, such as friction welding, have always been considered as a feasible repair alternative for difficult-to-weld or non-weldable materials [6]. Typical examples are NiAl-alloys (used in ship propellers) [7], intermetallic alloys and large cast structures (in iron, aluminium or titanium alloys) [8, 9] which are sensitive to either melting or the thermal cycle imposed by fusion welding operations. The fact that bonding in friction welding takes place below the melting point limits the extent and complexity of metallurgical reactions causing embrittlement (i.e. formation of intermetallic phases), cracking and porosity. Moreover, gas absorption and atmospheric contamination are generally not an issue reducing therefore the importance of the environment in the repair quality [6, 10-12].

Up to late 80's it was almost impossible to apply friction welding "in-situ". The machines available were then – as most of the available systems today – workshop-based installations, i.e. large and heavy, delivering massive forces (up to 2000 ton) at relatively low rotational speeds (i.e. 500 rpm) [13]. The introduction of portable systems capable of high rotational speeds and low forces turned friction welding into a "field welding" process [14, 15]. Approximately ten years later an alternative friction welding repair method was patented [16], which at first glance seemed somewhat complex. However, when considering the achievements in the area of automation (control and hardware, particularly tool-changing devices) it could be considered as a real alternative repair process based on the principles of friction welding [17, 18]. This method – called Friction Hydro Pillar Processing (FHPP) – consists in drilling a hole at the defect location, filling this hole by welding a consumable stud inside it and machining off the remaining section of the stud. Long defects could be repaired by a number of studs, welded sequentially (or otherwise) along the defect, whereby a minimum in overlapping between two consecutive studs should be observed. The

combination of portable friction welding systems and FHPP brought the dream of “in-situ” solid state repair technology a step closer to industrial reality [17-20].

This new perspective has been recognised by the industry in general and by the European Commission in particular, which led to a number of research initiatives aiming at the further development of process and hardware[1] as well as to initial steps towards implementation in real repair scenarios[2, 3] [21, 22]. The latter has been also taken up by the industry itself in the form of Group Sponsored Projects and research contracts to further expand the application of the method. Nevertheless, it did not took too long for those involved in such projects to realise that the available knowledge on the process (i.e. weld formation) and the performance of FHPP repairs was limited at its best at this time. As a result for every new material investigated extensive parameter studies had to be performed leaving not much time left for any sensible characterisation [17, 18].

The idea for the present work was emerged from the scientific necessity to explain the phenomena taking place during FHPP and to provide a set of performance data on welded repairs to those intending to use the process. Starting from a number of preliminary experiments and a substantial review of the published work, an experimental strategy has been devised to establish the bonding mechanisms operating in FHPP and to characterise repair welds on an industrially relevant steel material.

At the beginning of the present work the proposed repair technology was looked upon as an exotic method for very particular repair scenarios. Presently the industrial interest is overwhelming and the possible scope of applications is continuously increasing. In the repair area a number of applications are currently being investigated such as, ship propeller, Al fan casing of jet turbines, Riser Turrets in FPSO’s[4], composite Ti-risers, etc. The increasing complexity in alloys and configurations described above is probably an indication of where the future of this technology lies.

---

1 European funded research project “Affordable underwater robotic friction welding repair system – ROBHAZ”, Brite Euram III project No. BE96-3692, 06.1997-05.2000

2 European funded research project “Friction Stitch Welding Repair of Pipelines – STITCHPIPE”, CRAFT project, 12.1998-08.2001

3 European funded research project “Remotely Operated Hot Tapping of Deepwater Subsea Pipelines – PIPETAP”, CRAFT project, 10.2001-03.2003

4 Floating Production Storage and Offloading – Floating oil production unit with storage capacities, commonly modified large crude oil tanker.

2 FRICTION WELDING – A LITERATURE REVIEW

As reported by Crossland [23], the first friction welding related patent was granted to Bevington in 1891. His idea was to friction weld and simultaneously extrude two tubes. Another patent was granted to Klopstock and Neelands 1941 [24] on friction seam welding and friction welding of tubes. However, probably the first industrial application of friction welding was during World War II for the welding of thermoplastic piping in Germany. The broad industrial use of the process was however started by a Russian machinist A.I. Chudikov, who proposed the process of general friction welding and patented it in 1956, followed by extensive fundamental research on the process in the Soviet Union.

Nowadays the main field of application for friction welding in production can be found in the automotive and aerospace industry. A total amount of 1800 machines are currently in use in Europe and the USA [13]. The bandwidth of those machines ranges from 24000 rpm with less than 1 kN axial force to 100 rpm with 2000 kN axial force representing the various applications. The automotive industry depicts the growing demands in friction-welded components in recent years for example in the amount of airbag gas generator produced per year. This number rose from 28 million in 1998 to 36 million in 1999 [25].

Friction Welding is a solid-state joining process that produces a weld by rotating or moving workpieces under compressive force relative to eachother to produce heat and plastically displace material from the faying surfaces [26]. While generally considered a solid-state welding process, some authors report, that under some circumstances a molten film may be produced at the interface [27-31]. However, even then the final weld should not exhibit evidence of a molten state because of the extensive hot working during the final stage of the process. Nevertheless, the majority of authors consider that during the entire welding process no molten material is produced [23, 32-38].

The weld produced is characterised by the absence of a fusion zone, a narrow heat-affected-zone (HAZ), and the presence of plastically deformed material around the weld (flash). Weld quality is dependent upon the proper selection of material, joint design, welding variables, and postweld treatment if necessary.

The two general requirements for producing good friction welds are, first, that the materials to be joined can be forged and, second, that friction can be generated at the weld interface. The first requirement eliminates similar welds in brittle materials such as ceramics, some cast irons and cemented carbides while the second eliminates materials that contain alloying elements that provide dry lubrication [26].

2.1 ENERGY INPUT METHODS

There are two general methods of supplying energy in friction welding [26]: Direct Drive Friction Welding, sometimes called conventional friction welding, and Inertia Friction Welding, also called Inertia Drive Welding or Flywheel Friction Welding.

2.1.1 Direct Drive Friction Welding

In this method, one of the workpieces is attached to a motor drive unit, while the other is restrained from rotation. The motor driven workpiece is rotated at a predetermined speed. The workpieces to be welded are moved together and a friction welding force is applied. Heat is generated as the faying surfaces (friction surfaces) rub together. This continues for a predetermined time, or until a pre-set amount of upset (burn-off) takes place. The rotational driving force is discontinued, and the rotating workpiece is stopped by either the application of a braking force or by its own resistance to rotation. The friction welding force is maintained or increases (forging force) for a predetermined time after rotation ceases [26]. The weld is then completed.

2.1.2 Inertia Drive Friction Welding

In Inertia Friction Welding, one of the workpieces is connected to a flywheel, and the other is restrained from rotating. The flywheel is accelerated to a predetermined rotational speed, storing the required energy. The drive motor is disengaged and the workpieces are brought together by a friction welding force. This causes the faying surfaces to rub together under pressure. The kinetic energy stored in the rotating flywheel is dissipated as heat by friction at the weld interface as the flywheel speed decreases. An increase in friction welding force may be applied (forging force) before rotation stops. The forging force is maintained for a predetermined time after rotation ceases [26]. Then the weld is completed.

Both methods (inertia- and direct drive friction welding) produce excellent solid state bonds. There are slight differences or advantages of one method over the other depending upon the application (size, material combination and geometry considerations) [32]. The majority of friction welding machines are direct driven, while many machines in the USA are inertia welding machines. Owing to the fact that all welds produced within this work were made with a direct driven system, particular aspects of inertia welding will not be further discussed in this review.

2.2 Process Variations – Conventional and Additional Methods

Although there are various types of relative motion, the simple rotation of one of the workpieces while holding the other stationary remains the most widely used method of friction welding.

The friction welding methods can be divided in conventional and additional methods according to the American Welding Society (AWS) [26] and the German Welding Association (DVS) [39]. The conventional methods are: Basic, Counter Rotation, Centre Drive, Centre Drive (dual production) and Twin Welds. The additional methods are Radial Welding, Orbital Welding, Angular and Linear Friction Welding, Friction Surfacing, Friction Stir Welding and Friction Hydro Pillar Processing. The common processes will be presented and described briefly below. For further information on the additional processes refer to:

- Radial Welding [26, 40-44]
- Angular and Linear Friction Welding [26, 45-49]
- Friction Surfacing [24, 26, 46, 47, 50-70]
- Friction Stir Welding [26, 71-76]

2.2.1 Basic Rotational Friction Welding

This is the conventional and most commonly used process. Here, one of the workpieces rotates while the other is held stationary. The process has many applications in the automotive industry, including the joining of exhaust valve stems to valve heads and securing turbocharger rotor blade assemblies to shafts, involving both similar and dissimilar metals. Figure 2-1 shows the basic welding configuration. For further details see [26, 32, 39, 77-80].

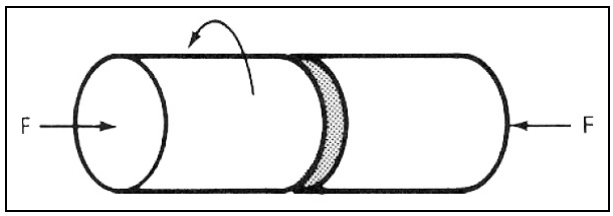

Figure 2-1: Basic Rotational Friction Welding [26].

2.2.2 Counter Rotation

With this method both workpieces are rotated but in opposite directions. This process is suitable when high speeds of rotation are required. Figure 2-2 depicts the basic arrangements.

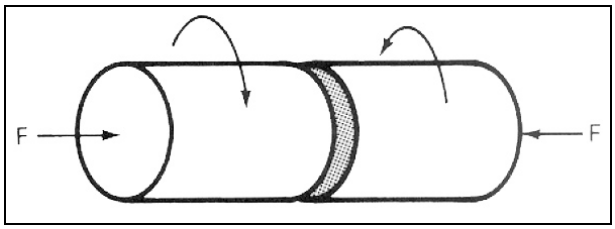

Figure 2-2: Counter rotation [26].

2.2.3 Centre Drive (Splicing)

Figure 2-3 shows the third common type of friction welding. Two stationary workpieces are pushed against a third rotating piece positioned between them. This set-up might be desirable if the two pieces are long or if they have an inappropriate shape so that rotation would be difficult or impossible by the other methods.

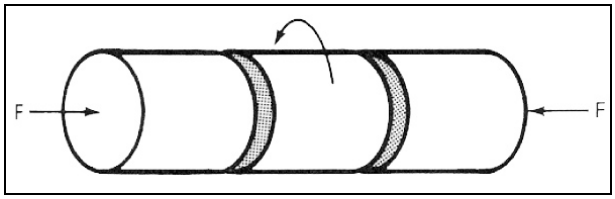

Figure 2-3: Centre drive [26].

2.2.4 CENTRE DRIVE (DUAL PRODUCTION)

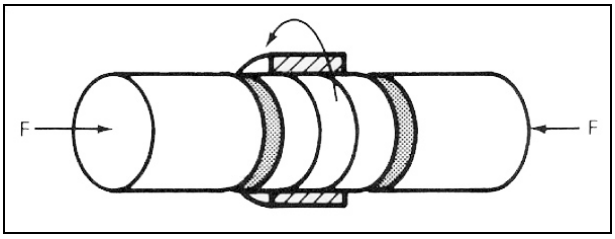

Figure 2-4: Centre drive - Dual production [26].

A similar situation, shown in Figure 2-4, involves the rotation of two workpieces against a third one positioned between them. The main difference with the centre drive method is that it is possible to make two welds at the same time for the purpose of improving productivity.

2.2.5 TWIN WELDS

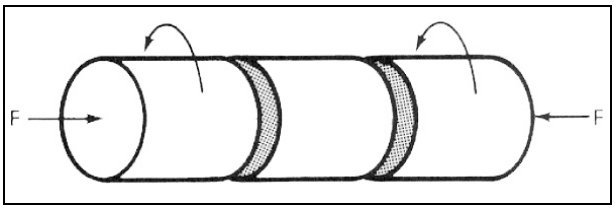

Figure 2-5: Twin welds [26].

Twin welds involves two rotating workpieces pushing against a third one stationary piece at the middle. Figure 2-5 shows the basic configuration of this type of welding.

2.3 PROCESS CHARACTERISATION - PHASES OF THE PROCESS

The division of the process in different phases is a common way when describing the weld cycle and the mechanisms related to it. Different authors divide the cycle in different numbers of phases. The AWS [26] and the American Society of Metals (ASM) [80] use two different phases while Vill [79] and Crossland [23] use three phases. A more detailed subdivision has been proposed by Neumann and Schober [81], Pauly [82] Böhme and Hermann [83] and Nentwig [84] with four phases and by Ellis [85] with five phases. The division in four phases is the most common one and will be presented in the following as illustrated in Figure 2-6.

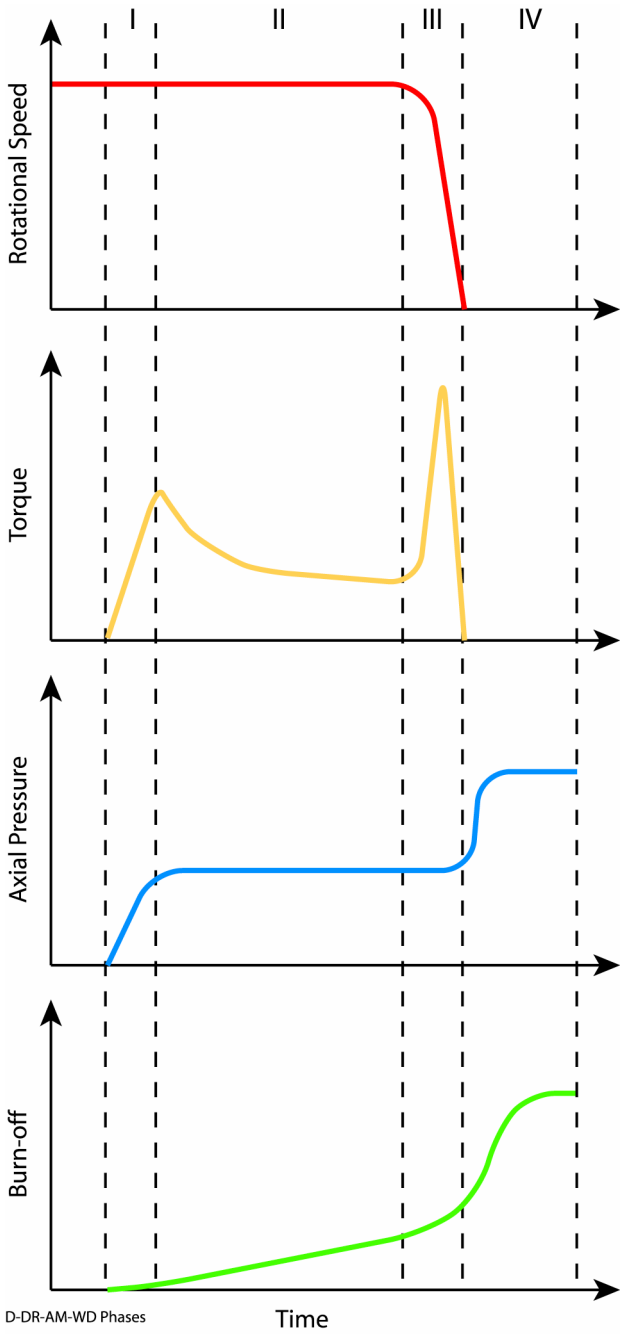

Figure 2-6: Schematic illustration of the process parameters during direct drive friction welding (I: Rubbing Phase, II: Heating Phase, III: Breaking Phase, IV: Bonding Phase), according to [81-84].

2.3.1 Phase 1 – Rubbing Phase

During the first part of phase 1 the initial contact of the faying surfaces will mainly result in a smoothening effect of these surfaces. The remaining part of phase 1 is briefly characterised by seizing and microbonding processes [23, 28, 79].

At the beginning of phase 1 only a limited amount of the nominal welding surface actually makes contact. Therefore, the surface pressure reaches locally extremely high values promoting plastic deformation and hence, flattening of the faying surfaces. In addition to these relatively high stresses, the outer regions of the joint are subjected to the highest relative rotational speed between the faying surfaces [84]. By rubbing, the surface roughness

is partly smoothened by elastic and plastic deformation and local melting, starting in the outer regions of the weld zone [37, 79]. Bethlehem [86] showed that the region between 0.3 and 0.7 of the radius is subjected to severe deformation and heating in this first stage, whereas the rest of the surfaces stays almost unaffected. This phenomenon is shown in Figure 2-7 on two stainless steel studs, which were separated after short rubbing durations. Dark rings of plasticised material can be seen at approximately 0.7 radius. The outer part depicts oxidation due to heating, while the inner region still shows unaffected surface with the machining marks.

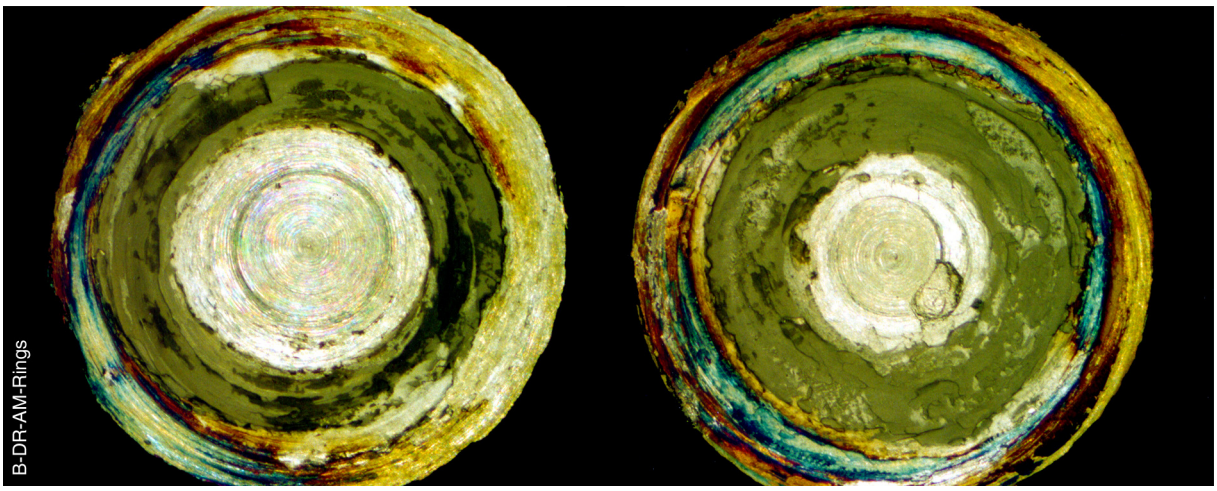

Figure 2-7: Plastification rings on stainless steel studs after different rubbing durations.

Eichhorn [87] observed that heating and plastification at the beginning of the process is preferable in the rotating partner, which leads to an uneven HAZ and degree of deformation. Isolated local bonding (microbonding) eventually taking place simultaneously across the contact surface is almost immediately sheared off. The shearing of those microbonds induces additional heating in the surrounding material [88]. If the temperature has quickly, but only locally, reached the melting point or even higher values, the heat generation decreases substantially. The heat dissipation increases and melting cannot be maintained [81]. If the material is plastified, the recrystallisation rate is lower than the deformation rate, which results in shearing of the local microbonding. The mechanism of the energy input and transformation is presented in more detail by Bethlehem [86].

Crossland [23] reported that owing to the processes described above oxides and adsorption layers are broken up and surface contaminations are removed. Due to the very high local temperatures occurring repeatedly for a short period of time and the friction induced chemical reactions, new oxides are produced. Especially in the outer regions isolated particles are transported out of the rubbing zone due to high radial forces (hydro-extraction effect).

One of the main effects of phase 1 is the smoothening of the outer regions of the rubbing surfaces, which takes place during the first revolutions of the workpiece within phase 1.

When the smoothening in the outer regions is almost completed, it starts to develop towards the rotational centre of the joint. In the outer regions almost no heat is produced during this

intermediate phase, because of the reduced friction contact (the faying surfaces are now widely smoothened) and the presence of oxide layers generated in the first part of phase 1.

Lower radial forces and restricted material flow conditions closer to the rotational centre obstruct the hydro-extraction effect of surface contamination particles. Therefore, a material concentration on a circular ring area can be observed, its distance from the workpiece rotation centre is 1/2 to 2/3 of the friction surface radius (Figure 2-8). This concentration causes local heating forming a thin plasticised film of sheared-off material. This ring area increases in size, an increased amount of the nominal welding area makes contact, and more isolated microbonding is produced [83, 89].

Owing to heat conduction the temperature also rises in the axial adjacent material. In plasticised zones a decrease of the deformation rate caused by torsion can be observed owing to the increased temperature [80, 87, 89].

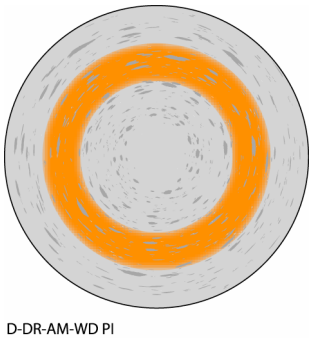

Figure 2-8: Schematic illustration of the faying surface during phase I: Plasticised material concentrates on a ring between 1/2 to 2/3 of the radius.

As a result of the above described processes the friction moment rises to its first maximum (Figure 2-6). The generated heat per time and the temperature itself increases significantly [90].

Phase 1 is completed as soon as the friction moment reaches its maximum. This peak is caused by the removal of the contaminant film on the one hand and the additional friction caused by rough surfaces produced by seizure on the other. The extraction of the contaminant film allows contact of fresh metal surfaces with a considerable increase in the coefficient of friction [79].

2.3.2 Phase 2 – Heating Phase

The increasing temperature in the ring of plasticised material (Figure 2-8) reached in the course of phase 1 causes the squeezing of highly plasticised material to cooler zones of the friction area. Owing to the immediate cooling of the plasticised material intense friction is produced again in these particular zones and the ring area is extended towards the rotational centre. The temperature in this area is comparatively low, because the radial deformation is quite small due to the low relative speed [79].

Particles encapsulated in the ring and not re-dissolved in the plasticised material are transported to the rotational centre of the weld zone (Figure 2-9).

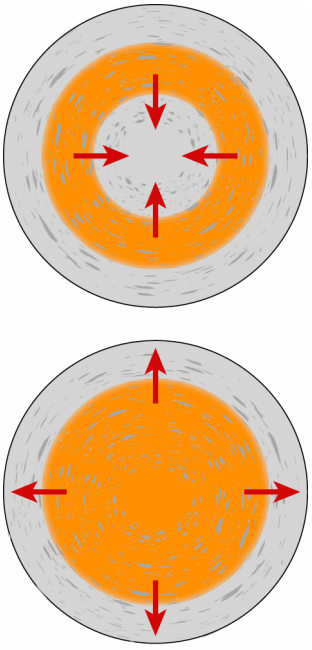

Figure 2-9: Schematic illustration of the faying surface during phase II: Plasticised area extends first to the centre of the diameter and finally to the circumference as well.

Figure 2-9 illustrates the widening of the ring area until it reaches the rotational centre, forming a circular area extending its diameter slowly towards the outer regions of the weld zone. Temperature equilibrium is achieved, which is supported by a self-balancing effect. This effect was described by Crossland [23] as follows: As the temperature rises, the metal becomes more plastic and the torque is reduced giving a lower heat generation with a resultant lower temperature. This in turn softens the material, resulting in less deformation work and a decrease of the temperature.

In the outer regions of the weld zone the material is easily pressed out of the friction surfaces, due to the high plastification and to low deformation constrain. As the temperature of the material and the height of the plasticised zone increases, the resistance to the axial force reduces and the material is pressed out of the friction area forming the flash [23].

The height of the plasticised zone decreases and cooler areas now make friction contact, heat up and become highly plasticised [79]. This process is maintained as long as the temperature and the height of the plasticised zone can be kept in equilibrium. As a result more material is pressed into the flash.

These balanced actions result in heat saturation of the friction area and the corresponding zones. A stationary temperature field is achieved at the faying surfaces and the friction moment decreases [79, 89] (Figure 2-6). From this point on an almost constant burn-off rate (i.e. shortening of the workpieces) is established. With increasing thermal saturation of the workpieces the energy required for plastification reduces leading to a lower friction moment [91]. However, the growing flash increases the friction surface and hence the friction moment. The common opinion is that these phenomena balance each other resulting in an almost constant friction moment [38]. Only Eichhorn [87] showed that the friction moment is decreasing constantly without staying on a certain level.

Phase 2 is concluded as soon as the process reaches the limiting control parameter, which means a predetermined temperature point, a certain amount of burn-off or a pre-set time.

2.3.3 Phase 3 – Breaking Phase

If the direct drive method is used, the breaking phase begins with a controlled decrease of rotational speed (Phase 3, Figure 2-6). Owing to the self-balancing effect described above the temperature drops. Additionally, the shear resistance increases owing to the lower deformation rate and hence the friction moment reaches its second peak [23].

This increase of the friction moment causes additional deformation in the adjacent material, which has so far not been subjected to any deformation. It should be noted that the

deformation resistance of these areas is comparatively low, since they have almost reached the friction surface temperature (due to thermal saturation in axial direction) before they are actually subjected to deformation [92].
The lower rotational speed also results in a higher burn-off rate. Neumann and Schober [81] reported an increasing flash temperature caused by material pressed from the inner regions of the weld zone into the flash.
At a critical point the rotation is reduced to such a low level that the temperature at the faying surfaces can no longer be maintained. Therefore the shear resistance of the material increases and torsional deformation takes place in a larger region along the workpieces. The friction moment increases substantially and has been observed to be constant for some milliseconds [91], Figure 2-6.

2.3.4 PHASE 4 – BONDING PHASE

The mechanism of bonding already begins in the heating phase, although bonding is not homogeneous across the contact surface [92]. The forging force achieves a homogeneous bonding across the whole section during the bonding phase.
Although the accepted opinion is that the use of a forging force significantly improves the mechanical properties of the weld [93], some experiments show that good welds can be obtained without an increase of the force after rotation stops which means without any forging force [85].
The change from the friction to the forging force (Figure 2-6) should take place at the end of the braking phase. The increased bonding force results in an abrupt increase of the burn-off rate and the friction moment [87]. Oxide layers in the outer regions of the weld zone produced by insufficient friction contact are now expelled. The welding surfaces make closer contact and particularly the materials in the outer regions are brought together within atomic distances to produce metallic bonding [92, 94].
After the rotation has stopped, the dynamic softening process, i.e. the deformation, is completed, but the diffusion processes still remain. As the material begins to cool down, static recrystallisation, crystal regeneration and creeping processes occur. Internal stresses are widely eliminated - a determinant factor for the mechanical properties of a friction weld [83].

2.4 RELEVANT PROCESS PARAMETERS

According to the literature [26, 32, 95, 96], there are a number of important process parameters and variables in friction welding.

Process parameters:

1) Relative speed of the faying surfaces
2) Normal force on the contact area
3) Heating time
4) Burn-off and burn-off rate
5) Time required to stop the spindle
6) Forging force rate and duration.

Process Variables:

1) Temperature of the friction surfaces
2) Nature of the material
3) Presence of surface films
4) Rigidity and elasticity of the friction surfaces;

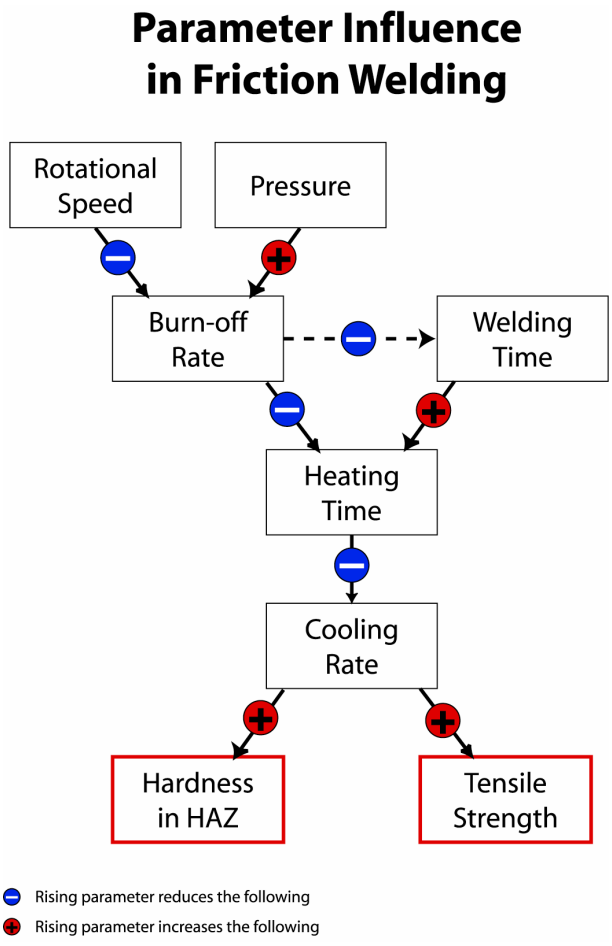

Figure 2-10: Parameter Influence in Friction Welding.

Although all the parameters are relevant, the first four are the most important ones and will be considered in more detail in this work. Also the influence on the weldment quality and process performance will be discussed.

Usually welding parameters are developed and optimised through a series of trials for a given application. 1979 Dennin [97] presented the first attempt to establish welding parameters for new applications by numerical calculations without performing welding trials, but reducing the amount of welding experiments prior to production is still a matter of research today [98].

A summary of the influence and interaction of the basic welding parameters is given in Figure 2-10.

2.4.1 The Relative Speed of the Faying Surfaces

The relative rotational speed is the least sensitive process parameter [26]. Nevertheless, the tendency to increase the rotational speed during friction welding to intensify the process is erroneous and there are certain optimum speeds for each individual material combination and application [79].

From the standpoint of an intensification of the process and improvement of the quality of the welded connection it is desirable to use relatively low rotational speeds. The process efficiency is improved as a result of reduced heat losses, which reduce the amount of energy used for welding. This leads to a necessary increase in the power of the installation and, what is more important, to a much longer rubbing phase. The duration of this phase (and for low rotation speeds throughout the entire welding process) depends to a large degree on the initial condition of the friction surfaces [79].

At high rotational speeds deep tearing at the friction surfaces is replaced by a polishing action [79, 99]. In order to achieve the conditions for plastification at the faying surfaces, longer heating times are required. Longer heating times allow the propagation of thermal energy along the axial direction of the workpieces and as consequence a greater volume of material is heated [100]. Therefore, high rotational speeds lead to lower cooling rates, wider HAZ and hence lower hardness at the vicinity of the bonding line [85, 87].

On the other hand, lower speed of rotation produces a thinner HAZ with a profile that is noticeably much more severely pinched in comparison with similar welds produced at a higher speed of rotation. Conversely, for certain dissimilar metal combinations, low velocities (and their shorter heating times) can minimise the formation of brittle intermetallic compounds. In practice, heating time (for a given amount of upset) is usually controlled by varying the friction welding pressure [26, 97].

Microstructural analysis of welded steel joints show that, for a given welding pressure, the increase in speed produces an increase in grain size. On the other hand higher speeds lead to the formation of a much coarser Widmanstätten structure both, at the interface and adjacent HAZ. Finally, it can be seen that higher rotational speed resulted in a significantly lower tensile strength, particularly at lower pressures [85, 87, 100].

2.4.2 The Normal Force

Although this variable may vary in broad ranges in the heating and forging stage it controls the temperature gradient in the weld zone, the required drive power, and the axial shortening.

The axial force must be high enough to hold the faying surfaces in intimate contact to keep detrimental substances out of the welding zone and to avoid oxidation [26]. However, it should be noted that high forces cause local heating to high temperatures and rapid axial shortening (high burn-off rate), which might be uncontrollable [85].

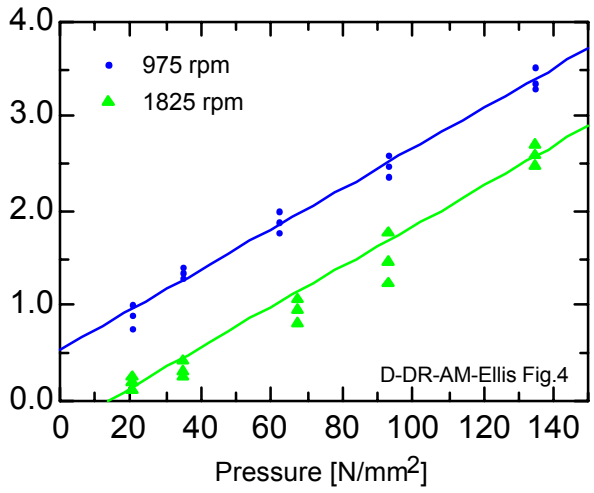

Figure 2-11: Relationship between steady burn-off rate and pressure [85] (19mm mild steel bar-to-bar weld).

Eichhorn [87] showed that for a given burn off, the time from the initial contact of the surfaces to the end of the welding procedure decreases as the normal force increases. The higher the pressure, the faster the material is consumed and the shorter the welding time will be. Ellis [85] presented a relation between the axial pressure and the burn-off rate for mild steel bar-to-bar welds (Figure 2-11).

After the breaking phase two different methods of varying the axial force are commonly used: maintaining the force or increasing it (forging). For the latter, a forging force is applied, which can improve the joint quality by ejecting overheated grains into the flash [26, 100].

Ellis [85] demonstrated that the axial force also influences the width and character of the HAZ. The overall shape ranges from an almost parallel sided boundary at low forces to a more ‘’pinched’’ or double cone profile in the centre of the interface at higher forces. In the second case, the heat liberated is totally used to plasticise the material and does not propagate in the axial direction. According to Ellis [85], welds made at the higher forces show a narrower region where the hardness values are lower than in the parent material. It means that, the higher the force is, the more pinched the hardness profile will be in the interface region.

To compensate for a large mass of material the AWS [26] suggests to increase the axial force to produce adequate heating. This intensification also has a benefit on the weldment properties, as it changes the nature of the microstructure at the interface from a near Widmanstätten structure at low forces to a more equiaxed and progressively finer grain sized ferrite [100]. The finer grain size suggests that the interface temperature is reduced, since extrusion of heated metal begins at a lower temperature. The high axial force changes the heating conditions, as the plasticised material that “carries” the heat, is immediately pressed into the flash. Additionally Ellis [85] reported that the ultimate tensile strength progressively increases with axial force.

2.4.3 HEATING TIME

Vill [79] suggested that it would be better to select the duration of the heating period rather than the upset as the third basic parameter of the friction welding process. This suggestion is based on the fact that for a given power of the process (the speed and pressure are given) the duration fully determines the energy to be utilised for welding. Consequently the heating time determines the temperature conditions of the process, keeping in mind that the plastic deformation of the specimen is derived from the temperature conditions. Therefore some authors [31, 34, 101] suggested the use of temperature itself as the third welding parameter next to the relative speed and the axial force.

The heating time is defined as the period from initial contact of the faying surfaces to the end of the braking phase. The heating time is significantly influenced by the axial force and by the rotational speed. It is reduced as force is increased and decreases with rotational speed [79, 85].

The heating time can be controlled in two ways: the first is with a suitable timing device that stops rotation at the end of a pre-set time, the second is stopping rotation after a predetermined axial shortening (burn-off) [26].

Heating time is important especially for a low burn-off rate because it not only defines the microstructure of the interface but also controls the depth of heating in the workpiece by conduction and therefore the width of the HAZ [85].

At the end of the forging stage, depending on the cooling rate the austenite transforms into different products (i.e. ferrite, pearlite, bainite, or martensite). The type and the volume fraction of the final microstructure are a function of the peak temperature reached during the welding cycle and the subsequent cooling rate. The microstructure will determine the final strength and susceptibility of the weld to brittle fracture and other properties of the joint. The peak temperature and the cooling rate are difficult to measure experimentally due to severe plastic deformation that takes place at the weld interface [27].

The cooling rate is affected by the surrounding media and the welding time combined with the total amount of flash formed around the weld interface. If the flash has a large mass, then the heat stored within the flash will be conducted back into the weld thereby reducing the cooling rate of the metal within the HAZ. Short heating times naturally result in a high heat generation rate. This also involves a relatively high burn-off rate forming a big flash where most of the heat is stored as sensible energy. In comparison, when using longer heating times, not all of the heat generated at the weld interface is stored in the flash, but much of it has time to conduct into the welded parts.

From the standpoint of an intensification of the process and improvement of the quality of the weld, it is desirable to have short heating times without flash formed. Thus, the cooling rate will be higher and the mechanical properties will be better. On the other hand, if it is desirable to preserve the toughness it is better to have longer heating time and consequently lower cooling rate [87, 100].

2.4.4 Burn-off / Burn-off Rate

Burn-off describes the amount of plasticised material and is usually measured as the axial displacement or shortening of the rotating workpiece. The burn-off rate is the amount of burn-off per second and can therefore be considered as a representation of the welding speed.

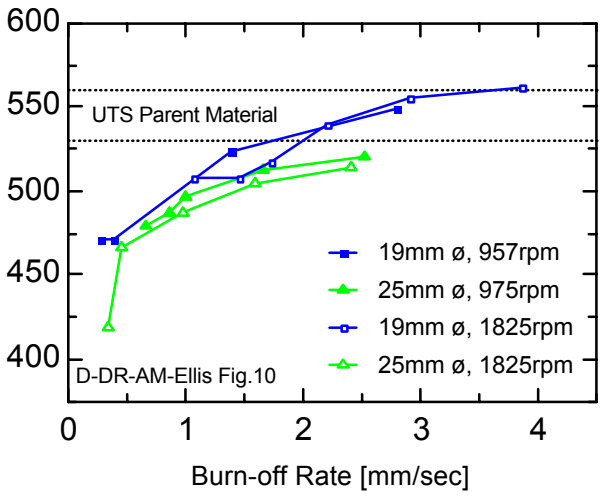

Figure 2-12: Effect of burn-off rate on tensile strength [85] (mild steel bar-to-bar welds).

The burn-off not only controls the welding cycle, but also has a significant influence on the weldment properties. The applied force and speed of rotation will influence the time needed to reach the pre-set amount of burn-off. The time from initial contact of the surfaces to the end of burn-off becomes shorter as force increases and a lower speed results in a higher burn-off rate for the same nominal pressure. Since the burn-off rate is increased, the total welding time is reduced and hence there is less time available for grain growth and homogenisation to take place [85].

Figure 2-12 illustrates the effect of burn-off rate on tensile strength according as presented by Ellis [85].

On the other hand, controlling the process by burn-off has its disadvantages too. Vill reported that large burrs, central projections remaining on the surface of the specimen, misalignment of the end cross sections and similar surface defects have a negative influence on the quality of the weld if the process is controlled by the burn-off [79]. The wear of these irregularities is usually detected as the beginning of the upset before the surfaces make full contact. Hence the control system will stop the weld before the necessary burn-off was achieved.

2.4.5 Welding Parameter Windows for Carbon Steels

Table 2-1 gives a summary of optimised welding parameter windows for direct drive friction welding of carbon steels.

Table 2-1: Welding parameter windows for direct drive friction welding of carbon steels.

Author	Year	Ref.	Alloy	Diameter [mm]	Max. Relative velocity* [m/s]	Friction Pressure* [MPa]	Forging Pressure* [MPa]
V.K. Lebedev I.A. Chernenko	1992	[102]	Normal Quality carbon steels	16-40	1.20-2.00	50-100	50-100
V.K. Lebedev I.A. Chernenko	1992	[102]	Low-alloy structural steels	14-22	0.70-1.70	45-90	45-180
A. Neumann D. Schober	1991	[81]	Low-alloy structural steels	15-40	0.80-2.00	30-50	60-100
A. Neumann D. Schober	1991	[81]	Low-alloy structural steels	40-100	0.80-2.00	50	100
DVS	1993	[77]	Low-alloy structural steels	20	1.57-3.14	50-80	150-250
F. Eichhorn R. Schaefer	1968	[87]	Mild steel (DIN S235)	20	1.00-2.00	30-50	30-80
AWS Welding Handbook	1991	[26]	Mild steel	Not restricted	1.30	31-60	76-152
G. Dennin	1979	[97]	Mild steels	20	1.57	40-60	50-180
C.R.G. Ellis	1972	[85]	BS970 EN3B mild steel	18-25.4	0.92-2.33	30-105	30-105
W. Lucas	1973	[100]	BS970 EN3B mild steel	18	1.72	30-90	30-150
B.J. Eberhard B.W. Schaaf A.D. Wilson	1983	[103]	ASTM A516 Grade 70 carbon steel	127x12.7 pipe	2.20	55	110
S. Manteghi	1994	[104]	BS 970 Grade 080 M40 (AISI 1039 and 1040)	25	1.86	60	160
V.K. Lebedev I.A. Chernenko	1992	[102]	High Quality carbon steels	10-70	1.00-2.00	35-50	40-100
ASM Handbook	1993	[80]	Carbon steels	Not restricted	1.20-3.00	83-166	166-332
ANSI/AWS C6.1-89	1989	[33]	Mild Steels	Not restricted	1.27-4.06	41.4-83	83-166

* All welding parameters from optimised conditions as stated in the respective references.

2.5 Mechanical Properties – Influence of the Basic Welding Parameters

In spite of being an old technology, there are many studies addressing the optimisation of the weldability of special materials by friction welding. A large amount of materials have been considered to be not-weldable initially, but nowadays are considered to be fully weldable by friction welding.

In principle, almost all metals that can be hot forged and are unsuitable for dry bearing applications can be friction welded. Some metals may require postweld heat treatment to remove the effect of the severe deformation or quench hardening at the weld interface [26, 33, 39, 77, 78]. Additionally, there is a great number of dissimilar metal combinations that can be welded, even if this involves combinations that have high and low thermal conductivity, a large difference in forging temperatures, or the tendency to form intermetallic compounds.

Figure 2-10 shows possible material combinations weldable by friction welding as presented in the literature and reported by equipment manufacturers [26, 39, 77, 78]. Nevertheless, this table is not a strict rule but is still a matter of research.

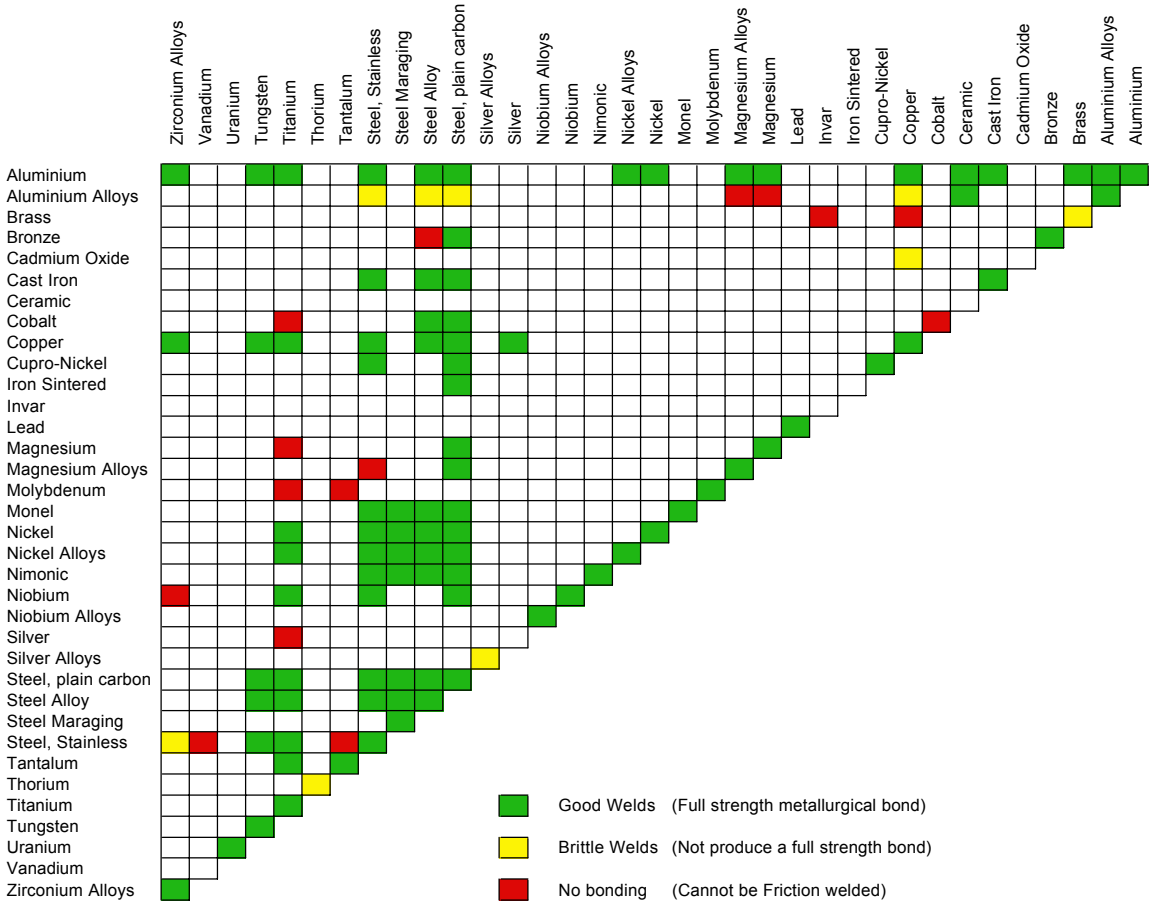

Figure 2-13: Weldability according to AWS [26] and DIN [105].

Many authors have reported the influence of the basic welding parameters on the mechanical properties of friction welded joints. Table 2-2 gives a summary of the influences of the basic welding parameters for conventional friction welding based on the following references: [26, 55, 57, 79, 85, 93, 100, 106-108]

Table 2-2: Influence of the basic welding parameters on the joint properties.

	Mechanical Properties	
Welding Parameter	Tensile Strength	Hardness
Rotational Speed	Higher rotational speeds result in a significantly lower tensile strength. Higher speeds give higher heating time and respectively a lower cooling rate.	Higher rotational speeds result in a progressively lower hardness. Lower speeds reduce the heating time and increase the cooling rate, resulting in higher hardness.
Axial Force	The ultimate tensile strength progressively increases with the axial pressure. The higher the pressure is, the higher the burn-off rate will be and, consequently the amount of heat generation is low. As a result the process will present higher cooling rate.	The hardness increases with the axial pressure. The higher the pressure is, the higher the burn-off rate will be and, consequently the amount of heat generation is low. As result the process will present higher cooling rate.
Welding Time	Short welding time increases the ultimate tensile strength. The HAZ in welds produced with short welding time is narrower and, consequently, the heat dissipation (cooling rate) will be higher.	The welding time is the most important parameter to control the hardness. The higher the welding time, the smaller the cooling rate and, consequently the smaller the hardness.
Forging Force	The forging force has two beneficial effects on the strength of the weld. Adequate forging is essential to break up the coarse inclusions, which are adversely reoriented during frictional heating and to refine the coarse austenite grains by hot-working. When the metal cools down the tendency to form Widmanstätten structure will be lower. The forging force should always be applied correctly in order to improve the ductility and to increase the ultimate tensile strength and the hardness.	

A summary of the achievable mechanical properties of direct drive friction welds in carbon steels is presented in Table 2-3. Generally it could be said that, if optimised welding parameters are used to produce similar welds in steel materials by friction welding, the tensile properties of the joint are above base material properties (overmatch condition). Fatigue properties are also likely to be superior than those of the base material. Neumann and Schober [81] reported that Charpy impact tests of standard friction welds usually give

sufficient values, but should be judged very carefully. Minor deviation of the notch besides the bonding line might already result in significantly different results as different microstructures are tested. In addition to this, the standard deviation is generally very high.

Table 2-3: Summary of mechanical properties of direct drive friction welds in carbon steels.

Author	Year	Ref.	Alloy	YS* [MPa]	UTS* [MPa]	Elon-gation * [%]	Max. Hardness HAZ*	Charpy Impact* (Temp.) [J]	Fatigue* (Tension)
A. Neumann D. Schober	1991	[81]	Mild steels	Above base material					105-110% of base material
F. Eichhorn R. Schaefer	1968	[87]	Mild steel (DIN S235)	Above base material			220 $HV_{0.2}$		
ANSI/AWS C6.1-89	1989	[33]	Mild Steels	Above base material					
S. Manteghi	1994	[104]	Mild steel (BS 970 Grade 080 M40)	Above base material			246 HV_5		Superior arc welding
C.R.G. Ellis	1972	[85]	Mild steel (BS970 EN3B)	Above base material					
B. Eberhard B.W. Schaaf A.D. Wilson	1983	[103]	Carbon steel (ASTM A516 Grade 70)	406	550	20		20 J (-20 °C)	
S.D. Bhole	1991	[106]	HSLA steel to mild steel				550 HV_5 in the HSLA		

* All values from optimised welding conditions as stated in the respective references.

2.6 General Advantages and Limitations of Friction Welding

The advantages and disadvantages of conventional friction welding are presented below. Further details on non-conventional friction welding processes can be found elsewhere [10, 11, 17, 18, 20, 26, 46, 65, 71-76, 80, 82, 94, 100, 109-118].

2.6.1 Advantages

- Special attention to surface cleanliness is not necessary for most of the applications, because friction welding tends to disrupt, displace, and finally remove surface films into the weld flash ("collar").
- Filler metal, flux, and shielding gas are not required. Unlike fusion welding, friction welding is not hazardous to operator health and is safer, because there is no metal spatter, radiation, fume, or electric hazard involving high voltage, arcs and sparks.

- Defects associated with melting-solidification phenomena, like porosity and segregation, are not present in friction welding, because it is a solid-state process.
- It is possible to make transition joints of dissimilar metals that are difficult or even impossible to weld by other processes (for example, refractory and exotic metals).
- Lower labour costs, simple part design, lower energy requirements and a short weld cycle make the process cost effective for producing components normally made by other processes.
- The process is easily automated to reproduce repeatable high quality welds. Current equipment can be operated from up to 4 kilometres from the weld site making it particularly suitable for remote applications in hazardous environment.
- The low heat input and fast cycle times allow welding to be carried out on live pipelines, gas lines and methanol lines [110, 119]
- Narrow HAZ are associated with the process.
- Friction stud welding has also been certified for use within explosive atmosphere without risk of ignition. This allows welding to be carried out safely in zoned areas of offshore and petrochemical installations without recourse to shutdown of plant and equipment.
- Operators are not required to have manual welding skills.
- In most cases, the weld strength is as strong or stronger than the weaker of the two materials being joined.

2.6.2 LIMITATIONS

- The welding area of at least one part must be rotationally symmetrical, so that the part can rotate about the axis of the welding plane. Typical part geometries that can be friction welded are: bar to bar, bar to tube, bar to plate, tube to tube and tube to plate.
- This process is normally limited to making flat and angular (or conical) butt joints.
- The material of at least one component must be plastically deformable under the given welding conditions.
- Preparation and alignment of the workpieces may be critical for developing uniform rubbing and heating.
- Capital equipment and tooling costs are high.

2.7 TEMPERATURE CYCLE

Although friction welding is a well-known process it is still difficult to make accurate temperature prediction for the faying surfaces as well as for the HAZ. The main reasons for this are considered to be the gradual increase of temperature during the friction process and the non-uniform heating of the faying surfaces [23, 31, 34, 79].
Smarzynski [35] concluded from a literature review, “that the question of temperature in the zone of friction is the object of investigations carried out by many scientists.” Additionally the

different opinions of these scientists are very conflicting [35]: “The temperature cannot reach the melting point of the elements being joined, its magnitude may be near this temperature, and it can reach it easily, but only in a small volume of the metal.”

The gradual increase of temperature during the welding process leads to a significant change of the thermal and physical properties and, consequently, there is an alteration in the initial material parameters (i.e. specific heat, heat conductivity and friction coefficient). On the other hand, during the friction welding process, the relative speed of friction at the centre of the material is zero, but increasing towards the peripheral surface. In others words, in the initial stage of the friction welding process, the temperature at the interface rises faster in the area towards the peripheral surface. The peripheral area where the temperature has risen rapidly is softened more quickly, presumably inducing the apparent friction coefficient to drop more than in the central area [31, 88].

There are various methods recommended to measure the temperature during the welding process. Usually the temperature cycle is measured in an experimental set up to establish suitable welding parameters for production welds. Wichelhaus [27] proposed an easy way to calculate the temperature cycle with very good correlation of calculated and measured temperatures based on the assumption of a homogeneous temperature across the faying surfaces. The proposed concept [27] calculates the temperature field based on measured temperatures on one spot. Shinoda [120] has proposed a different method to calculate the heat generation and consequently to obtain the correlation of heat generation and mechanical characteristics during the friction welding process of similar or dissimilar materials. On the other hand, Suga et al. proposed FEM (Finite Element Method) to calculate the temperature distribution [31]. In his experiments the temperature was calculated by combining the data on friction torque during the weld and the non-stationary heat conduction finite element analytical method.

By varying the friction welding parameters such as friction pressure, friction time and burn-off rate, the temperature distribution along the weld interface, can be changed drastically. Suga et al. [31] presented the effects of the welding conditions (i.e. friction time, axial pressure) on the temperature distribution and the hardness profiles in more detail.

3 Friction Hydro Pillar Processing – A Literature Review

In consequence of the fact that Friction Hydro Pillar Processing (FHPP) is a very young welding process the number of publications is very limited. Up to 1999 only 7 references [16, 82, 112, 114, 115, 121, 122] were published including non-reviewed sources, information flyer and graduation thesis. This demonstrates the fact that FHPP is still in a very embryonic stage of development and not widely known. In addition to this the industrial implementation suffers from the problematic licence politics by the inventor TWI, which makes it almost impossible to develop new fields of applications and to perform further optimisation of the process itself.

3.1 Description and Process Characteristics

The most comprehensive description of the process was given by Thomas and Nicholas 1997 [115], while an illustration can be found in Figure 3-1:

> *"The FHPP technique involves rotating a consumable rod co-axially in an essentially circular hole whilst under an applied load, to generate continuously a localised plasticised layer. The plasticised layer coalesces and comprises a very fine series of adiabatic, helical rotational shear interfaces, part spherical in shape. During FHPP the consumable member is fully plasticised across the bore of the hole and through the thickness of the workpiece. The plasticised material develops at a rate faster than the axial feed rate of the consumable rod, which means that the frictional rubbing surface rises along the consumable to form the dynamically recrystalised deposit material. The plasticised material at the rotational interface is maintained in a sufficiently viscous condition for hydrostatic forces to be transmitted. Both axially and radially, to the inside of the hole enabling a metallurgical bond to be achieved."*

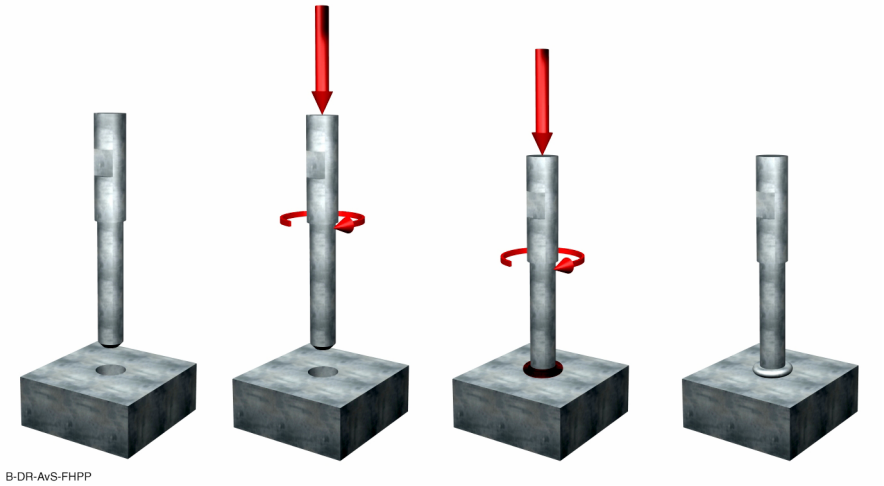

Figure 3-1: Schematic illustration of FHPP.

The main areas of application were indicated in the repair of steel structures in the construction as well as in the offshore industry. The possibility to repair cracks under water with a number of overlapping FHPP welds (Stitch Welding) has also been shown [121], while the most comprehensive list of potential advantages of FHPP (when fully developed and understood) was given by Nicholas 1995 [112] as follows:

- Solid phase joining, re-processing and new materials manufacture.
- Deep penetration narrow gap for repair and joining, (ferrous and non-ferrous metals).
- Well suited for automation and remote control.
- Can be operated for repair in hazardous environments such as underwater, explosive gases, highly magnetic and radiation.
- Large section, dissimilar materials joining capability.
- Requires less weld metal – the thicker the plate the more cost effective.
- Environmentally friendly.
- Comparatively low equipment costs.
- Low cost (bar stock) consumables.
- Rapid – 50 mm deep holes filled in less than 10 seconds.

The developments which lead to the invention of FHPP have been described by Andrews and Mitchell 1990 [113]. This report covers the development of the friction plug welding process for repair of offshore structures. Plug welding differs from FHPP first of all by the fact that the weld is performed in a tapered through-thickness hole. Consequently the diameter of the welding consumable is dependent on the thickness of the base material to be repaired. Nicholas [112] reported that, the need to keep the equipment size down but retain the possibility to repair thick sections lead later on to the invention of FHPP. Cross sections of Taper Plug welds showed that the consumable only plasticised in the contact area near to the surface [113], while with FHPP the consumable plasticises across the whole diameter of the bar [121].
The patent on the process was granted to TWI in 1993 [16]. Thomas and Nicholas [122] presented further advantages of the process in the same year focusing on the application in the heavy industry joining or repairing thick steel structures. Thomas and Nicholas [122] state special advantages for FHPP with thick-walled structures due to the fact that the amount of weld material needed is comparably low and, as in all friction welding processes, FHPP is readily mechanised and easy to automate.
The first comprehensive report on FHPP including microstructure and mechanical properties was compiled by Nicholas 1995 [112]. The first part of this report covers the process itself, where the parallel hole configuration is presented as well as a taper hole arrangement. Nicholas [112] found that those “materials which do not exhibit adequate plastic flow characteristics often respond much better to a tapered joint design”. The bonding mechanism is described by metallurgical bonding owing to a normal force on the interface between the plasticised material of the stud and the base material. The formation of a normal force to the sidewalls, although only an axial force is applied, is explained by hydrostatic behaviour of the

plasticised material inside the hole [121]. Nicholas [112] assumes that a tapered hole configuration will assist the bond formation due to the additional forces on the tapered surfaces [112]. Investigations on the influence of the taper angle on the bond quality have not been reported so far.

As the consumable rod undergoes significant hot working during the welding process, a very refined hot worked microstructure was reported by Nicholas [112]. Owing to the superior static and dynamic properties of the weldment FHPP was suggested as a method of enhancing materials as well as for the production of monolithic materials and MMCs.

In the second part of his report Nicholas [112] presented microstructural and mechanical results of a mild steel FHPP weld in a C-Mn Steel substrate. Depending on the process parameters either a very refined microstructure across the whole weldment or refined regions which have not undergone layer shearing could be found. Nicholas [112] explains this with the balance between thermal transfer and material displacement. If the balance results in a heat flow along the stud, a part of the stud will shear off due to the thermal softening. Nevertheless, it was reported that both weld specimens had good bending and tensile test properties, while the exact values were not given.

Welding trials with aluminium alloys showed poor bonding quality with parallel hole configurations while the change to tapered hole and stud shape resulted in good bonding properties. This was explained by the extra welding force generated by the tapered surfaces and the reduced tendency to shear due to the increasing stud diameter [112].

Re-processing with FHPP of mild steel, cupro-nickel-chrome and nickel aluminium bronze results in significant increase in tensile strength (+ 54 % with mild steel), hardness and Charpy impact values (+ 220 % for mild steel) [112]. Welding mild steel studs (BS 970, 070 M20) in a carbon manganese plate resulted in 100-200 MPa higher tensile strength in the weld metal compared to the base material value [123]. Further investigations in this material combination resulted in maximum hardness values of 320 HV_5 in the HAZ and bend angles of 90-104° for single FHPP welds. Gibson [123] reported that Charpy impact tests on cylindrical stitch welds only gave a Charpy impact toughness of 23 % of the plate material value (+20 °C, notch at bonding line, T-position). These very low values were associated with oxide layers on the bonding interface.

The influence of additional gas shielding (although usually not required) on the FHPP process and properties was first mentioned by Nicholas 1995 [112], but later on presented in more detail by Thomas and Nicholas 1997 [115]. Welds have been performed with rotational speed and burn-off rate as welding parameters. The use of shielding gas enabled good weld properties to be produced at lower burn-off rates [115]. This would enable lower axial welding forces at the same rotational speed. Thomas and Nicholas [115] reported encouraging results by the use of shielding gas especially in butt or sleeve configurations avoiding the oxidisation in the gaps between the plates, whereas detailed test results were not reported.

Nicholas [112] indicated 1995 that the size of the machines required and the forces associated with FHPP was the most limiting factor for an extensive industrial use of the process.

Figure 3-2: State of the art FHPP weld. (DIN S235 Mild steel stud in a S690QL CrMo steel plate).

The first investigations and welding trials with a portable FHPP welding head have been described by Pauly 1999 [82]. In this work it has been successfully demonstrated that sound FHPP welds could be produced with a portable welding equipment. The main difference in the welding equipment used by Pauly [82] to the one used by Nicholas and Thomas [112, 115, 121, 122] is the possibility to apply rotational speeds up to 7000 rpm. This reduced the required axial force from up to 90 kN to less than 25 kN. Pauly [82] studied a number of different stud and hole configurations with encouraging results, although still leaving some lack of bonding at the bottom area of the hole at the end of this investigation (Figure 3-2). A macrograph of a weld from the investigations by Pauly [82] is shown in Figure 3-2. Although a distinct bonding line and a narrow HAZ can be seen, the quality of the bond to the sides was strong enough for a 180° bending test around the centre line of the stud.

Only at the transition from the side walls to the bottom area the width of the HAZ decreases significantly and lack of bonding can be found. The centre area of the bottom shows clear bonding defects, which was expected by Pauly [82] and which was not subject of the presented investigations.

Figure 3-2 can be considered as state of the art prior to the developments presented in the presented report. It should be emphasised that the satisfactory mechanical properties presented so far only state the quality of the bonding to the sides of the hole. Generally the bonding in the bottom area, especially in the transient to the sides, shows lack of bonding or poor bend angle in all publications.

3.2 NOMENCLATURE

The FHPP related nomenclature is not fully defined so far with a lot of similar names used for different process variations. The following list tries to define a couple of phrases related to FHPP. Those phrases will only be used in the given meaning within this work.

FHPP	Friction Hydro Pillar Processing. Friction welding process where a rotational welding consumable is friction welded in a bore hole. The welding consumable and the bore hole can be of different geometries and shapes, including a tapered configuration. In general the welding consumable plasticises across the whole diameter and across the whole welding depth. Un-plasticised local areas might occur.
Tapered Plug Welding	Friction welding process where a through-thickness hole is closed by friction welding a rotational welding consumable to the sides of the hole. The welding consumable is only plasticised near the surfaces and not across the whole diameter. Usually a tapered configuration for the consumables (plug) and the hole is used.
Stitch Welding	Application of the FHPP process where a number of FHPP welds are performed along a welding path, overlapping each other for a given distance. The bore hole for the following weld is drilled partially in the consumable stud of the prior weld. Used for the repair of longer cracks and joining plates with longer welding seams.
Tapered Stitch Welding	Stitch Welding with tapered holes and welding consumables.
Stud Welding	Friction welding process where a single rotational stud is welded on the surface of a workpiece.

4 MOTIVATION AND OBJECTIVES

In the late 80's and at the beginning of the 90's a number of portable friction welding machines have entered the market [14, 15]. These small and flexible machines were primarily designed for conventional friction welding and friction stud welding, making use of higher rotational speeds and reduced axial forces to produce metallic bonding. This new concept allowed the "in-situ" usage of friction welding in large components and existing structures [6, 119, 124, 125]. In parallel to that in the same period of time innovative friction welding processes have been developed, one of these being FHPP [16]. In 1997 it was demonstrated by Pauly and the author [82] for the first time world wide that portable systems could be successfully used to produce defect free FHPP welds, opening totally new perspectives for the application of this technology, particularly for the repair of offshore and marine structures [17, 18, 20, 126]. However, so far there was no systematic description of the mechanisms controlling bonding in FHPP welds. Moreover, the information on microstructural development during welding and the achievable mechanical properties available in the literature was, at its best, limited in scope. No studies on possible bonding mechanisms were reported in the literature.
Owing to the industrial relevance of this technology and the general lack of knowledge on process and properties the objectives of this study have been established as follows:

1) to establish the possible bonding mechanisms through a systematic analysis of thermal and mechanical phenomena taking place in FHPP.
2) to determine the effect of process parameters and joint configuration on microstructure and properties.
3) to determine the microstructural and mechanical properties of friction stitch welds in a steel grade applied in offshore and marine structures.

By fulfilling the above mentioned objectives it is intended to provide the industry with an alternative repair technology to conventional fusion welding processes providing superior properties, applicable to a range of materials and environmental conditions.

5 Experimental Strategy

Figure 5-1 illustrates the experimental strategy and the structure of the presented work. After the literature review on friction welding in general and FHPP in particular, the equipment and procedures used are presented in chapter 6. This chapter includes a detailed description of the different base materials used in the course of this work. Chapter 7 concentrates on the development of optimised welding parameters and stud and hole geometry combinations for HSLA steel. The influence of those variables on the plastification, material transport and the resulting properties is investigated in detail. A proposed bonding mechanism in FHPP is presented at the end of chapter 7 closing with a summary of the mechanical properties of FHPP welds in HSLA steel.

The application of FHPP stitch welds in a mild steel for the marine and offshore industry is addressed in chapter 8. After a process optimisation for this material, stitch welds were produced for systematic investigations of the mechanical properties. The results were finally discussed considering the classification society requirements.

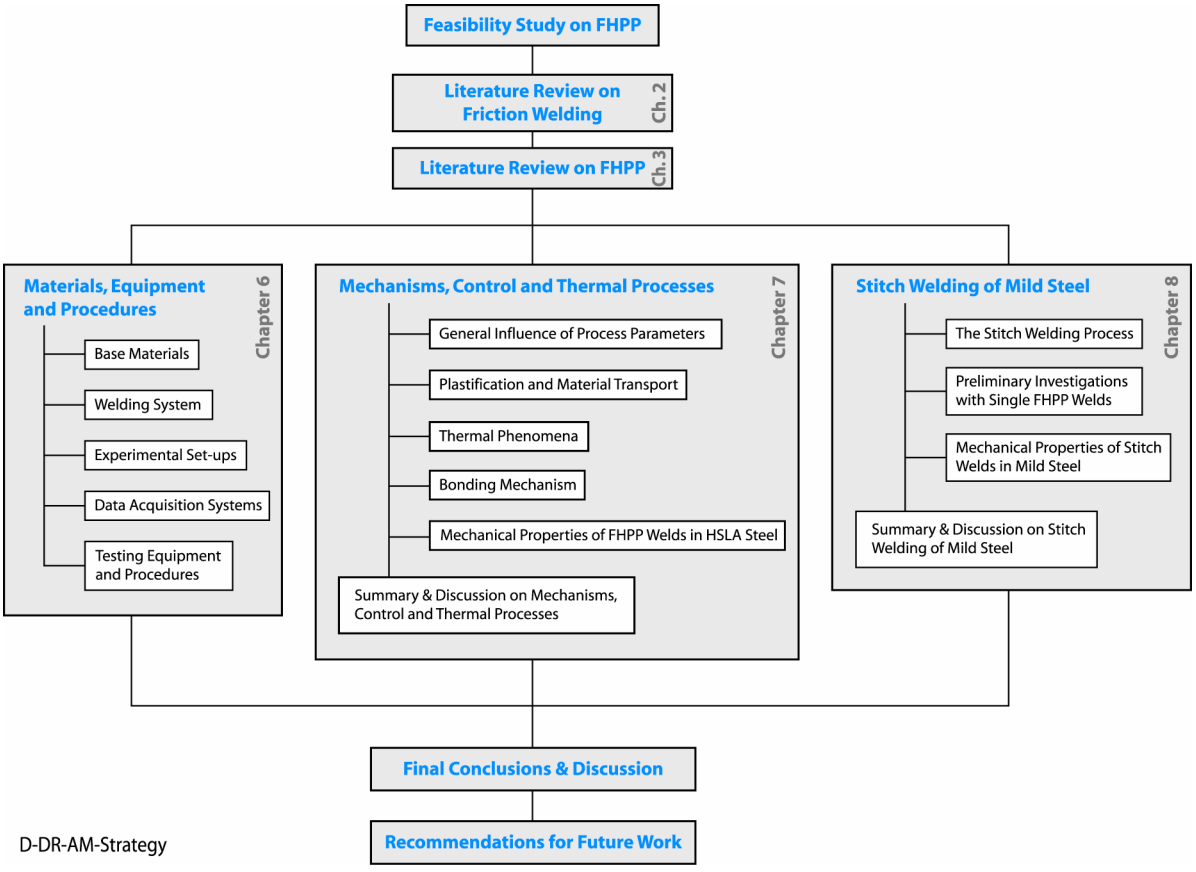

Figure 5-1: Experimental strategy of the present work with references to the main chapters.

6 MATERIALS, EQUIPMENT AND PROCEDURES

6.1 BASE MATERIALS

Three different steel grades have been used within this study. For the majority of experiments a high strength low alloy (HSLA) C-Mn pipeline steel has been used (API 5L X65). It is widely used as pipeline material for the offshore industry. In some experiments where thicker plates were needed a similar C-Mn grade (St460T, 1.8915) was used to machine the required base plates. All final stitch welds and the special preliminary experiments were performed in mild steel (S235, DIN EN 10025).
The material properties and chemical compositions will be presented in more detail in the following. The chemical analysis was done by mass spectral analysis; the carbon equivalent was calculated according to the following equation by IIW sub-commission IX-G:

$$C_{equivalent} = C + \frac{Mn}{6} + \frac{Cr + Mo + V}{5} + \frac{Cu + Ni}{15}$$

A material identification number will be used to relate the base materials to the appropriate welding experiments later on.

6.1.1 BASE MATERIAL 01 – API 5L X65 PIPE

A HSLA C-Mn steel according to the American Petroleum Institute standard API 5L for line pipes was supplied as 10” pipe for the initial welding experiments. Welding studs as well as base plates have been machined out of the pipe. It was mainly used for the welding experiments presented in chapters 7.1 and 7.2.

Table 6-1: Chemical composition of base material 01 – API 5L X65 pipe.

	C	Si	Mn	P	S	Al	N	Cu	Mo	Ni	Cr	V	Nb	Ti	B	Ca	Sn	$C_{äq}$
Manufacturer’s Certificate	0.100	0.270	1.400	0.011	0.001	0.042	0.010	0.090	0.030	0.070	0.090	0.043	0.013	0.002			0.008	0.377
Chemical Analysis	0.080	0.248	1.400	<0.20	<0.00	0.038		0.012	0.142	0.032	0.011	0.009		0.017				0.349

All values in weight percentage

Table 6-2: Mechanical properties of base material 01 – API 5L X65 pipe.

	Tensile Strength[1]	Yield Strength[1]	Elongation	Charpy Impact Values[2] [J]			
	[MPa]	[MPa]	[%]	+20 °C	±0 °C	-20 °C	-40 °C
Manufacturer’s Certificate	545	483	30	-	-	-	-
Own Test Results	561	478	27	-	-	-	-

[1] Mean Values of a least three specimens
[2] Mean Values of a least four specimens

6.1.2 BASE MATERIAL 02 – API 5L X65 PLATE

The material for all welding studs for the detailed investigations and evaluation of mechanical properties of FHPP welds was supplied as 22 mm thick plate of a HSLA C-Mn steel according to the American Petroleum Institute standard API 5L for line pipes.

Table 6-3: Chemical composition of base material 02 – API 5L X65 plate 22 mm.

	C	Si	Mn	P	S	Al	N	Cu	Mo	Ni	Cr	V	Nb	Ti	B	Ca	Sn	$C_{äq}$
Manufacturer's Certificate	0.080	0.340	1.450	0.016	0.003	0.029	0.006	0.190	0.009	0.170	0.029	0.070	0.033	0.016				0.367
Chemical Analysis		0.444	1.390	0.019		0.038		0.209		0.193	0.032			0.025				

All values in weight percentage

Table 6-4: Mechanical properties of base material 02 - API 5L X65 plate 22 mm.

	Tensile Strength[1]	Yield Strength[1]	Elongation	Charpy Impact Values[2] [J]			
	[MPa]	[MPa]	[%]	+20 °C	±0 °C	-20 °C	-40 °C
Manufacturer's Certificate	565	473	29.4	252	207	196	200
Own Test Results	538	437	30	-	-	236	-

[1] Mean Values of a least three specimens
[2] Mean Values of a least four specimens

The microstructure consists of a fine-grained ferrite matrix with distinctive pearlite lines (Figure 6-1). Figure 6-2 shows the mid-plate area with wider ferrite areas and pronounced bands of pearlite.

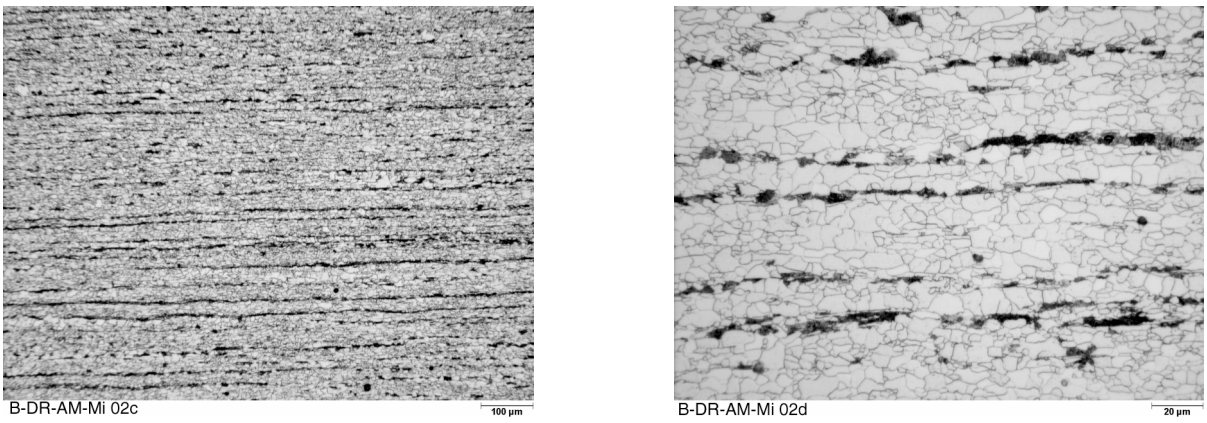

Figure 6-1: Microstructure of X65 stud base material (original magnification 100x and 500x).

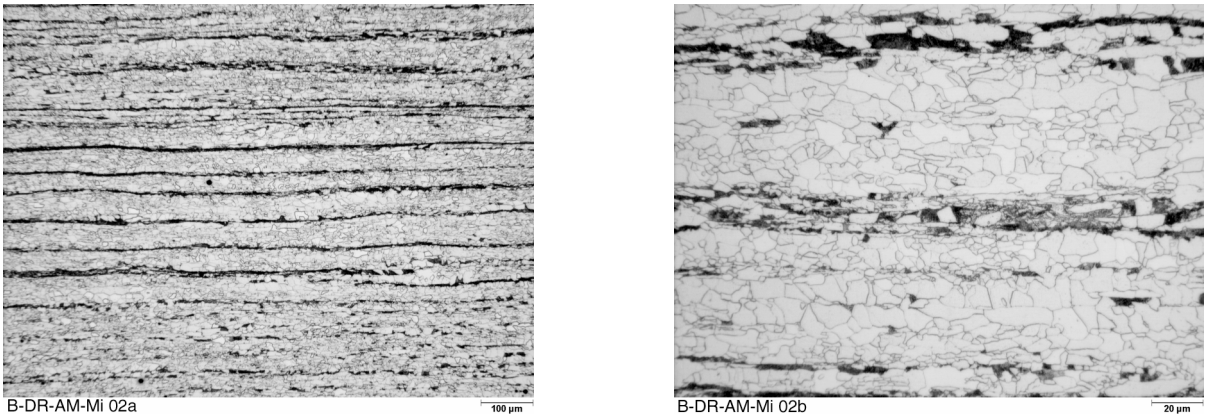

Figure 6-2: Microstructure of X65 stud base material, mid plate thickness (original magnification 100x and 500x).

6.1.3 BASE MATERIAL 03 – API 5L X65 PLATE

All base plates for the detailed investigations and evaluation of mechanical properties of FHPP welds were machined from a 25.4 mm thick plate in grade X65, according to the American Petroleum Institute standard API 5L for line pipes.

Table 6-5: Chemical composition of base material 03 – API 5L X65 plate 25.4 mm.

	C	Si	Mn	P	S	Al	N	Cu	Mo	Ni	Cr	V	Nb	Ti	B	Ca	Sn	$C_{äq}$
Manufacturer's Certificate	0.070	0.410	1.600	0.014	0.003	0.024	0.010	0.093	0.020	0.080	0.050	0.070	0.035					0.376
Chemical Analysis	0.051	0.450	1.590	0.011	<0.001	0.035		0.089	0.028	0.079	0.023	0.058		0.003				0.349

All values in weight percentage

Table 6-6: Mechanical properties of base material 03 – API 5L X65 plate 25.4 mm.

	Tensile Strength[1]	Yield Strength[1]	Elongation	Charpy Impact Values[2] [J]			
	[MPa]	[MPa]	[%]	+20 °C	±0 °C	-20 °C	-40 °C
Manufacturer's Certificate	575	506	30	264	287	257	279
Own Test Results	565	470	30.9	>300	>300	>300	>300

[1] Mean Values of a least three specimens
[2] Mean Values of a least four specimens

The microstructure consists of a ferrite matrix with distinct pearlite lines (Figure 6-3). The ferrite grain size decreases significantly from the mid plate thickness to the surfaces (Figure 6-4).

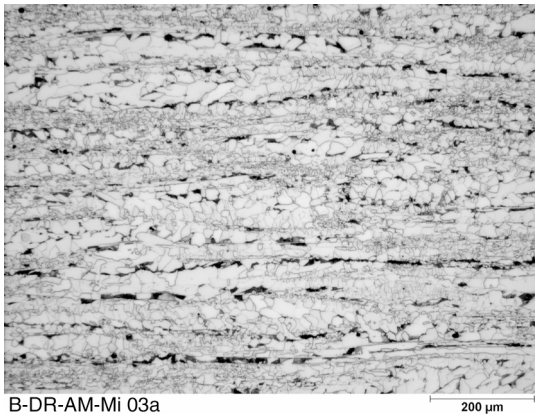

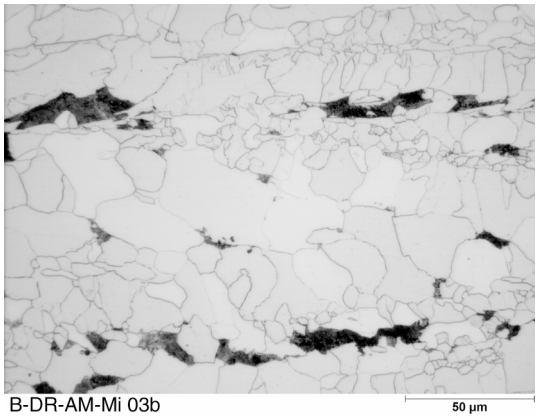

Figure 6-3: Microstructure of X65 plate base material, mid plate thickness (original magnification 100x and 500x).

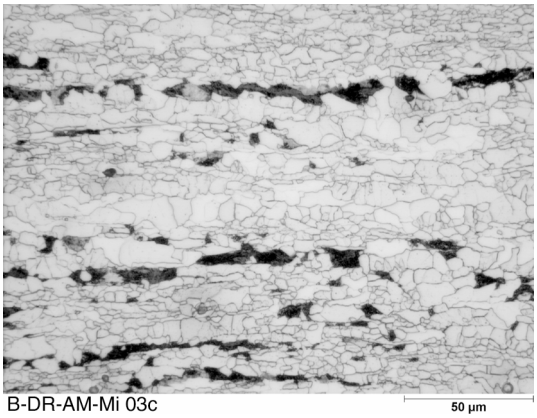

Figure 6-4: Microstructure of X65 stud base material, near plate surface (original magnification 500x).

6.1.4 BASE MATERIAL 04 – S235 BAR

All tapered welding studs for the mild steel welds in chapter 7.2 and the tapered stitch welds in chapter 8 were produced from 24 mm diameter round bar material according to the German DIN EN 10025 standard.

Table 6-7: Chemical composition of base material 04 – S235 bar.

	C	Si	Mn	P	S	Al	N	Cu	Mo	Ni	Cr	V	Nb	Ti	B	Ca	Sn	$C_{äq}$
Manufacturer's Certificate	0.140	0.220	0.610	0.012	0.033		0.010	0.330	0.011	0.080	0.080					0.001	0.013	0.287
Chemical Analysis		0.213	0.417	0.014		0.006		0.283		0.100	0.082			<0.001				

All values in weight percentage

Table 6-8: Mechanical properties of base material 04 – S235 bar.

	Tensile Strength[1]	Yield Strength[1]	Elongation	Charpy Impact Values[2] [J]			
	[MPa]	[MPa]	[%]	+20 °C	±0 °C	-20 °C	-40 °C
Manufacturer's Certificate	455	322	33	-	-	-	-
Own Test Results	441	300	36	-	-	99	-

[1] Mean Values of a least three specimens
[2] Mean Values of a least four specimens

Figure 6-5 shows the microstructure transverse to the rolling direction. A regular displacement of globular ferrite and pearlite can be found all across the bar.

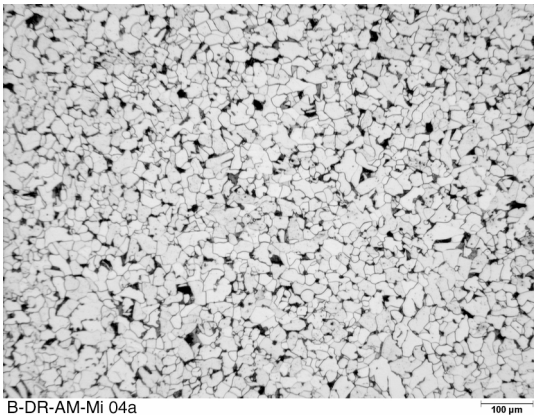

Figure 6-5: Microstructure of base material 04 - S235 bar (original magnification 100x).

6.1.5 BASE MATERIAL 05 – S235 PLATE

This material was supplied as 20mm plate according to the German DIN EN 10025 standard. The base plates for the initial tapered stud welds, as presented in chapter 7.2, were produced from this material. It should be noted, that this material showed extremely high Charpy impact values in the base material tests and low elongation values in the tensile tests.

Table 6-9: Chemical composition of base material 05 – S235 plate.

	C	Si	Mn	P	S	Al	N	Cu	Mo	Ni	Cr	V	Nb	Ti	B	Ca	Sn	$C_{äq}$
Chemical Analysis	0.073	0.170	0.450	0.020	0.030	0.020		0.190	0.020	0.070	0.110	0.020		<0.002				0.195

All values in weight percentage

Table 6-10: Mechanical properties of base material 05 – S235 plate.

	Tensile Strength[1]	Yield Strength[1]	Elongation	Charpy Impact Values[2] [J]			
	[MPa]	[MPa]	[%]	+20 °C	±0 °C	-20 °C	-40 °C
Own Test Results	425	405	16	295	>300	>300	>300

[1] Mean Values of a least three specimens
[2] Mean Values of a least four specimens

6.1.6 BASE MATERIAL 06 – S235 PLATE

All base plates for the tapered stitch welds presented in chapter 8 were produced from a 20 mm thick mild steel plate according to the German DIN EN 10025 standard.

Table 6-11: Chemical composition of base material 06 – S235 plate.

	C	Si	Mn	P	S	Al	N	Cu	Mo	Ni	Cr	V	Nb	Ti	B	Ca	Sn	$C_{äq}$
Manufacturer's Certificate	0.120	0.260	0.450	0.009	0.016	0.030	0.009	0.180	0.010	0.103	0.020	0.002	0.003	0.003				0.220
Chemical Analysis		0.309	0.365	0.012		0.029		0.199		0.125	0.043			<0.001				

All values in weight percentage

Table 6-12: Mechanical properties of base material 06 – S235 plate.

	Tensile Strength[1]	Yield Strength[1]	Elongation	Charpy Impact Values[2] [J]			
	[MPa]	[MPa]	[%]	+20 °C	±0 °C	-20 °C	-40 °C
Manufacturer's Certificate	437	332	32	146	-	-	-
Own Test Results	431	290	31	-	-	58	-

[1] Mean Values of a least three specimens
[2] Mean Values of a least four specimens

The microstructure exhibits pearlite lines in a globular ferrite matrix as shown in Figure 6-6.

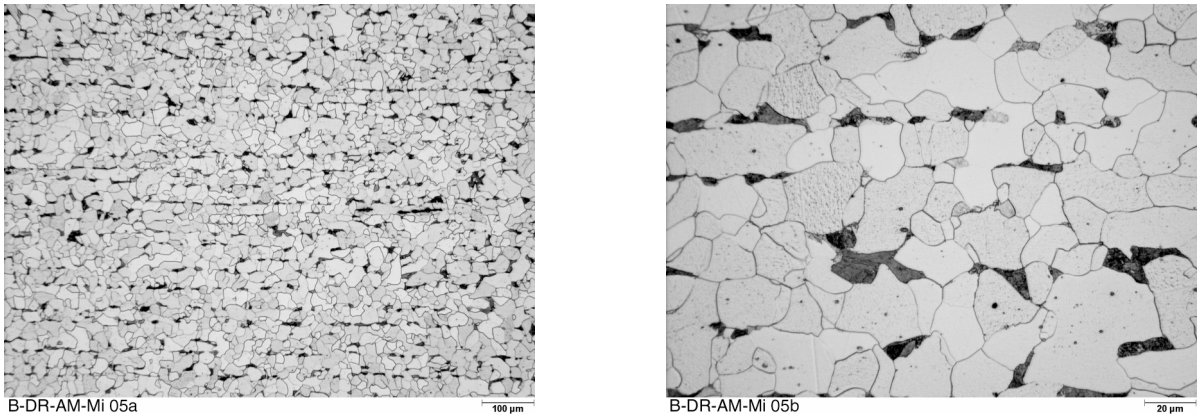

Figure 6-6: Microstructure of base material 06 – S235 plate (original magnification 100x and 500x).

6.1.7 BASE MATERIAL 07 – ST460T PLATE

This material was supplied as 50 mm thick plate according to the German DIN standard (St460T, 1.8915). Only the very thick base plates for the material flow experiments with the nickel tracer rod and the plates for the force measurements were machined form this grade. No mechanical properties of FHPP welds have been determined for this material.

Table 6-13: Chemical composition of base material 07 – St460T plate.

	C	Si	Mn	P	S	Al	N	Cu	Mo	Ni	Cr	V	Nb	Ti	B	Ca	Sn	$C_{äq}$
Manufacturer's Certificate	0.139	0.440	1.590	0.016	0.005	0.029		0.190		0.560	0.070	0.130	0.030					0.494

All values in weight percentage

Table 6-14: Mechanical properties of base material 07 – St460T plate.

	Tensile Strength[1]	Yield Strength[1]	Elongation	Charpy Impact Values[2] [J]			
	[MPa]	[MPa]	[%]	+20 °C	±0 °C	-20 °C	-40 °C
Manufacturer's Certificate	595	449	23	-	-	-	-

[1] Mean Values of a least three specimens
[2] Mean Values of a least four specimens

6.2 WELDING SYSTEM

The system used in the present study can be described as a hydraulically powered friction welding machine (Figure 6-7). It is designed and built as a portable friction stud welding machine for underwater use by Circle Technical Services Ltd. in Aberdeen. It is mainly used under water either by divers or by Remotely Operated Vehicles (ROV) to weld studs on steel structures [10, 11, 110, 124, 127, 128]. In all these applications the weld itself is controlled and monitored from above the water.

Figure 6-7: HMS 3000 Welding Head.

The system consists of four major components: the Hydraulic Power Unit (HPU), the valve block, the welding head and the control system:

HPU

In the configuration used, the HPU's pump is driven by a 50 kW electric motor supplying up to 115 l/min at 315 bar. The maximum oil pressure is continuously adjustable while the pump automatically adjusts the flow. Depending on the required power on the weld head the oil pressure might be lower than the maximum set value. In case of an idle run the pressure drops to the value required just to overcome the flow restriction in the system.

The HPU delivers the flow and pressure via a 60 m long hose connection to the valve block. Owing to these long hoses and their flexibility there is a significant delay in increasing the pressure after a sudden change in the required power. This phenomena lead to some problems specially at the first contact between the stud and the base plate (Touch Down) at very high rotational speeds where the system sometimes stalled due to the very low oil pressure.

Unfortunately the long hose connection was required due to the distance between the experimental site and the possible location for the HPU in the GKSS facilities. Nevertheless such distances could not be precluded for industrial applications.

Valve Block

The valve block regulates the oil flow and pressure supplied by the HPU. All operations of the weld head are driven by electrically controlled proportional valves on the valve block. Besides additional safety valves three pressure transducers are used to monitor the mainline pressure (supply from the HPU) and the two sides of the piston in the welding head (axial force). Supplementary to this standard configuration a number of additional sensors have been installed to allow a comprehensive monitoring of all system variables (see chapter 6.4). A flow meter and a temperature probe have been added to the main line to monitor flow changes and possible overheating of the hydraulic oil. Two pressure transducers are used to measure the pressure across the hydraulic motor of the welding head.

Weld Head

The portable weld head itself is approximately 600 mm long and 160 mm in diameter. It consists mainly of a hydraulic fixed displacement motor at the upper side and a hydraulic piston inside the lower cylinder. The piston can move the lower part of the shaft by 50 mm in axial direction and applies the required axial force. Welding consumables are fixed in the chuck at the lower end of the shaft. A metal proximity sensor on the shaft inside the housing monitors the rotational speed, while a linear proximity sensor (LIPS) measures the axial movement inside the piston. The weld head is attached to the welding rig and support structures by a bayonet connection on the housing.

Control System

The PC-based control system aquires the sensor information (rotational speed, axial position and piston pressures) and controls according to the welding parameter. This control system regulates the welding process by the burn-off (This is a burn-off controlled system). The welding parameters (rotational speed and axial pressure) can be changed a number of times during one weld. This gives a very flexible tool to respond to changes in the welding conditions during a single weld (i.e. changes in geometry). Process parameter sets are saved as “projects” by the control system. They can be defined before the actual weld takes place. The welding parameters are displayed in real time during a weld and stored within the projects. These diagrams can be printed or displayed again, but unfortunately no option is given to export the measured data. The need for a comprehensive monitoring of all system variables with access to the measured data led to the implementation of an additional data recording system (see chapter 6.4). The control system uses psi as pressure unit, hence the conversion to the SI unit bar results in uneven values for the axial pressure.

6.3 EXPERIMENTAL SET-UPS

A basic stand supplied by the weld head manufacturer has been used for most of the welding experiments and system trials (Figure 6-8). The welding head can be fixed on top of the stand in a vertical position with its bayonet ring. Welding specimens were held in place in a vice after alignment of the bore hole and the welding stud. The distance between the vice and the welding head can be easily adjusted to different specimen heights by means of a screw jack.

The beam with the vice can be replaced by an optional water basin which has been specially built for under water welding trials. This basin allows welds to be produced in a wet environment without the need to submerge the entire welding head under water and with cooling conditions similar to the under water environment.

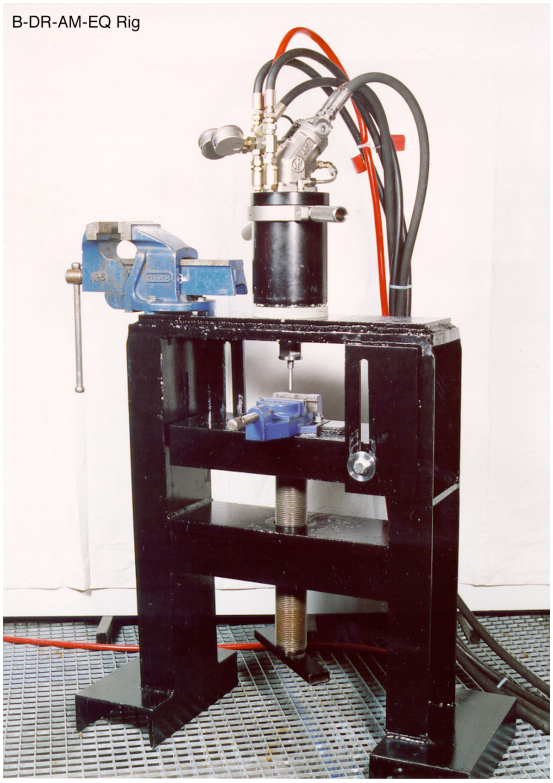

Figure 6-8: Basic welding stand.

In order to weld bigger specimens a new rig was designed and built (Figure 6-9). The weld head is fixed via a bayonet coupling in a stiff gantry on a plate. The beam can be adjusted in height for different specimen sizes with two screw jacks. The specimen can either be fixed directly to the thread matrix on the table with common clamping devices or in case of standard 50x50 mm plates in an additional fixture with quick tensioner. This modular design allows satisfactory visibility and accessibility in handling welding samples and for measuring systems.

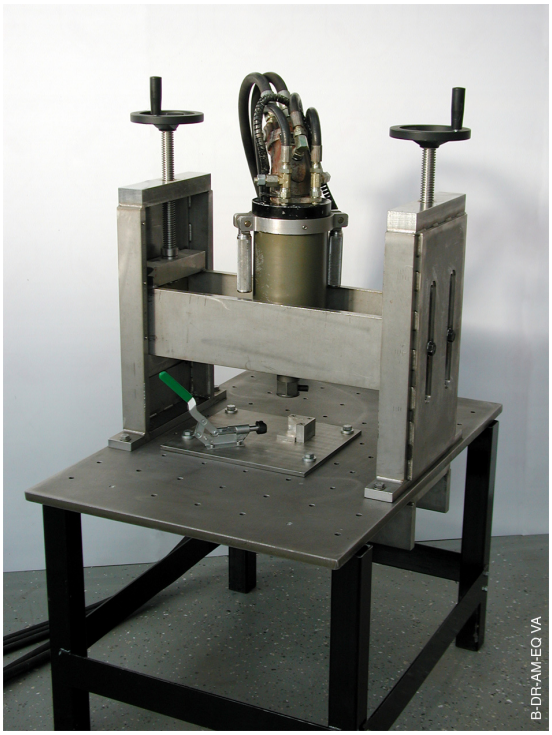

Figure 6-9: New welding table with quick tensioner fixture.

6.4 DATA ACQUISITION SYSTEMS

6.4.1 DATA RECORDING SYSTEM – DRS

As mentioned in chapter 6.1 an additional measurement system was needed for acquisition and processing of process parameters and complementary data. This system was set-up by Pauly [82] and denominated Data Recording System (DRS).
The DRS is used to measure and store the welding parameters and additional signals for every weld (see Table 6-15). The system is based on a standard PC connected to National Instruments hardware for signal conditioning. The software was programmed in LabView and gives real time diagrams from all signals generated during the welding. Data can be stored and exported for further evaluation and analysis. Owing to the fact that all sensors are processed by a single unit, including signals generated by the welding control system, reference among all data (welding parameters and system variables) is possible. The DRS records data with 100 Hz per channel.

Table 6-15: Measured and calculated signals in the DRS.

Measured Data	Calculated Data
Rotational speed	
Axial position of piston	Burn-off distance
Hydraulic pressure on both sides of the piston	Axial force
Main line flow	
Oil temperature in main line	
Main line hydraulic pressure	
Hydraulic pressures to and from weld motor	Torque and power (not automatically processed by DRS)

Data files have been stored for every weld produced in this study. These files were then transferred into standard data processing software for further processing as well as for complementary evaluation. Table 6-16 shows a set of exemplary welding parameters as programmed in the weld head control system. The respective welding graph with the most important parameters is shown in Figure 6-10. The current power is calculated and added in this diagram already.

Table 6-16: Exemplary set of welding parameters.

Geometry Type E		
Axial Pressure [bar]	Burn-off [mm]	Rotational Speed [rpm]
34.48	2	7000
34.48	2	6000
34.48	6	5000
34.48	Hold for 3 sec.	-

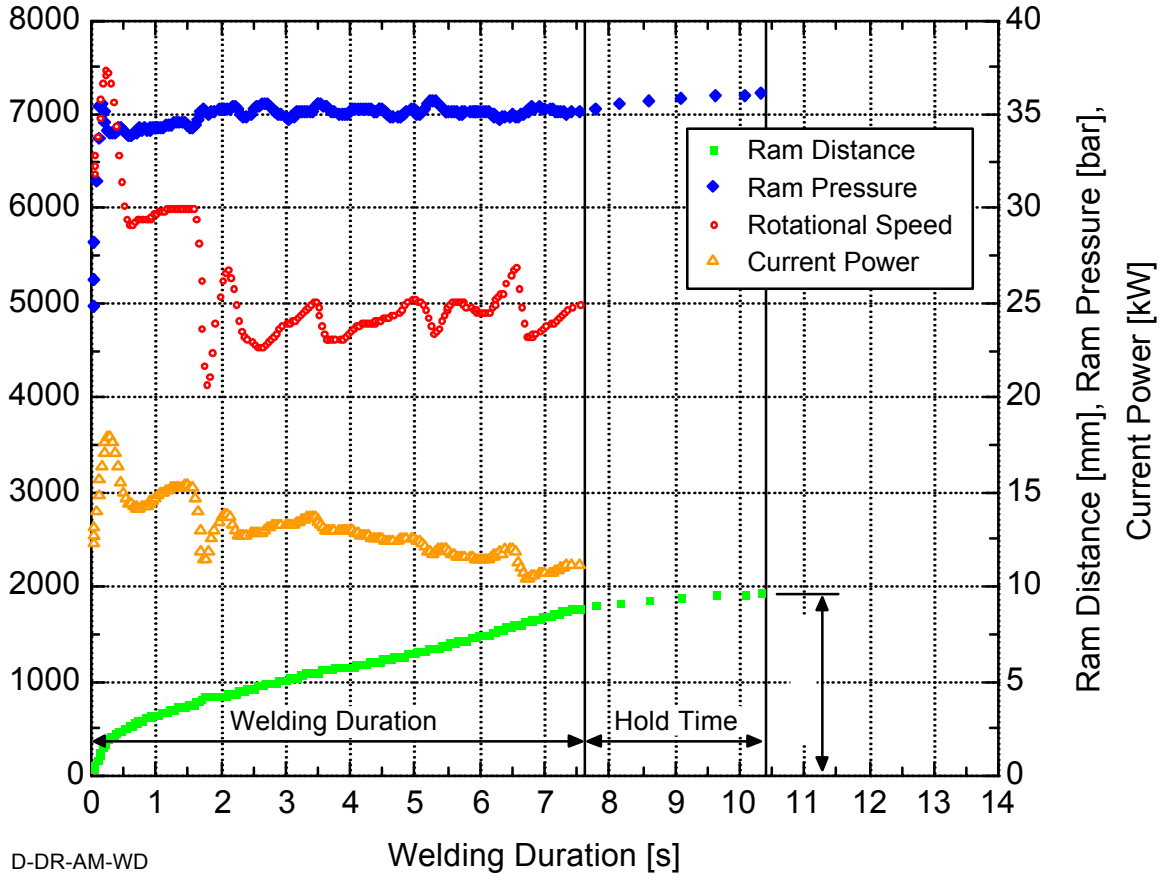

Figure 6-10: Exemplary welding diagram.

6.4.2 Temperature Measurements

For experiments on thermal phenomena presented in chapter 7.3 a special measuring system based on signals generated by thermocouples has been devised, programmed and assembled (Figure 6-11).

Figure 6-11: The Thermocouple measuring system.

This is a PC based measuring and data acquisition unit. The PC is connected to National Instruments SCXI-hardware for signal conditioning. The software was programmed in LabView and generates real time diagrams during measurement. Data can be stored and exported for further evaluation and analysis. Up to 32 thermocouples can be recorded simultaneously with a maximum of 50 Hz per channel. The measurements for this study were all recorded at 50 Hz. The software allows different types of thermocouples and includes the possibility to calibrate the signals. Calibration curves for the different types of thermocouples are already implemented in the LabView software package to convert the electromotive force (mV) into the appropriate temperature (°C). Heating and cooling rates can be calculated for individual temperature ranges (i.e $\Delta t_{8\text{-}5}$).

6.4.3 Internal Pressure Measurements

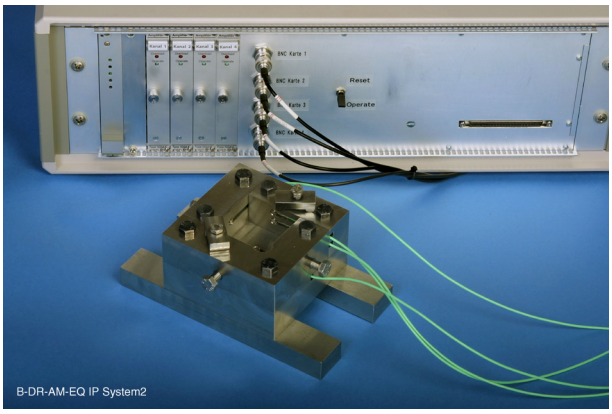

Figure 6-12: The load cell measuring system - Load cell device in the front with four load cells, amplifier and signal conditioning in the back.

A special measuring system has been designed and built for experiments on bonding mechanisms presented in chapter 7.4. Four miniature piezo-electric load cells and respective amplifiers were connected to National Instruments data acquisition hardware (Figure 6-12). The four load cells can be simultaneously recorded with 10 kHz per channel. The software produces a real time diagram at a reduced frequency. Further analysis of the data was carried out with standard data processing software. Measurements were started by a trigger signal from the DRS. This ensured that the data measured by both systems have the same time base.

6.5 TESTING EQUIPMENT AND PROCEDURES

6.5.1 WELDING PROCEDURE

The welding studs and plates were permanently marked prior to preparation for a welding trial. Studs and plates were then degreased and cleaned with Acetone to avoid any influence of machining liquids. The stud is fixed in the weld-head chuck and aligned with the hole in the welding specimen. All welding parameters have been previously typed in the control system and can now be loaded by a reference number. The DRS system and the weld control are manually started and the weld is performed according to the given welding parameters. The rotational speed is started first and after the required speed is reached, the piston is moved out and the stud is moved into the hole and makes contact at the bottom. At this point the axial movement is measured as burn-off. The rotational speed and axial pressure might be changed during the weld after pre-set steps of burn-off. When the full burn-off distance is reached, the rotational speed is stopped, but the axial pressure is kept constant for another three seconds. Afterwards the pressure is released and the specimen was taken out from the fixture.

6.5.2 OPTICAL MICROSCOPY

The microstructural characterization has been conducted on cross-sections of welded specimens, including the base material, HAZ and stud material. Specimens were cut in the centre of the stud across the base plate following grinding and polishing with diamond paste down to 1 µm using standard metallographic techniques. The etching solution used for all specimens was 3 % Nital.
After preparation specimens were analysed by optical microscopy using a Reichert-Jung microscope, model MeF3.

6.5.3 HARDNESS TESTING

Selected cross-sections were subjected to Vickers micro hardness measurements according to DIN EN 1043-2 [129]. The measurements were taken in rows as illustrated in Figure 6-13. Complete profiles across the whole weld as shown in Figure 6-13a were used for detailed characterisation, while the short profiles just across the bonding line (Figure 6-13b) were used to evaluate the effect of individual parameter sets and weld zone geometry on the resulting microstructure.
A load of 200 p was applied for 5s with a distance between indentations of 0.2 mm. The surfaces to be tested were properly prepared and etched, in order to enable the correct identification of the different zones of the welded joint. The hardness tests were performed on a Shimadzu Hardness Testing System (HMV – 2000) with a computer controlled specimen transport and indentation.

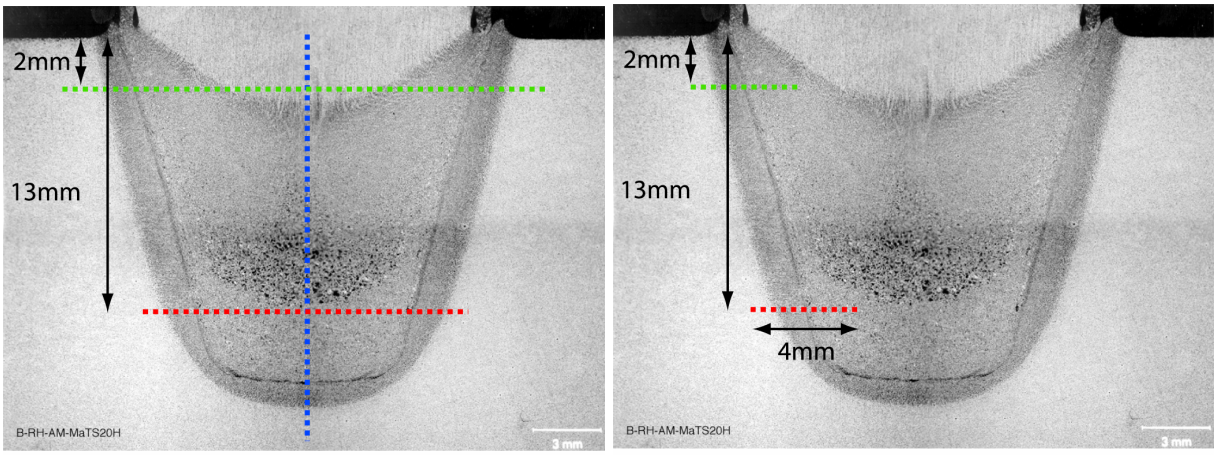

B-DR-AM-CH 3xHV B-DR-AM-CH 2xHV

Figure 6-13: Position of hardness profiles on welded specimen.

6.5.4 Bending Test

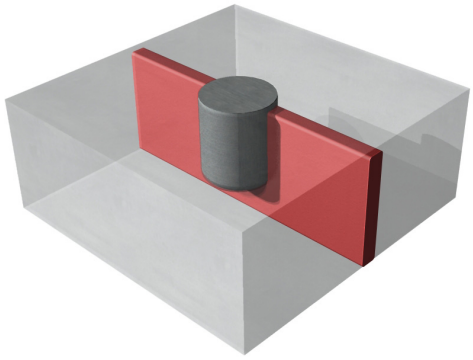

Figure 6-14: Position of bend specimen in welded samples.

Specimens for bending tests were machined from selected welds to evaluate the bonding quality. A purpose built three-point bend test rig was designed and built by Pauly [82] for sub-standard specimens according to DIN EN 910 and AWS D3.6M:1999 [130, 131]. The bending test specimens were machined from welded samples as shown in Figure 6-14. The outer surface of the specimens was polished and etched before machining to enable correct identification of failure location. Specimens were then tested with the punch positioned at the centre line of the weld region. The test was stopped at the onset of failure occurring on the outer surface and the final bend angle was measured.

6.5.5 TENSILE TESTING

Uniaxial tension tests have been carried out on base material and on welded joints according to DIN EN 10 002 and DIN EN 895 [132, 133]. For the base metal and single weld characterisation round specimens with 5 and 8mm diameter were used, positioned at the middle-thickness. The tests were performed with a deformation rate of 0.5 to 1 mm/min using a Zwick testing machine (200 kN capacity).

Stitch welded samples and S235 base material was tested using flat tensile specimens (25x17mm cross section). The tests were performed with a deformation rate of 2 mm/min using a Zwick testing machine (200 kN capacity).

All specimens were extracted transversely to the rolling direction and tested at room temperature. The results were expressed in terms of yield strength, ultimate tensile strength and elongation.

6.5.6 CHARPY IMPACT TESTING

Impact toughness tests have been performed with Chapy-V specimens according to DIN EN 10 045 and DIN EN 875 [134, 135]. Specimens were machined from base material, single welds and stitch welds at 7 mm distance from the plate surface (Figure 6-15). The notch was oriented normal to the plate surface for all specimens (T-Position) at the bonding line or at the centre of the stud. All specimens were extracted transversely to the rolling direction.

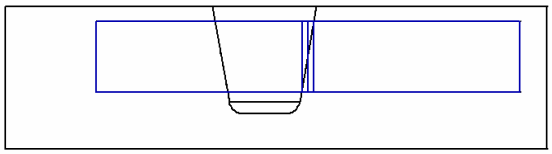

Figure 6-15: Position of Charpy impact specimen in a single-weld base plate.

6.5.7 MICRO FLAT TENSILE TESTING

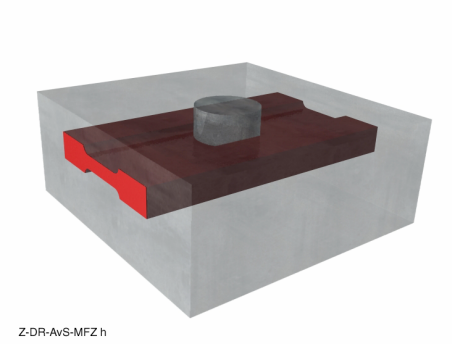

Figure 6-16: Specimen position for micro flat tensile tests horizontally across a weld.

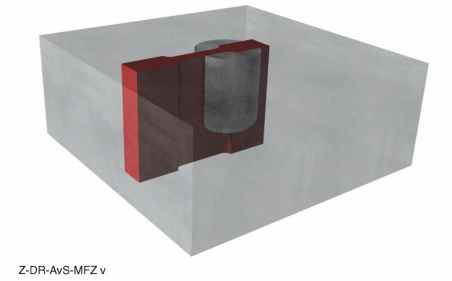

Figure 6-17: Specimen position for micro flat tensile tests vertically along the bonding line.

The variation in local tensile properties across the joint and along the depth of the weld has been determined using flat micro tensile specimens. In order to determine the properties across the weld, blocks were extracted horizontally through the base plate at 7 mm from the top as shown in Figure 6-16. For the properties along the depth of the weld, blocks have been extracted along the bonding line through the full plate thickness (Figure 6-18). Individual specimens were cut continuously along the blocks by spark erosion. The micro flat tensile concept has been presented by Çam et.al. [136] including comparison with round tensile specimens test results.

The tests were carried out with a deformation rate of 0.2 mm/min on an Instron testing machine. The results were expressed in terms of tensile properties, strength gradient across the joint and elongation.

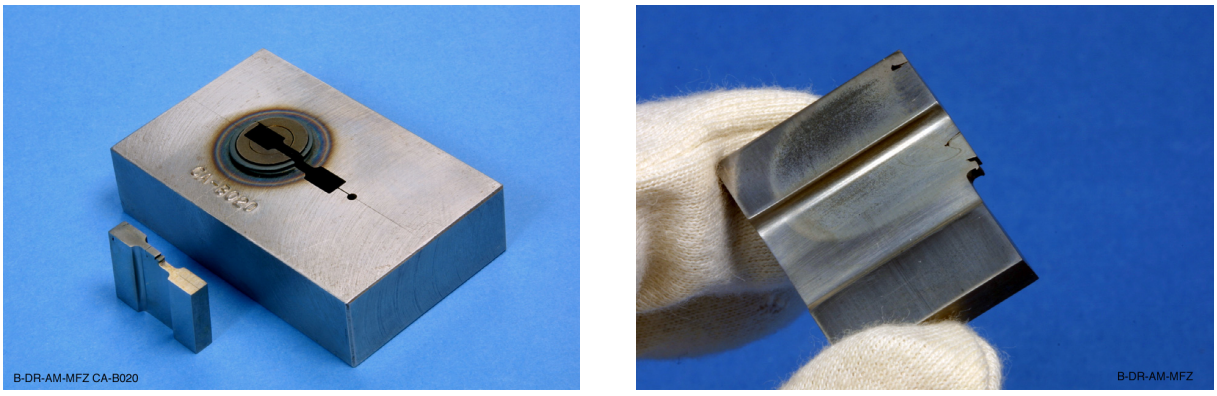

Figure 6-18: Welded specimen with block cut out for micro flat tensile tests along the depth of the weld.

7 MECHANISMS, CONTROL AND THERMAL PROCESSES OF FHPP

In the following chapter the experiments performed in order to analyse the different influences of process parameters will be presented. Based on the results reported by Pauly [82] and provisional experiments carried out by the author [17, 18, 20] initial stud and hole configurations were chosen taking into account optimum system behaviour and achievable mechanical properties. The welding parameters and the stud and hole configurations were further modified and optimised for the chosen material combinations. A detailed investigation of the processes and resulting properties is presented in the following chapter. The evaluation of the mechanical properties is mainly focused on the area of 7mm distance to the plate surface (half the weld depth).
Finally the bonding mechanisms are described based on the measurements and results presented in the following.

7.1 GENERAL INFLUENCE OF PROCESS PARAMETERS

The influence of the welding parameters on bonding quality, size of the HAZ and hardness values has been investigated within the mechanical limits of the system for a given geometry combination.
As described in chapter 2.4 the main welding parameters (i.e. rotational speed and axial force) should influence the size of the HAZ and the hardness values through changes in heat generation. Higher rotational speeds should result in a lower burn-off rate and a longer heating time. This should result in a larger HAZ and lower hardness values. Higher axial forces should promote bigger burn-off rates, shorter heating times, smaller HAZ and higher hardness values (see Figure 2-10).
Whereas the burn-off is a main welding parameter in standard friction welding the influence in FHPP is rather small. In FHPP a certain amount of burn-off is required to fill the hole completely, but it does not influence the mechanical properties as it does in conventional rotational friction welding (see chapter 2.4.4). If the burn-off is set too small, the hole will not be filled up to the surface. While if the burn off is too big, much stud material is plasticised on top of the weld, heating the consumable stud and the base material and extending the welding time.

7.1.1 EXPERIMENTAL PROCEDURE

For the following experiments all welding studs and base plates have been machined from base material 01. Chemical composition and mechanical properties of this base material have been reported in chapter 6.1.1. A geometry combination of a 8mm diameter stud and a 10mm diameter hole as used by Pauly [82] was chosen as illustrated in Figure 7-1. Minor bonding defects especially at the bottom of the hole were expected but were not a matter of concern at this stage.

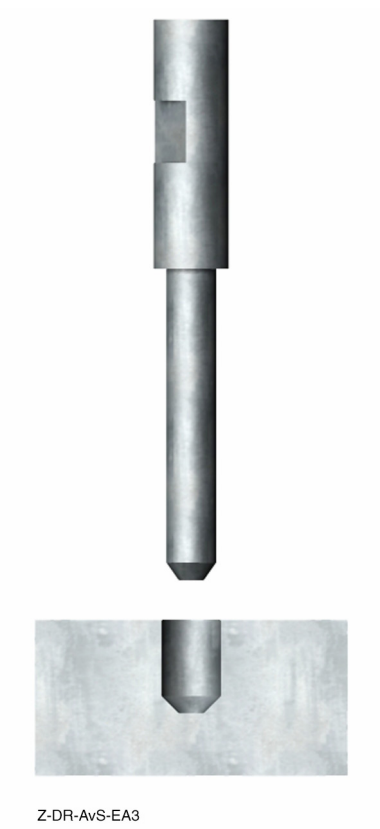

Figure 7-1: Stud and plate geometry used for parameter influence experiments.

A parameter matrix was devised and extended to the mechanical limits of the system. Derived from the knowledge of previous experiments [18, 20], welds outside the chosen parameter window led either to stalling of the weld head motor or to insufficient bonding throughout the whole weld.

The rotational speed was changed from 4000 to 7500 rpm in 500 rpm steps, while the axial pressure of the piston was changed from 6.90 to 24.14 bar in 3.45 bar steps. The burn-off was set to 10 mm for all welds based on the experiments presented by Pauly [82]. Two welds for each parameter combination have been produced. All welds have been recorded with the DRS (see chapter 6.4.1).
All specimens were cut at the centre of the weld and polished for visual examination and hardness measurements. Vickers micro hardness measurements with a load of 200 p ($HV_{0.2}$) have been taken from all specimens as described in chapter 6.5.3.
The recorded welding data were used to calculate the burn-off rates and the heating time for the individual welding parameter combinations.

7.1.2 Results

All welds show bonding in the upper region but lack of bonding at the bottom part as shown in Figure 7-2. None of the welds stalled or showed insufficient sidewall bonding throughout the examined parameter matrix. Visual analysis of the HAZ's shape and size showed that subjectively the size of the HAZ increases with rotational speed. The influence of the axial force is less significant, but the tendency to smaller HAZs with higher axial pressures is noticeable.
The hardness test results will be presented related to the parameter influences in chapter 7.6.1.

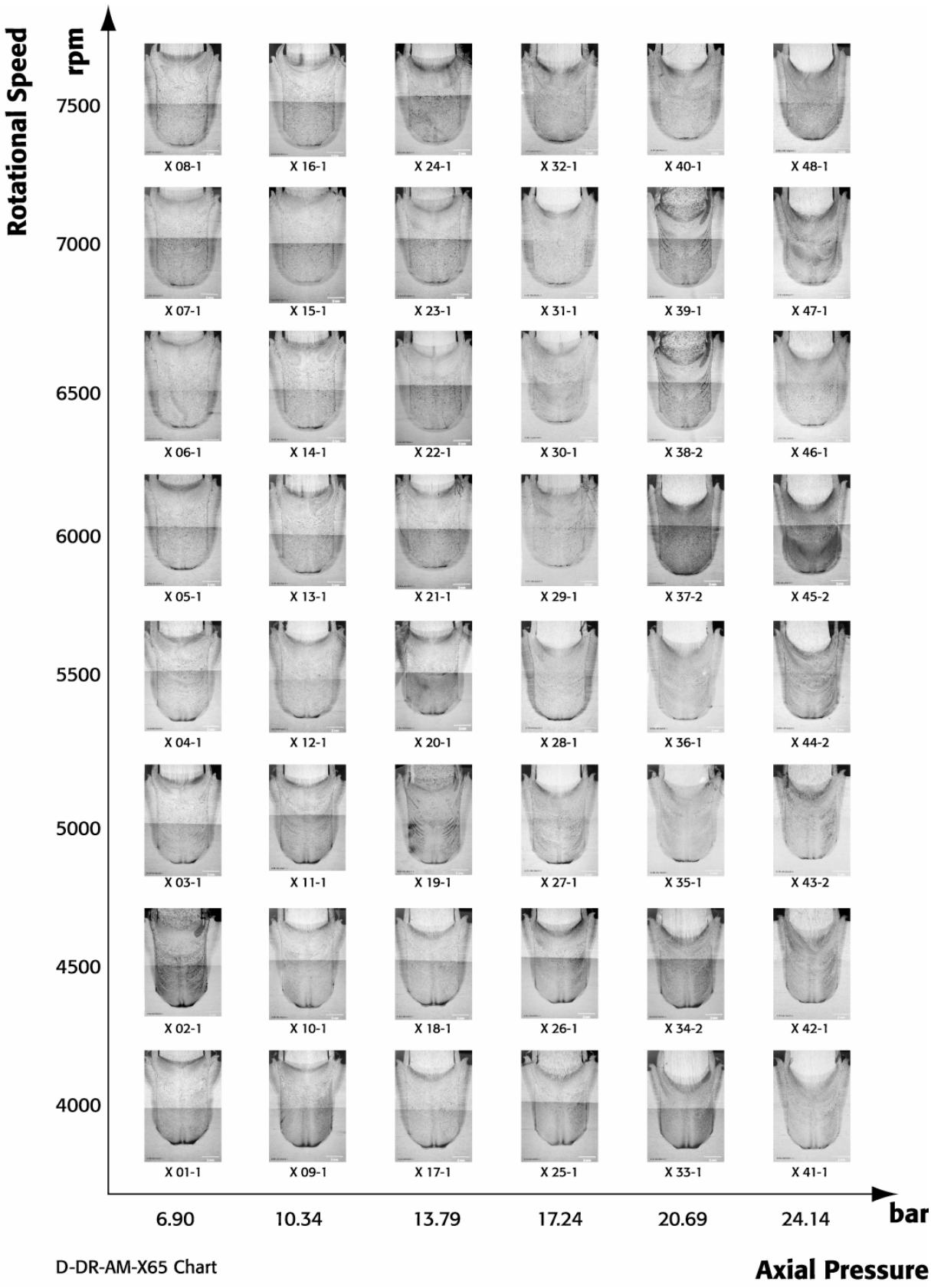

Figure 7-2: Macrographs of parameter matrix.

The heating times and burn-off ratios were calculated from the DRS measurements. Figure 7-3 presents the effect of axial pressure on heating time. The heating time is the measured time in seconds between the initial contact of the stud at the bottom of the hole (touch down) and the end of the weld when the rotation stops. It was found that the heating time reduces significantly with increasing axial pressure, but shows smaller variation with rotational speed (Figure 7-3).

The burn-off ratio (expressed as a mean value) is the ratio between the total burn-off and the heating time. Owing to the fact that neither the welding parameters nor the geometry of the studs changed during the welds the burn-off ratio is rather constant during a weld. In Figure 7-4 the axial pressure is plotted versus the burn-off ratio. As expected, the burn-off rates increase with increasing axial pressure.

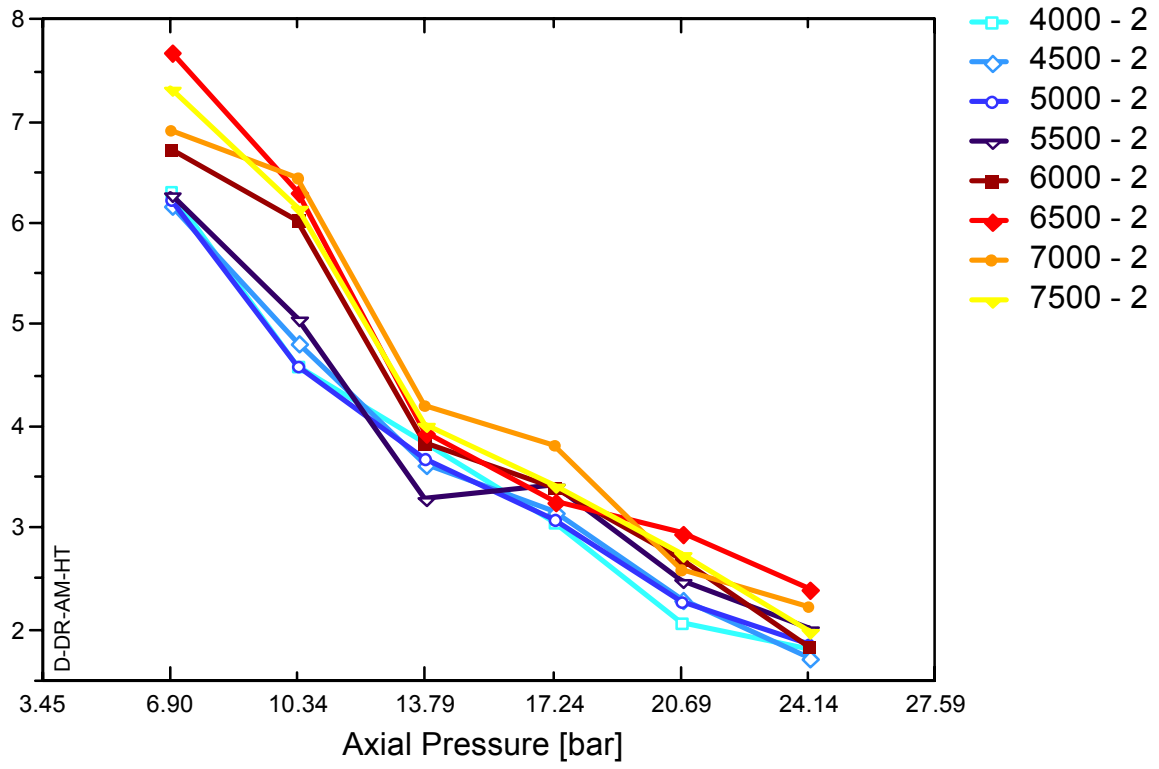

Figure 7-3: Heating time vs. axial pressure for different rotational speeds.

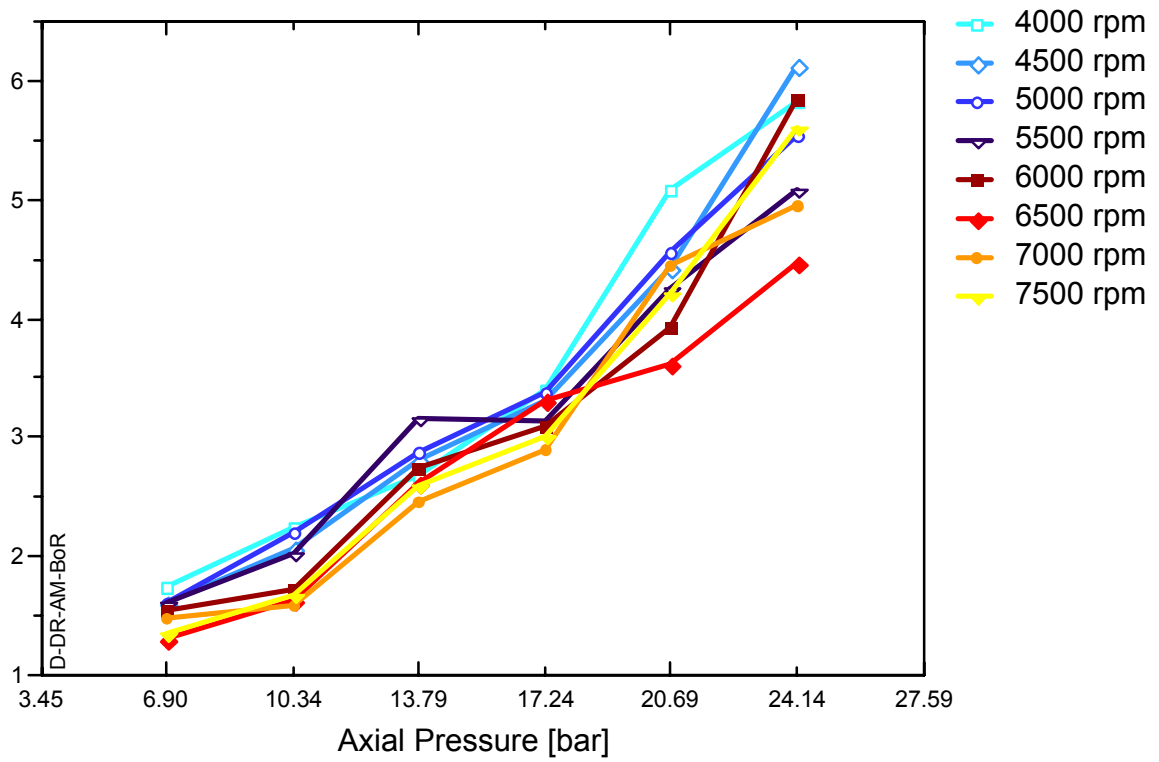

Figure 7-4: Burn-off rate vs. axial pressure for different rotational speeds.

7.2 Plastification and Material Transport

Not only the welding parameters themselves have a major influence on the quality of the weld, but apparently the stud and hole shape have possibly an even bigger influence. In order to gain a better understanding for the material flow and the characteristics of the plastification in a FHPP weld, a number of experiments were performed. Based on the knowledge gained with the first experiments in this context a new stud and the hole geometry could be developed which resulted in full bonding all around the interface. The experimental procedure within this chapter is illustrated in Figure 7-5.

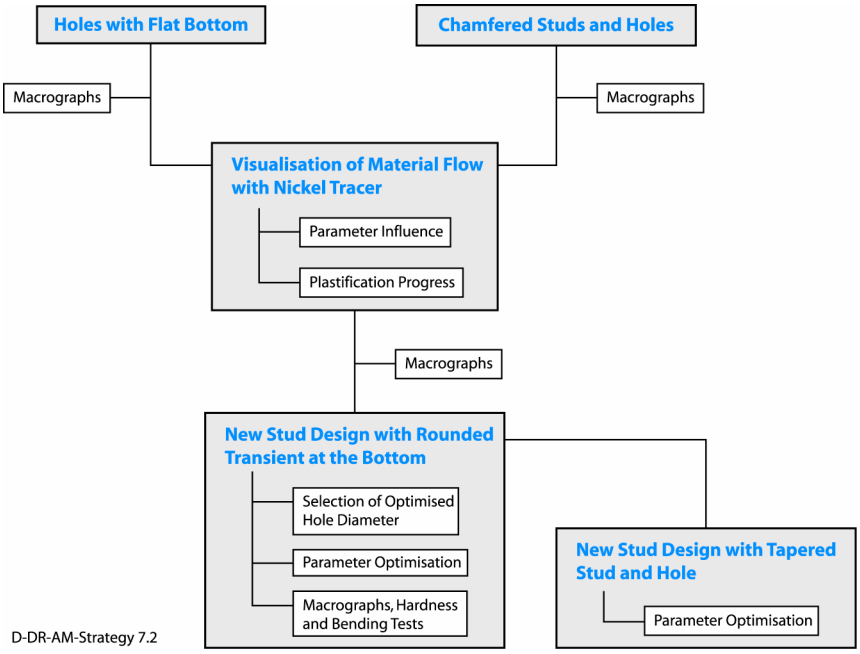

Figure 7-5: Experimental procedure of chapter 7.2

7.2.1 Experimental Procedure

The welds performed within this chapter were all subjected to visual examination of the cross sections on an optical microscope. Some specimens were used for micro-hardness measurements, usually performed in two horizontal lines in 2 and 13 mm distance from the plate surface. Certain specimens were subjected to bend tests as described in chapter 6.5.4. First experiments on the stud and hole shape were reported by Pauly [82]. Starting from a standard drill hole and a cone tip on the stud the author [82] examined hemispherical and flat tips as well. However, none of these geometries gave full bonding all around the interface. Based on these results two different approaches were examined. A hole with a flat bottom was used with studs with different tip designs (Figure 7-6). The hypothesis behind these welds was that small angles between the hole surface and the stud would immediately press the plasticised material out of the interface resulting in insufficient heating of the base material and poor bonding. The cone angle on the tip of the stud varied in steps from 0°, 10°, 20° to 30°. Welds were performed with a constant rotational speed of 5000 rpm and axial pressured of 10.34 and 20.69 bar. The welds were cut and visually observed in an optical microscope (see chapter 6.5.2).

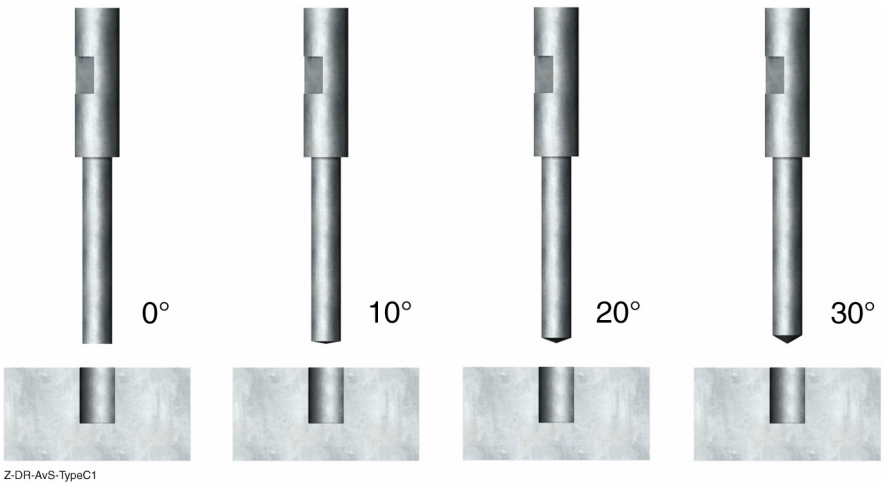

Figure 7-6: Stud and hole geometries with flat bottom.

In the second approach chamfered hole bottoms and stud tips were used (Figure 7-7). The angle on the stud chamfer varied from 45°, 50° to 55°, while the one on the hole bottom was kept constant at 45°. This means that in the combination with 45° chamfer angle the entire tip of the stud made contact with the bottom of the hole at the beginning of the weld. Welds were performed with a constant rotational speed of 5000 rpm and axial pressure of 10.34 or 20.69 bar for the first 3 mm burn-off. The rest of the weld was completed with 20.69 bar axial pressure. The intention in starting the weld with lower axial pressure was to reduce the burn-off ratio at the beginning and thus increase the heating duration at the bottom of the hole. A reduced axial pressure would also reduce the peak torque on the motor at touch down. The welds were cut and visually observed on an optical microscope (see chapter 6.5.2).

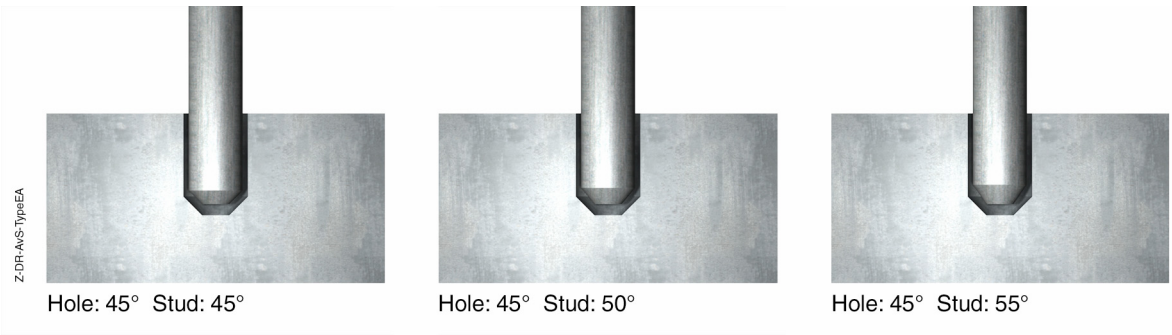

Figure 7-7: Chamfered stud and hole geometries.

In order to visualise the plastification and the material flow during a FHPP weld a Nickel rod was inserted in the welding stud as a tracer material. Eichhorn [87] reported similar experiments to visualise the material flow in conventional rotational friction welding. A Nickel welding consumable for Tungsten Inert Gas (TIG) welding with 2 mm diameter was pressed in the centre of the lower end of the welding consumables (Figure 7-8). Nickel stays unaffected by the etching solution (Nital) and could therefore be used to trace the material flow of the stud.

The geometry was similar to the chamfered ones described in the previous experiments (45° and 55°). The stud diameter was 8 mm, the hole depth was increased to 30 mm to get a certain distance of the weld which is not affected by any bottom or surface influences. The material used for the base plates was an St460T as presented in chapter 6.1.7.

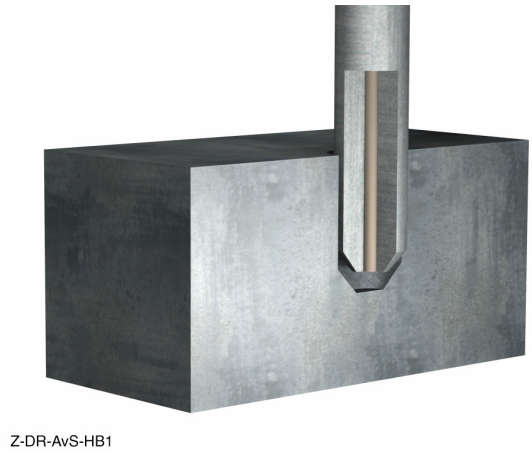

Figure 7-8: Stud design with nickel tracer rod.

Figure 7-9: Optimised stud and hole geometry combination.

Two different experiments were performed with these special studs. On the one hand the influence of welding parameters was visualised in a small 3x3 parameter matrix (2000, 5000 and 8000 rpm, 6.90, 13.79 and 20.69 bar). In addition to this, 8 welds were produced with 5000 rpm and 20.69 bar axial pressure. Only one of these was really welded to the full burn-off, all the others were stopped earlier with decreasing burn-off distances down to only 1 mm. Macrographs of these cross-sections should give information on how the plastification and the material flow progresses during the weld.

Based on the knowledge gained in the experiments mentioned above an optimised stud and hole geometry combination was developed and examined (Figure 7-9). Not only the stud diameter was increased but also the hole geometry at the bottom was changed to a flat bottom with rounded transition to the cylindrical hole. Different combinations of hole diameter (10.5, 11, 12 and 13 mm) with constant stud diameter (10 mm) were investigated. Studs were machined from base material 02, while the plates were made of base material 03 (see chapter 6.1.2 and 6.1.3).

Optimal welding parameters for 12 mm hole diameter were established with a 4x3 parameter matrix. All welds were visually examined with the optical microscope. Selected specimens were subjected to hardness testing as well.

Finally another geometry combination based on a tapered stud and hole was designed and extensively tested (Figure 7-10). It is expected that the forces on the bonding line increase due to the taper stud and hole shape. The additional forces should increase the overall bonding properties and extend the parameter window to lower axial forces. The tapered geometry focuses on thinner plates, as the weldable depth is limited by the maximum stud diameter of the welding system. Hole depths of more than 20 mm are probably not weldable in the tapered stud geometry with the welding system employed in this study.
The selected material for these tests was therefore already focused on possible applications in the marine and offshore industry. The material used was a mild steel DIN S235; base material 04 for the studs and base material 05 for the plates (see chapter 6.1.4 and 6.1.5). After preliminary trials optimised welding parameters were investigated with a 3x6 parameter matrix. All welds were visually examined with the optical microscope. Selected specimens were subjected to hardness testing, bend testing and Charpy toughness testing as described in chapter 6.5.

Figure 7-10: The tapered stud and hole design.

The welding parameters for tapered geometries are different from the ones for cylindrical holes, as the rotational speed is reduced in steps with the burn-off distance. This keeps the maximum relative velocity in a comparable range all along the weld. Usually the axial pressure is not changed during the weld in order to allow comparison of different weld geometries.

7.2.2 Results

The macrographs of the welds with different cone angles at the tip of the stud (Figure 7-6) are shown in Figure 7-11. It can be seen that the tip angle on the stud does not substancially influence the quality of the bonding or the size of the HAZ. Only a general influence of the axial pressure could be found in the improved bonding at the bottom of the hole with increased axial pressure. Furthermore, the shape of the frictional plane changes from reasonably flat at low pressures to a more cone shaped surface at higher pressures. The final frictional planes can be seen as lines in the grain structure at the upper part of the hole and emerge in the shape of the HAZ in the stud as well.
The welds with chamfered hole bottom and stud tip (Figure 7-7) still showed lack of bonding all around the bottom area of the weld (Figure 7-12). Nevertheless the quality of the weld increases significantly with increasing stud chamfer angle. The macrograph of the weld A with the same shape of the hole and the stud tip shows unfilled areas in the transient to the cylindrical hole. In comparison with A the macrograph of weld C shows complete filling of the cavity and a small HAZ at the bottom chamfer.

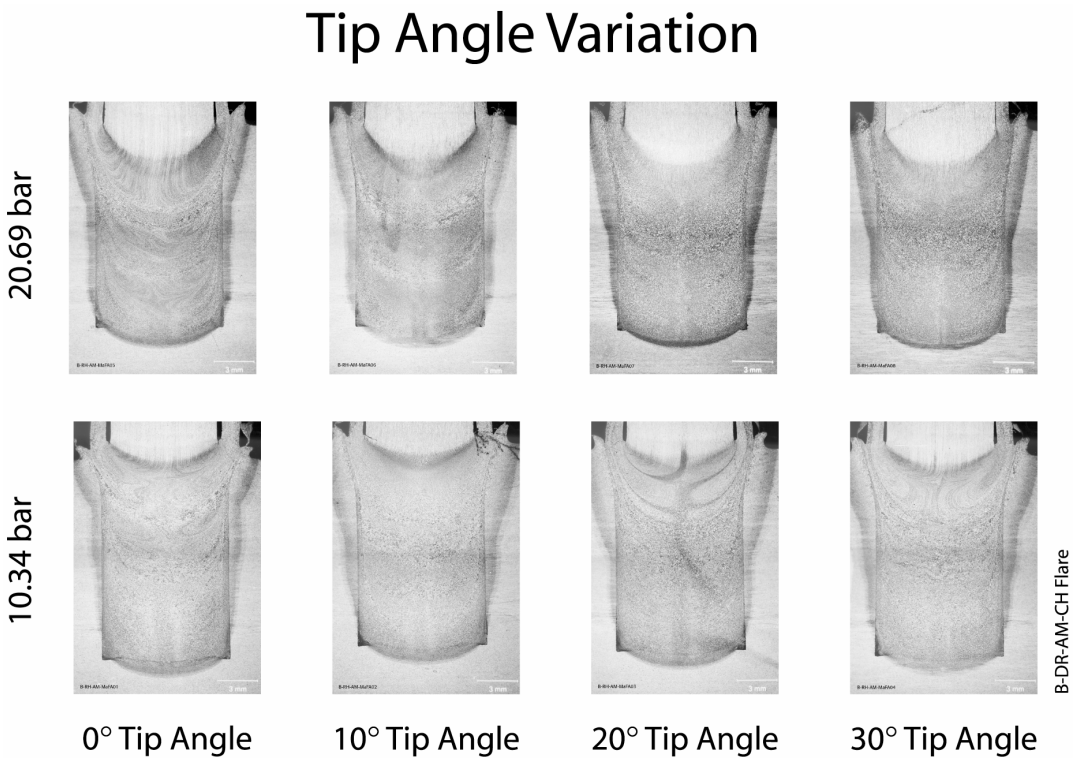

Figure 7-11: Macrographs of weld matrix with different tip angles.

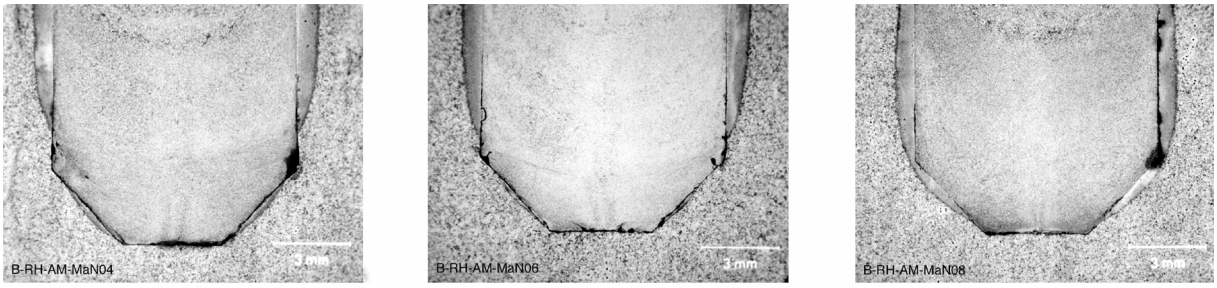

Figure 7-12: Macrographs of welds with chamfered hole and stud design, bottom area only.

The influence of the welding parameters on the material flow was visualised in a 3x3 welding parameter matrix with nickel tracer in the centre of the stud. The macrographs of this matrix are shown in Figure 7-13. Owing to problems during cutting of the specimen the macrograph of weld Fl01 does not show any nickel and the one from weld Fl04 shows cutting marks at the top. The welds produced at low rotational speed (2000 rpm) show the most uniform microstructure with very regular deformation of the nickel rod. Weld Fl04 shows that the very tip of the stud obviously sheared off at the very beginning and stayed undeformed. Higher rotational speeds and higher axial pressures caused a more irregular deformation of the nickel rod and inhomogeneous macrostructure.

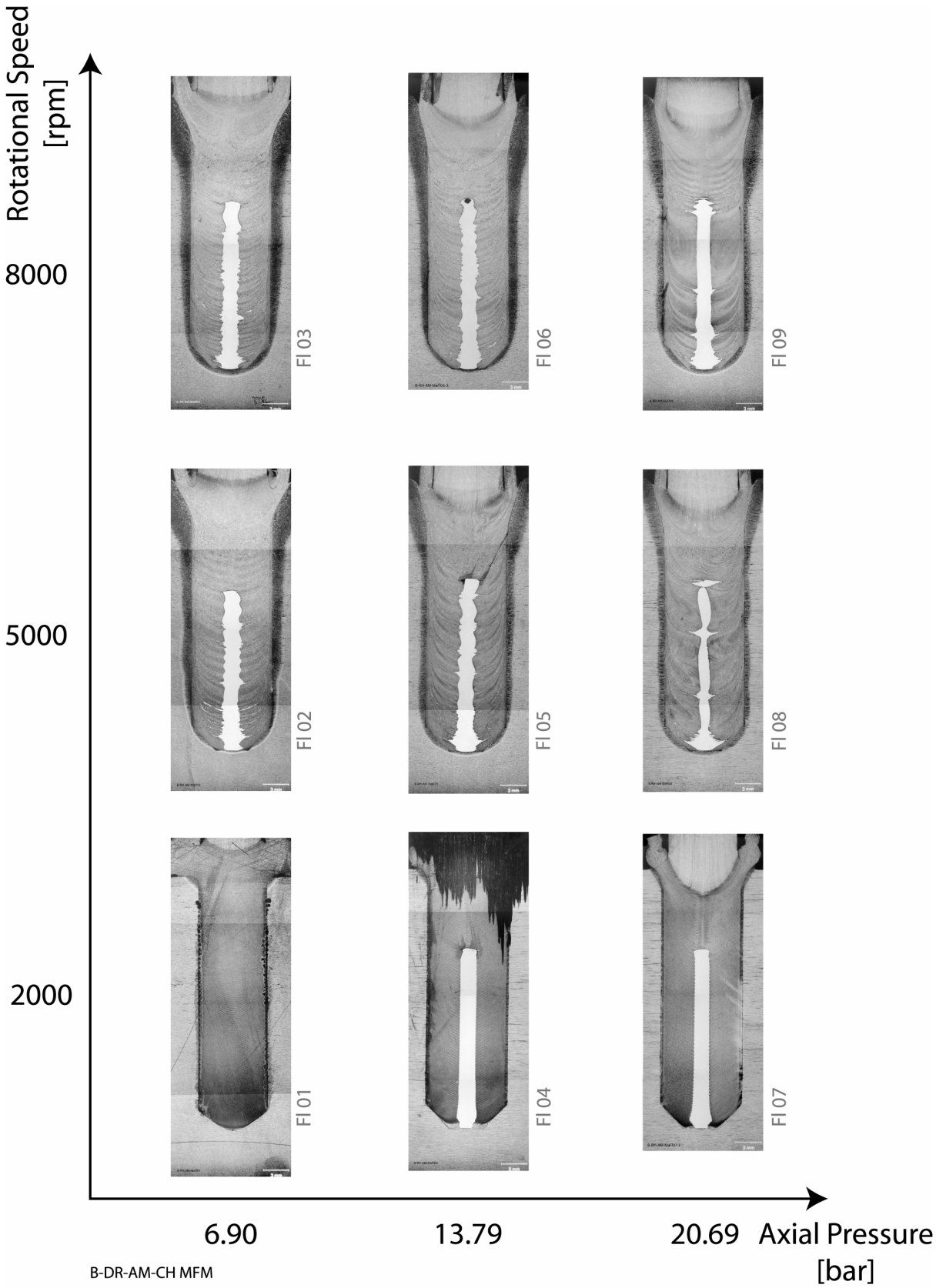

Figure 7-13: Macrographs of the 3x3 welding parameter matrix with nickel tracer studs.

Weld FI09 shows an approximately 6 mm long area in the middle of the hole with almost no HAZ and an un-deformed nickel rod. Shear planes, where non-plasticised stud material shears off the end of the stud, are indicated by a significant horizontal widening of the nickel tracer. At those locations the process “jumps” over a certain stud distance without plasticising the stud material in between and starts again with a new frictional plane on top of this sheared material. It should be emphasised that almost none of the Nickel material from the centre of the welding consumable is transported to the sides of the hole during the weld. Material from the centre of the stud will be predominantly deposited in the centre area of the weld. Figure 7-14 presents the measured welding parameters of weld FI08 (Figure 7-13). As indicated in the diagram two shearing phenomena can be clearly identified in a drop of the rotational speed, followed by an “overshooting” after the lower part of the stud sheared off and almost no torque is required. This correlates with a drop in the axial pressure as well, as the piston has to move suddenly to create the set axial pressure on the new faying surfaces.

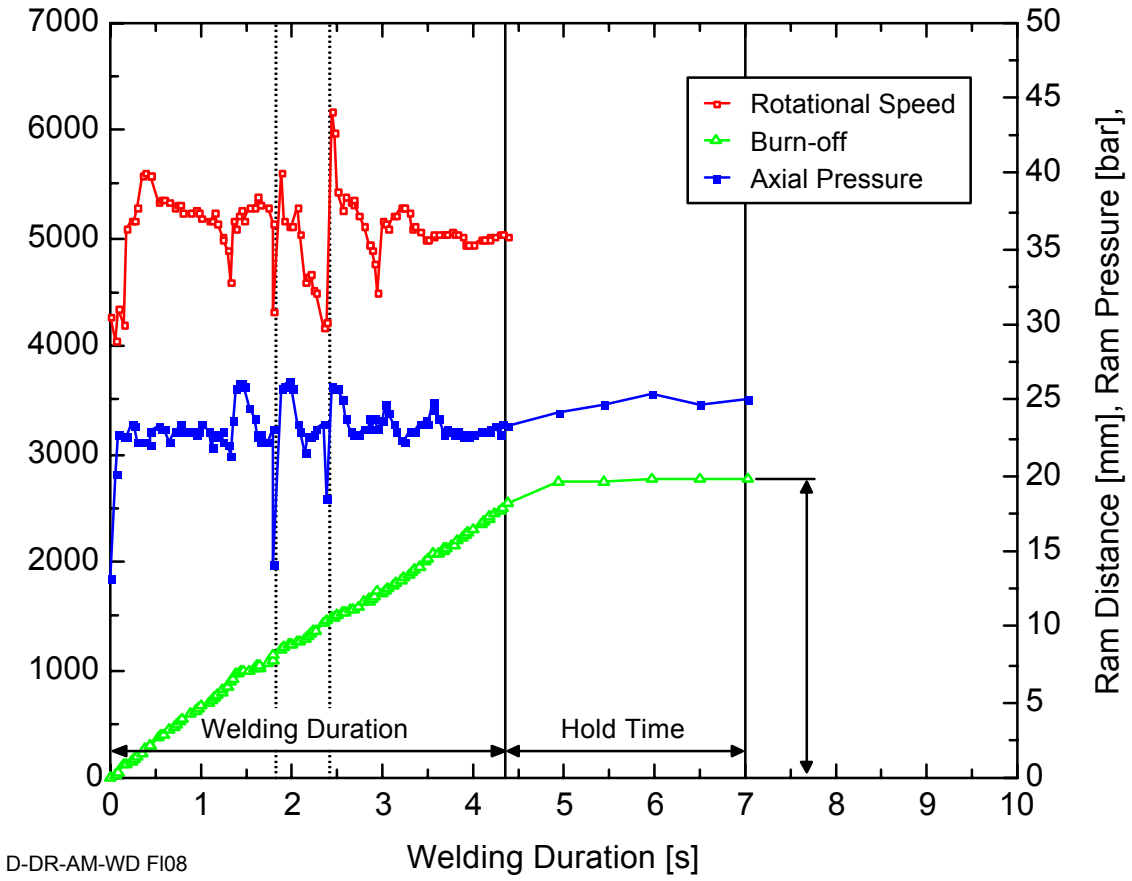

Figure 7-14: Welding parameter measurements of weld FI08, as measured by the DRS. Two shearing phenomena can be clearly identified (indicated by dashed lines).

The development of the plastification during the FHPP weld is shown in Figure 7-15. It is clearly shown how the plastification starts at the tip of the stud while the plasticised material rises in the gap between the stud and the hole. The shape of the frictional plane immediately

changes to an almost hemispherical contour. A number of shear planes developed as a result of the process parameters and the material properties.

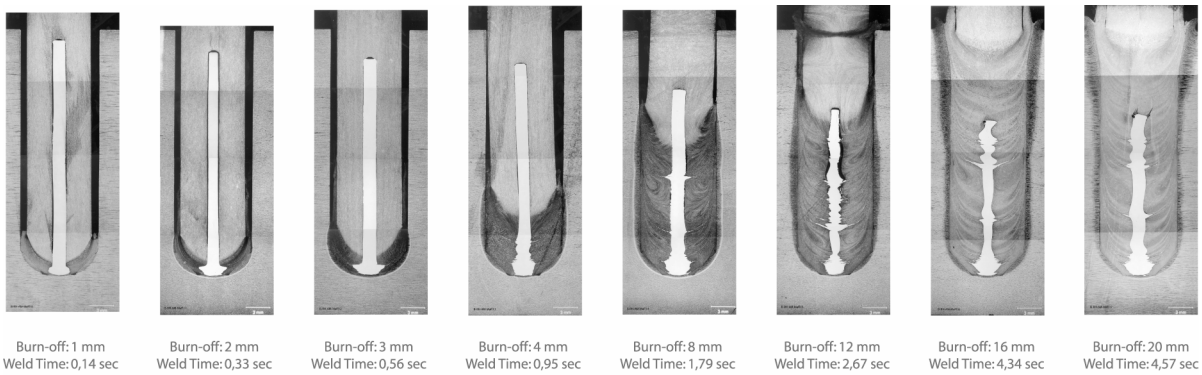

Figure 7-15: Development of plastification during FHPP demonstrated by welds with nickel tracer studs.

Based on the results of the experiments described above the design of the bottom of the hole was changed to improve the material transport as well as the overall bonding properties. The design of the stud retained 45° chamfer at the tip. As shown in Figure 7-16 this resulted in a significantly improved quality of the weld although still some lack of bonding can be seen at the rounded transient. Afterwards the stud diameter was increased to 10 mm and the hole size to 12 mm diameter. The macrograph with a 10 mm diameter stud and comparable welding parameters to the one shown in Figure 7-16 is shown in Figure 7-17. This figure clearly shows a increased HAZ all around the bonding line and improved bonding at the rounded transient.

Figure 7-16: Macrograph of a weld in X65 with 8 mm stud diameter and rounded transition at the bottom of the hole.

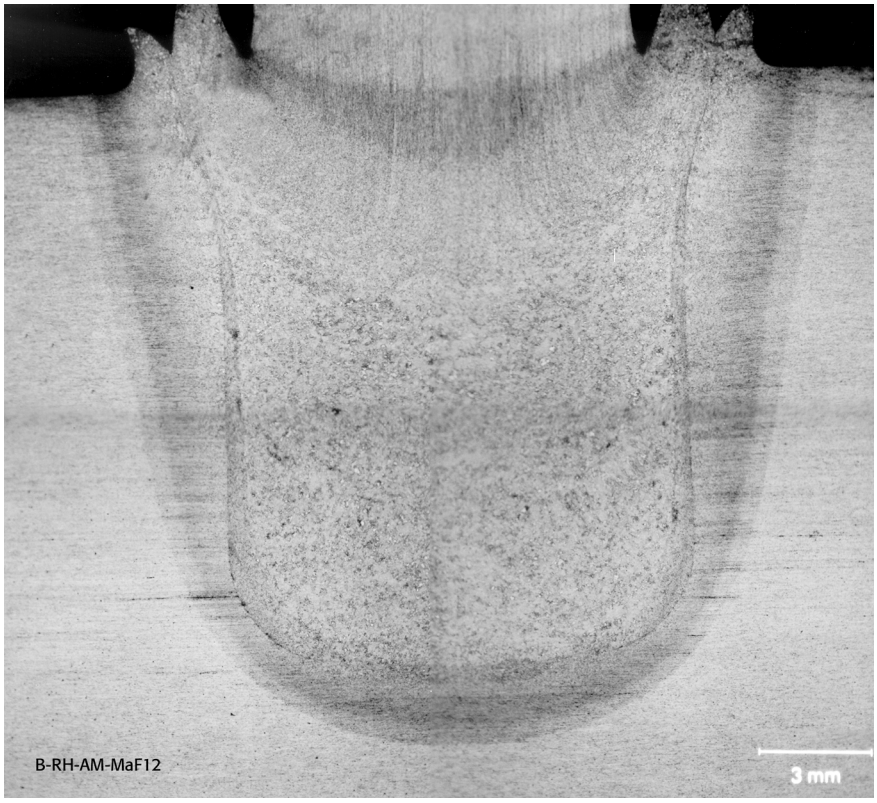

Figure 7-17: Macrograph of a weld in X65 with 10 mm stud diameter and rounded transition at the bottom of the hole.

Further investigations with this shape of the hole were performed with 10 mm diameter studs and different hole diameters (10.5, 11, 12 and 13 mm). The size of the HAZ increases with increasing hole diameter due to the bigger gap volume which is filled with plasticised material (Figure 7-18). Next to the weld DR02 in the 10.5 mm diameter hole with a bend angle of 170°, specimen TT05 in the 12 mm diameter hole showed a bend angle of 158°. Based on the bending test results, the uniform HAZ and the overall system performance during the welds, the combination of 10 mm diameter studs and 12mm diameter holes with the rounded transient at the bottom was selected for further welding experiments. The optimum welding parameter set for this geometry combination was established in a 4x3 welding parameter matrix. An optimum welding parameter window was found as shown in Figure 7-19. The defect free macrograph of weld specimen F06 welded with 6000 rpm and 20.69 bar is shown in Figure 7-20 together with the appropriate hardness survey. It can be seen that the hardness values rise from about 200 $HV_{0.2}$ in the base material to about 300 $HV_{0.2}$ in the HAZ. The hardness in the weld material itself varies between 250 and 340 $HV_{0.2}$. The horizontal pass at 2 mm distance from the plate surface depicts the un-affected stud material at the top of the weld, as this pass is above the final frictional plane.

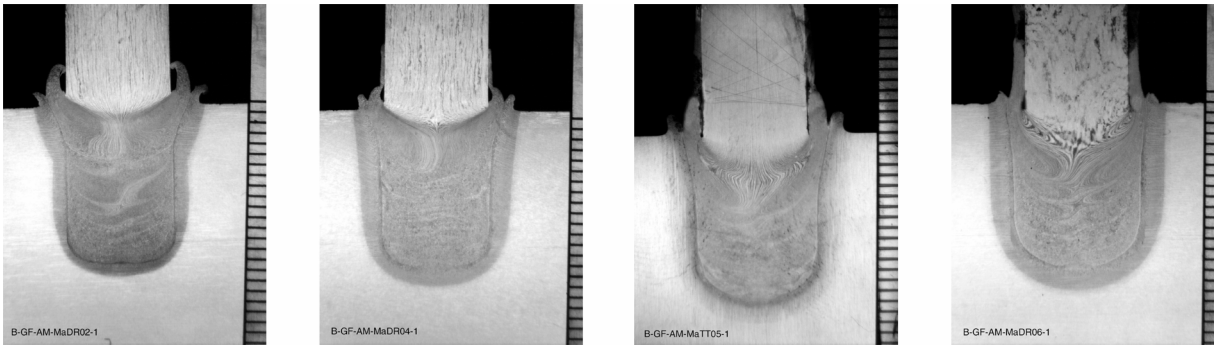

Figure 7-18: Macrographs of 10mm diameter studs in holes with 10.5, 11, 12 and 13 mm diameter.

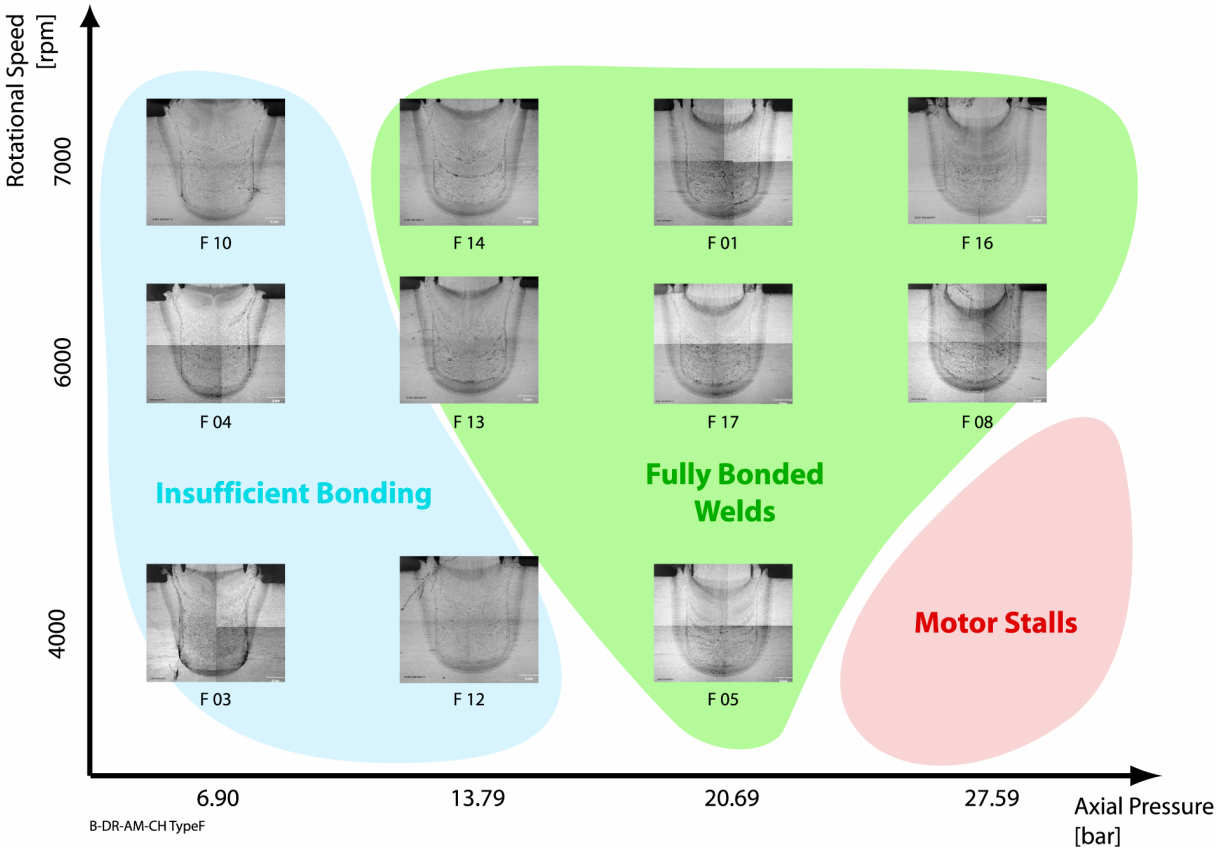

Figure 7-19: Welding parameter matrix for 10 mm diameter studs and 12 mm diameter holes in X65.

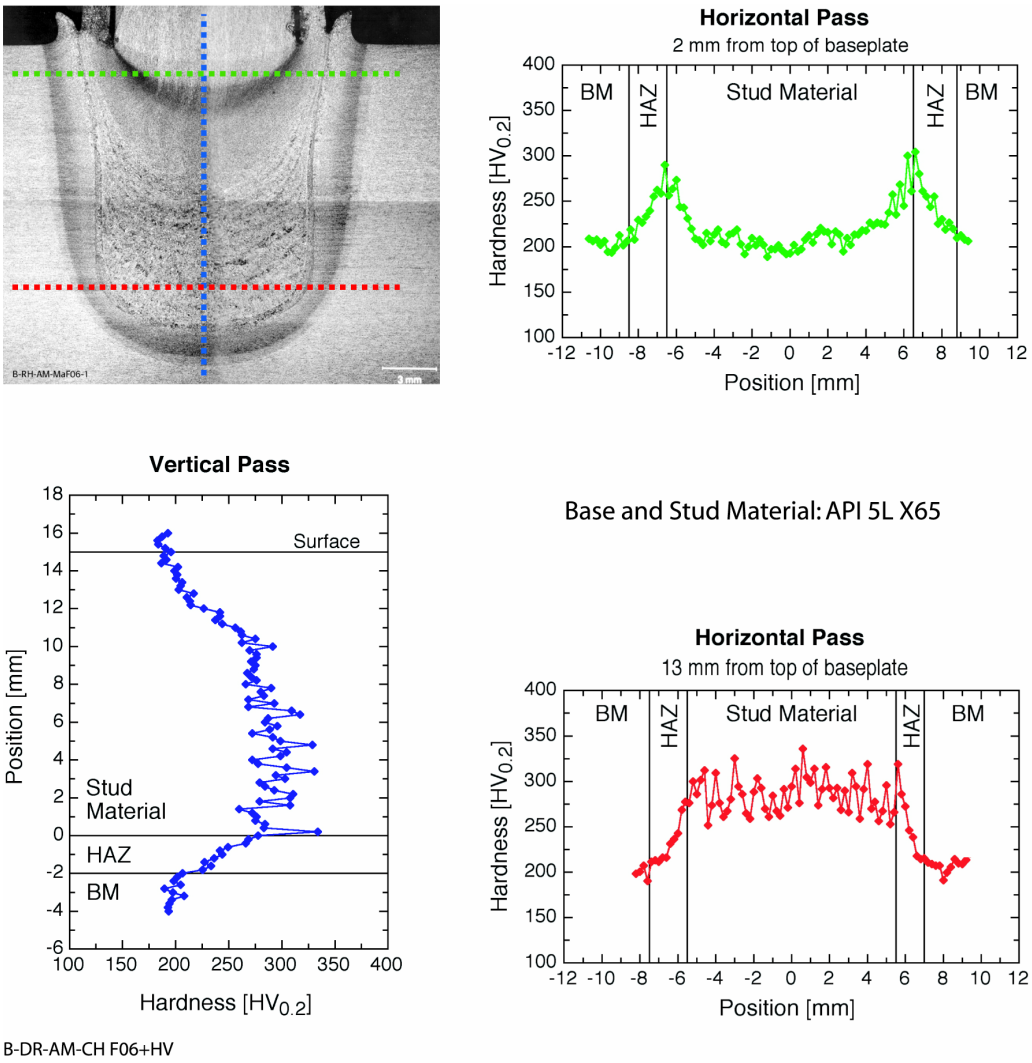

Figure 7-20: Macrograph and hardness survey of a defect free FHPP weld in X65.

Besides these experiments with cylindrical holes and API 5L X65 material (material 01), further experiments with DIN S235 mild steel and tapered hole and stud geometries have been performed (material 04 and 05). The results of a 3x6 welding parameter matrix are shown in Figure 7-21. Welds with high axial pressures resulted in stalling of the weld head motor during the weld, while low axial pressures gave insufficient bonding at the bottom of the weld. Figure 7-22 shows the macrograph and hardness survey of specimen TS20, welded with 7000 rpm and 27.59 bar. The hardness surveys show generally the same behaviour as presented for the cylindrical welds, while the values rise from about 160 $HV_{0.2}$ in the base material to about 250 $HV_{0.2}$ in the HAZ and the weld material. Contrary to expectations an expansion of the parameter window for sound welds to lower axial pressures could not be observed. The optimised welding parameters are shown in Table 7-1. While classifying tapered welds for comparison with cylindrical welds only the first line of welding parameters is used further on.

Table 7-1: Optimised welding parameters for tapered welds in DIN S235.

Axial Pressure [bar]	Burn-off [mm]	Rotational Speed [rpm]
27.59	2	7000
27.59	3	5000
27.59	Hold for 3 sec.	-

A number of additional welds with optimised welding parameter sets have been produced for bend tests and Charpy impact tests (see chapter 6.5). Charpy specimen were tested at –20 °C with the notch in the bonding line on one side of the hole. The results are presented in Table 7-2.

Table 7-2: Results of bend and Charpy impact tests with tapered welds in S235.

	No. of specimen	Mean Value	Lowest Value
Bend Test	7	158°	115°
Charpy Impact	4	107 J	90 J

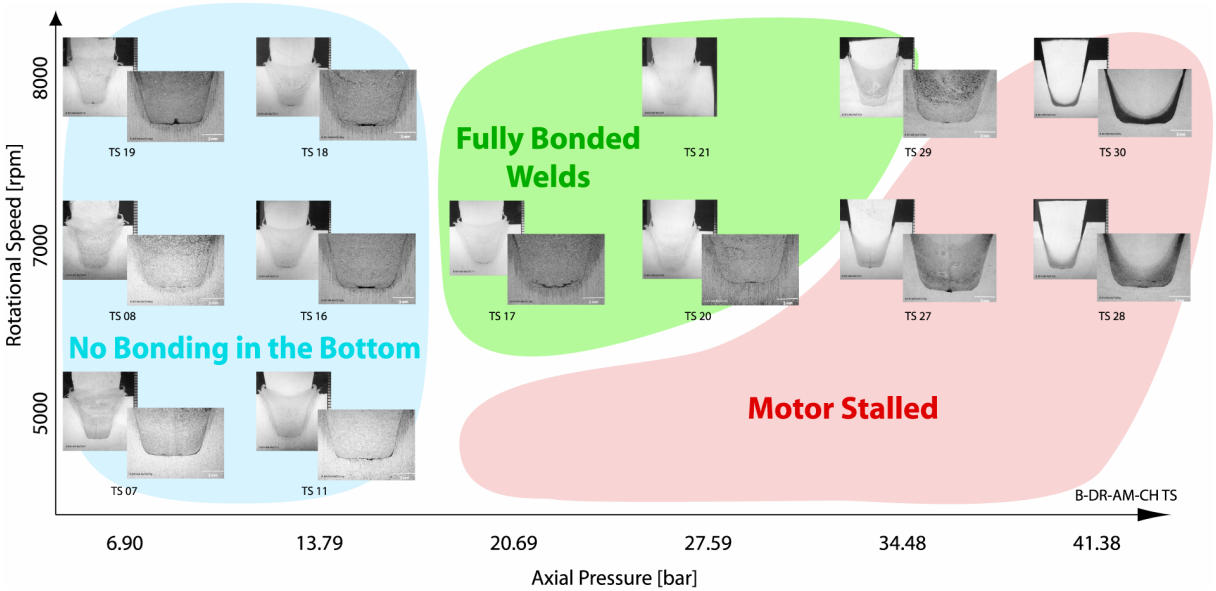

Figure 7-21: Welding parameter matrix for S235 tapered stud welds with macrographs of the complete weld and details of the bottom area.

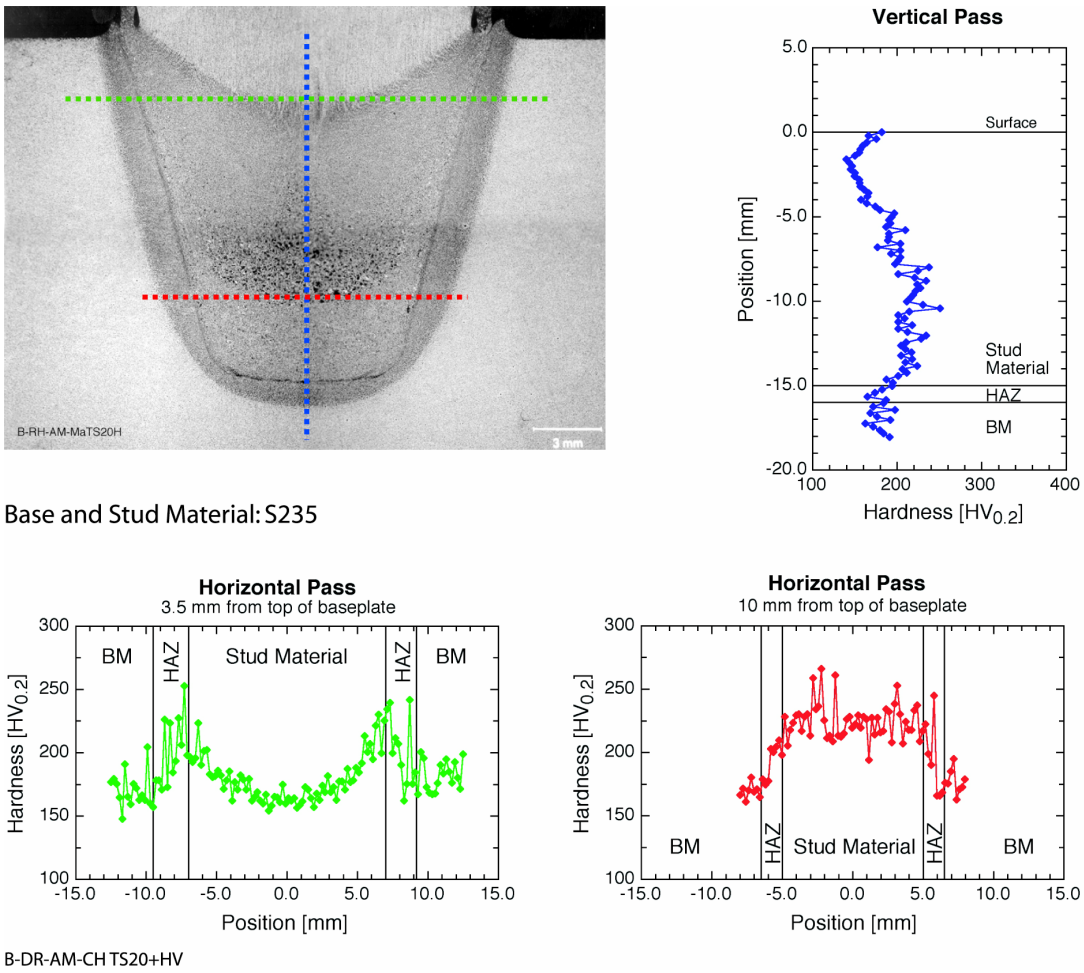

Figure 7-22: Macrograph and hardness survey of specimen TS20.

7.3 THERMAL PHENOMENA

A first approach to evaluate the temperature cycle in FHPP welds was performed with 5 thermocouples along the bonding interface. The main objective of these measurements was to establish the influence of the welding parameters and geometry combinations on the temperature cycle in the HAZ. The moving frictional plane has to be considered as the heat source in FHPP. This complicates the exact evaluation of the distance between the heat source and the thermocouples. It will be considered in the following that the distance between the thermocouple and the bonding line can be seen as the distance to the heat source as well. Some of the results gained will be used to describe the conditions at the bonding interface of welded specimens which will be analysed in more detail in chapter 7.4. It should be emphasised that with this experimental set-up only the temperatures within the HAZ to the sides of the holes were measured. In order to estimate temperatures at the frictional interface a number of thermocouples in different distances to the heat source and the exact distance to this source would be required. Such an extended measurement programme was not within the scope of the presented first temperature evaluation.

7.3.1 EXPERIMENTAL PROCEDURE

The influences of the stud and hole geometry combinations were evaluated with welding specimens in five different geometries (Types A to E). Starting from a cylindrical hole and stud combination (Type A) the taper angle of stud and hole was increased up to a 30° taper angle of the hole (Type E, see Figure 7-23) The cylindrical holes would be the best choice for very deep holes and would give the best efficiency with stitch welding (amount of weld material to the length of the weld). Tapered holes usually give a wider welding parameter tolerance and benefits in thin-walled structures. Studs were machined from base material 02, while the plates were made of base material 03 (see chapters 6.1.2 and 6.1.3).

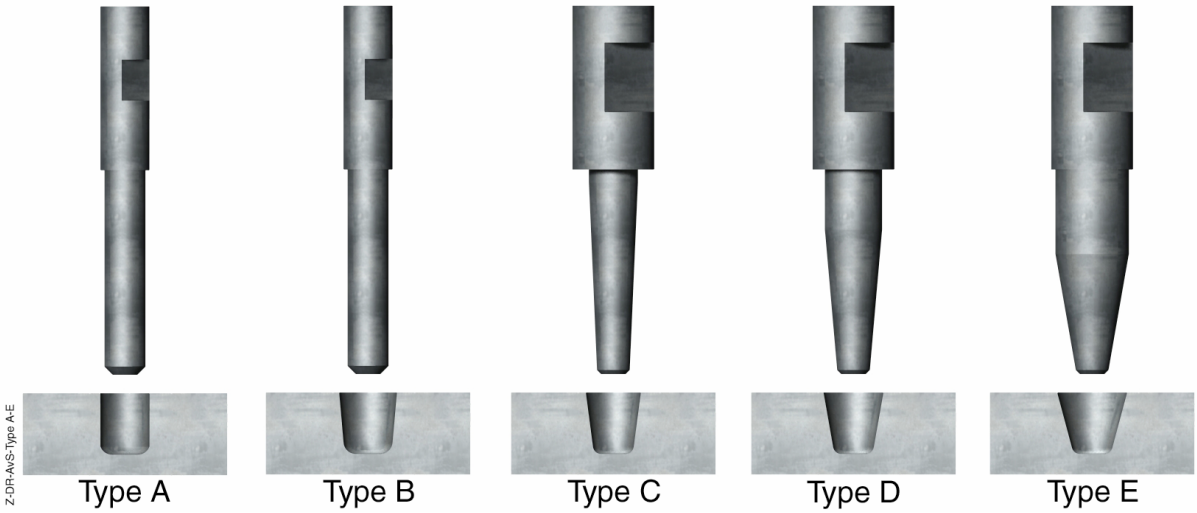

Figure 7-23: Type A to Type E stud and hole geometry combinations used within this study

The type A geometry (cylindrical) was used to determine the welding parameter influence as well. Four different axial pressures and three different rotational speeds were welded with this geometry, while only one parameter combination was used for all the other geometries.

Five holes (0.8 mm diameter) were spark eroded in the base plates with 0.5 mm distance to the borehole at different distances to the plate surface (see Figure 7-24). Type K thermocouples with 0.5 mm diameter were then placed in these holes with conductive paste and connected to the thermocouple measuring system (described in chapter 6.4.2). The temperature values during the welds were recorded at 50Hz and saved for further analysis. The $\Delta t_{8\text{-}5}$ time was calculated from the measured data after the welds.

Figure 7-24: Position of thermo-couple-holes in a type A and a type E base plate.

Every welded specimen was sectioned and polished for further analysis with the optical microscope and hardness tests. The distance between the tip of the thermocouple holes and the bonding line was measured with a digital image system on an optical microscope.

7.3.2 RESULTS

It has been observed that owing to the difficult procedure during the spark erosion of the thermocouple holes the actual distance between the tip of the holes and the bonding line varied significantly. Distances of 653 to 2091 µm were measured on the cross sections, although a distance of 500 µm was specified. In particular, in such close distances to the heat source these variations complicate the analysis and direct comparison of results. Hence, the measurements presented should only be considered for trends and not for absolute thermal analysis.

Figure 7-25 shows the measurements of two welds (type A, cylindrical geometry) with different axial pressures (27.59 and 13.79 bar) and same rotational speed (6000 rpm). The graphs show the temperature records for 30 seconds, while the maximum temperature was reached at the end of the welds for all records. The distance between the thermocouple hole and the bonding line (as measured after the weld) is given for each thermocouple. The bottom thermocouple (N°5) showed rising temperatures first, while later response of the rest of the thermocouples showed the gradually filling of the holes.

The measurements for all geometries and all welding parameters showed that the maximum temperature in the middle of the weld (N°3) is almost 200 °C higher than near to the surface (N°1+N°2). In most of the records the maximum temperature at position N°5 (bottom) is similar to the ones at positions N°1 and N°2.

The influence of the axial pressure on the temperature cycle is shown in Figure 7-25 for all five thermocouple-positions. Figure 7-26 shows the influence of the axial pressure as well as the rotational speed on the temperature cycle exemplary only for position N°3. It should be noted, that the maximum temperature reduces with increasing rotational speed, while the axial pressure mainly influences the slope of the temperature profile. Higher axial pressures result in a faster weld and a steeper temperature cycle.

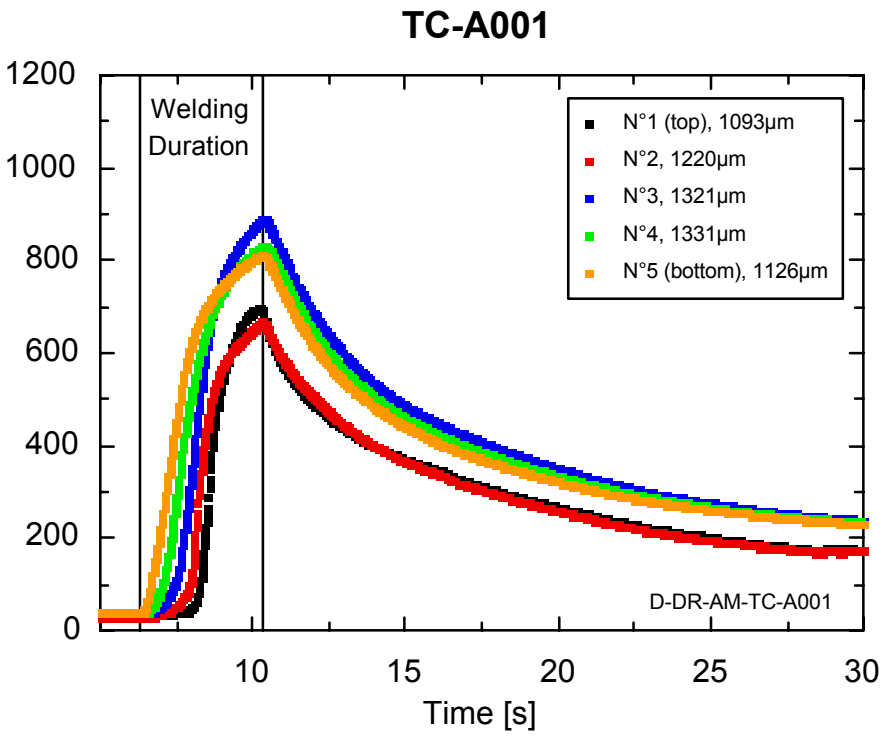

Axial Pressure:

27.59bar

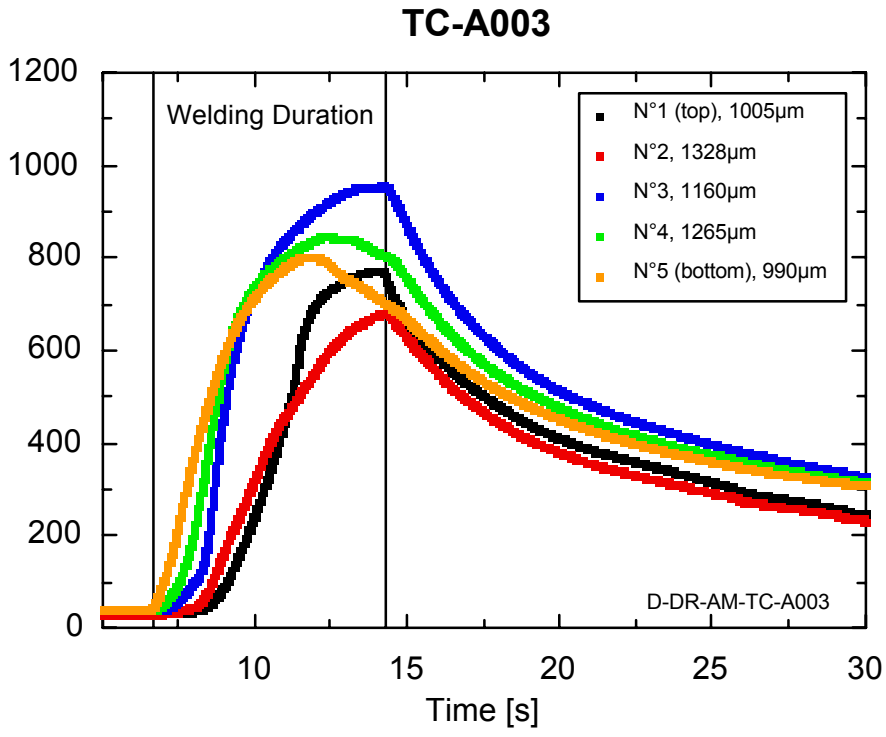

Axial Pressure:

13.79bar

Figure 7-25: Temperature measurements of specimen TC-A001 (27.59 bar) and TC-A003 (13.79 bar) at different distances to the plate surface. The distance between the thermocouple hole and the bonding line is given, respectively, in the legends.

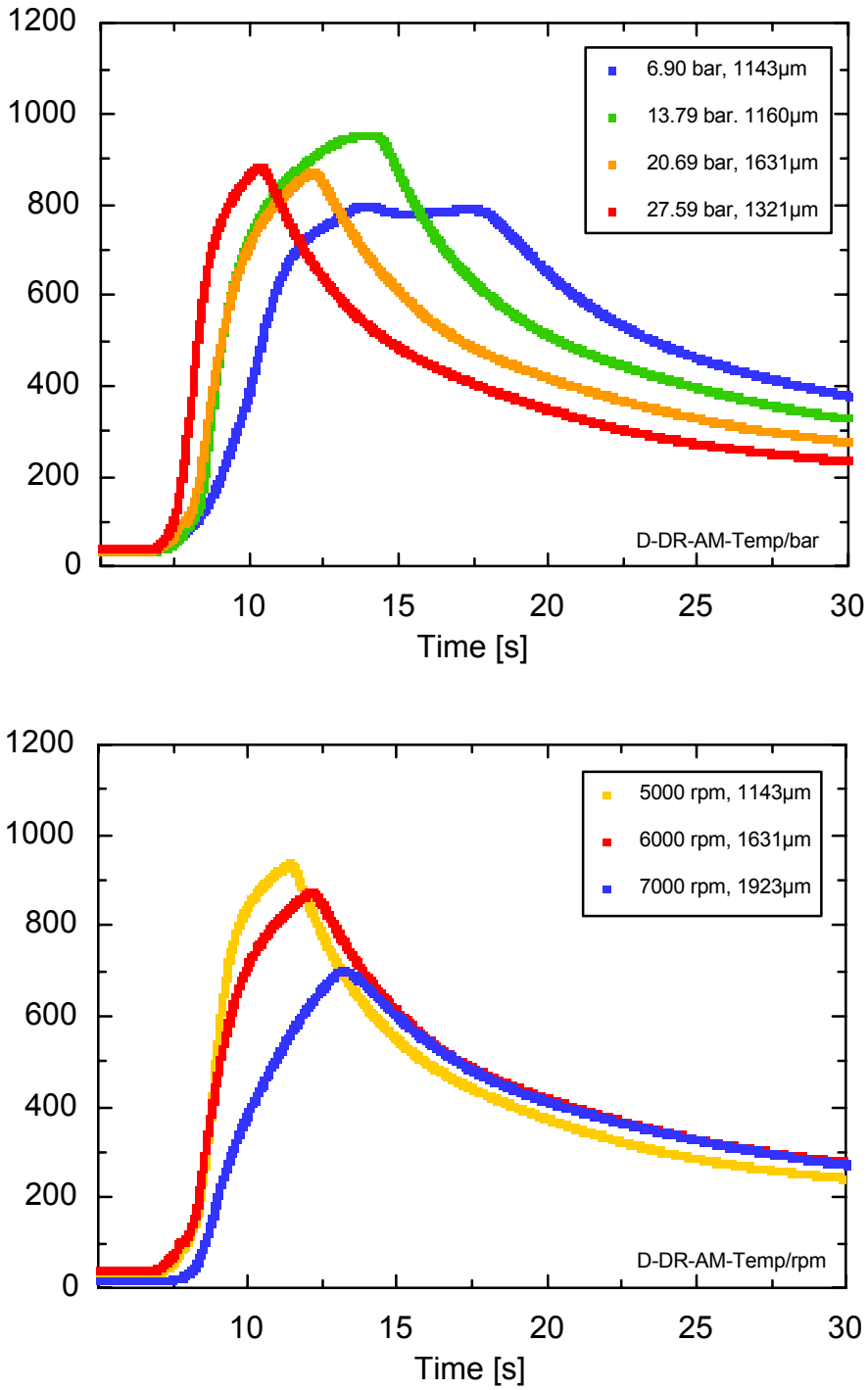

Figure 7-26: Influence of the axial pressure and the rotational speed on the temperature cycle measured at position N°3. The respective distances between the thermocouple holes and the bonding line is given in the legends.

Figure 7-27 shows the temperature measurements for the tapered geometry weld TC-E002. Compared to the temperature measurements for cylindrical welds as presented in Figure 7-25, the maximum temperatures are approximately 300 °C higher. The high temperatures and the long welding duration result from the bigger cross section area of the stud. The measurements for thermocouple N°1 (top) are affected by plastic deformation of the upper

hole area associated with the tapered geometry. Hence the proper placement during the welding cannot be guaranteed.

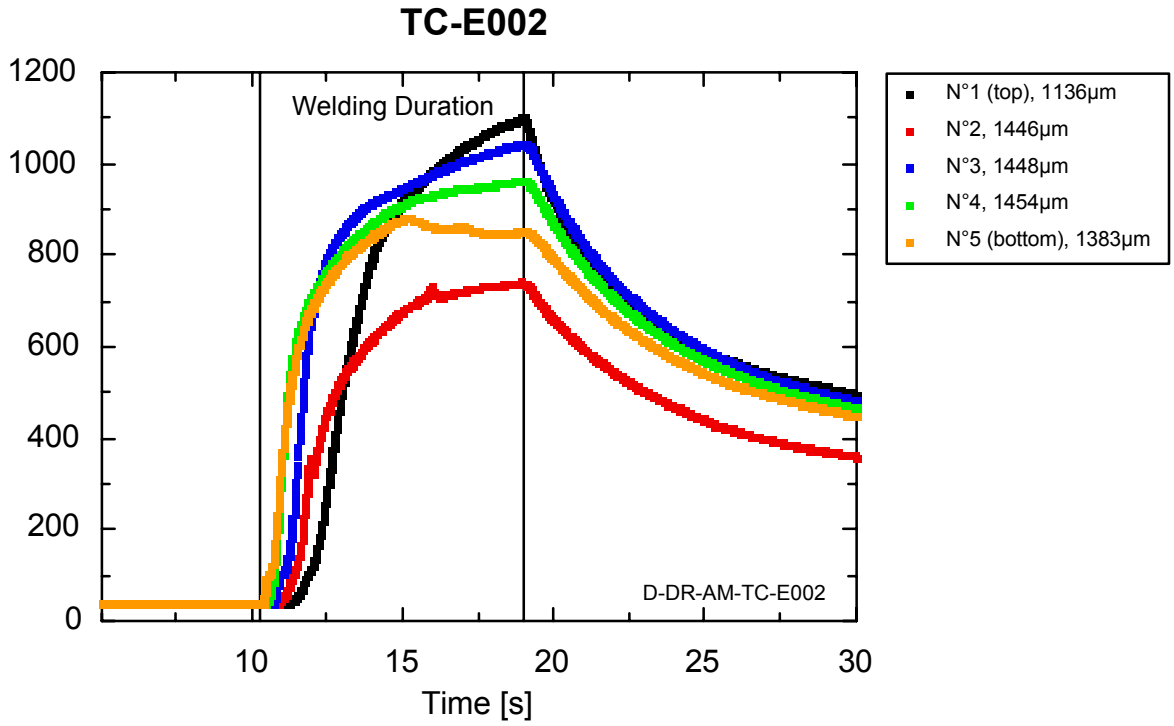

Figure 7-27: Temperature measurements for tapered specimen TC-E002 with the distances between the thermocouple holes and the bonding line given in the legend.

7.4 Bonding Mechanism

The main objective of this chapter is to evaluate the influence of the main welding parameters and geometry combinations on the mechanical properties of FHPP welds. This will be done globally for a complete weld as well as locally for different regions of the weld. Finally a proposed bonding mechanism for FHPP welds is presented.

7.4.1 Experimental Procedure

The same five geometry combinations (Type A to Type E) already presented in chapter 7.3.1 (Figure 7-23) for the temperature measurements, were used for these experiments to assess the geometry influence. The material combination was base material 02 for the studs and base material 03 for the plates (see chapter 6.1.2 and 6.1.3). In order to establish the best welding parameter combination a matrix of five different sets was welded for each geometry. The welded samples were visually inspected as described in chapter 6.5.2 and bend tests were performed from each specimen according to chapter 6.5.4. The optimum welding parameters were chosen based on the results of the bend tests and the macrographic examination. More specimens were subsequently welded with optimised welding parameters for hardness measurements ($HV_{0.2}$), Charpy impact toughness and round tensile tests for global mechanical properties. Micro flat tensile tests taken horizontally across the welds and vertically along the bonding line were performed in order to establish the local mechanical

properties in different weldment regions. The procedures used for all these tests have been described in chapter 6.5.
The total energy and the energy input rate (total energy/welding time) were calculated for every weld within the experiments described in this chapter. It should be emphasised, that due to the assumptions required for the calculations, the energy values are not absolute, but should rather be used for comparison among the welds presented. Calibration of torque measurements would give the exact value for the mechanical-hydraulic efficiency η_{mh} which would include all the specific components of the system (i.e. valves, length and size of hoses). Unfortunately, calibration of the weld head torque was not feasible within the scope of this study. The efficiency for the transfer of mechanical energy in thermal energy can be assumed as 1.0 according to Neumann and Schober [81].

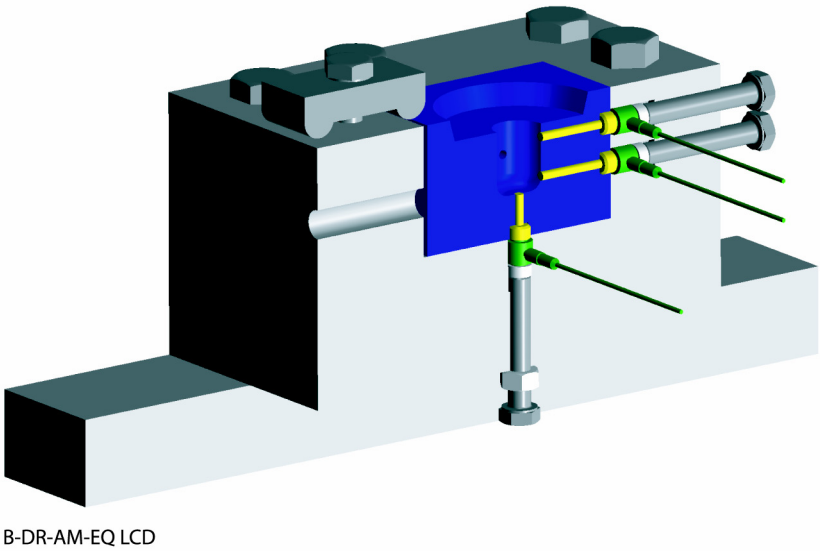

Figure 7-28: Cross section of the load cell device with load cells (green), weld specimen (blue) and pistons in the weld specimen (yellow).

After the temperature cycles and the local mechanical properties have been measured, only the local forces on the bonding line were missing in order to describe the local parameters responsible for the bonding and the corresponding mechanical results. A device was designed and built to accommodate four miniature piezo-electric load cells around exchangeable weld specimens (see Figure 7-28). Special weld specimens were machined from base material 07 (see chapter 6.1.7) with four pistons inside to transfer the load on the bonding line (and the piston's area) to the appropriate load cell during the weld. As shown in Figure 7-28 one of the pistons was located in the bottom of the hole, while the three remaining ones were positioned in different depths in the wall of the hole. The same distances as for the hardness, tensile and Charpy tests were used to locate these pistons. The load cells were part of the Load Cell System as described in chapter 6.4.3.
In order to correlate the force measurements to the current conditions inside the weld, a sequence of welds were produced with increasing burn-off from 1 mm by steps of 1 mm to

the full burn-off for such welds. Macrographs were taken from the cross sections showing the development of the weld formation with the burn-off distance.
Welds were produced with Type A and Type E geometries to analyse the welding parameter influence as well as the geometry influence on the force measurements. The same welding parameter matrices as for the initial parameter optimisation were used. Assuming the process theory of hydrostatic pressure, as presented by Thomas and Nicholas [121] the measured forces should be constant along the hole depth for a given geometry. For the same welding pressure the measured forces should reduce with increasing stud diameter, as the applied load is divided by a larger surface.

7.4.2 RESULTS

The macrographs of all welds for every welding parameter and in all geometry combinations showed defect-free joints all along the bonding lines. Macrographs of the optimised parameter combinations for all geometries are shown in Figure 7-29 to Figure 7-33 along with the respective hardness profiles and bend test results. The optimised welding parameters for the five geometry combinations are listed in Table 7-3 below.

Table 7-3: Optimised welding parameters for the examined geometry combinations in API 5L X65.

Geometry Type A		
Axial Pressure [bar]	Burn-off [mm]	Rotational Speed [rpm]
27.59	12	6000
27.59	Hold for 3 sec.	-

Geometry Type B		
Axial Pressure [bar]	Burn-off [mm]	Rotational Speed [rpm]
20.69	14	6000
20.69	Hold for 3 sec.	-

Geometry Type C		
Axial Pressure [bar]	Burn-off [mm]	Rotational Speed [rpm]
20.69	10	7000
20.69	8	6000
20.69	Hold for 3 sec.	-

Geometry Type D		
Axial Pressure [bar]	Burn-off [mm]	Rotational Speed [rpm]
27.59	2	7000
27.59	4	6000
27.59	7	5000
27.59	Hold for 3 sec.	-

Geometry Type E		
Axial Pressure [bar]	Burn-off [mm]	Rotational Speed [rpm]
34.48	2	7000
34.48	2	6000
34.48	6	5000
34.48	Hold for 3 sec.	-

The bending tests show, that if cracking occurs it happens in the bonding line at the transient from the bottom of the hole to the side walls. Only geometry B shows a different behaviour, with cracks being observed on the side wall bonding line. It should be emphasised that geometry D and E showed bend angle of 170° over a wider range of welding parameters than the three other geometries.
The results of the round tensile tests are shown in Table 7-4. The failure always occured in the base material outside the HAZ.

Table 7-4: Results of round tensile test, welds with different geometries.

Weld Geometry (No. of specimens)	Yield Strength [MPa]	Tensile Strength [MPa]	Elongation [%]
Type A (3)	444	541	26
Type B (3)	435	535	32
Type C (3)	441	540	26
Type D (3)	443	542	24
Type E (2)	470	555	17
Base Material 03	470	565	30

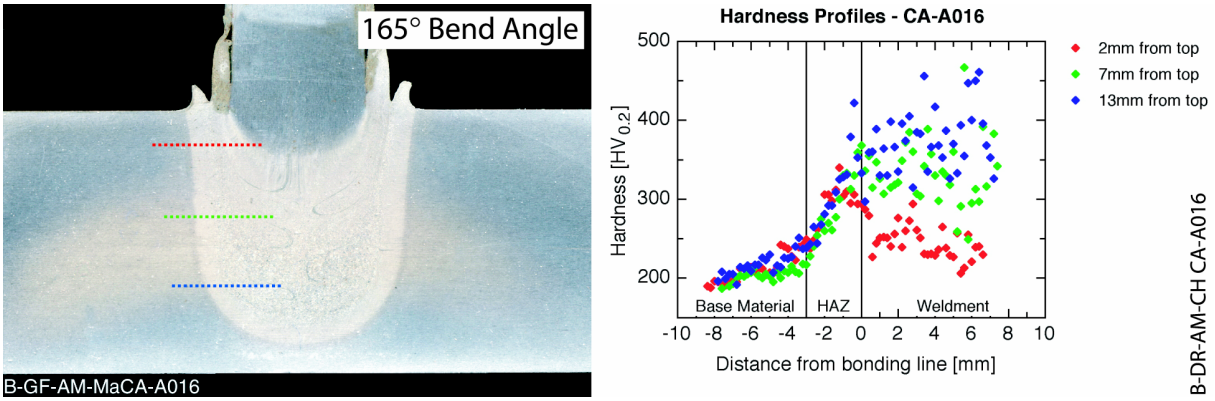

Figure 7-29: Macrograph, hardness measurements and bend test results of geometry type A (CA-A016).

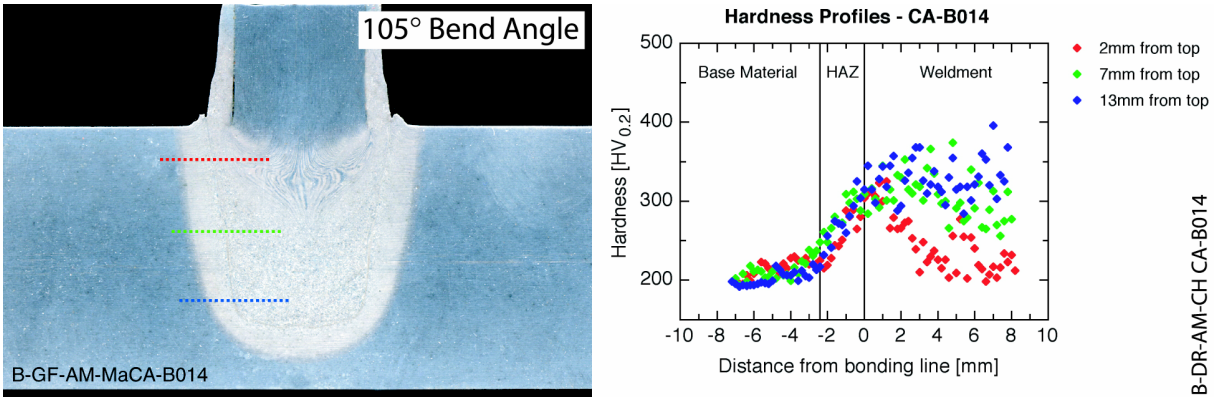

Figure 7-30: Macrograph, hardness measurements and bend test results of geometry type B (CA-B014).

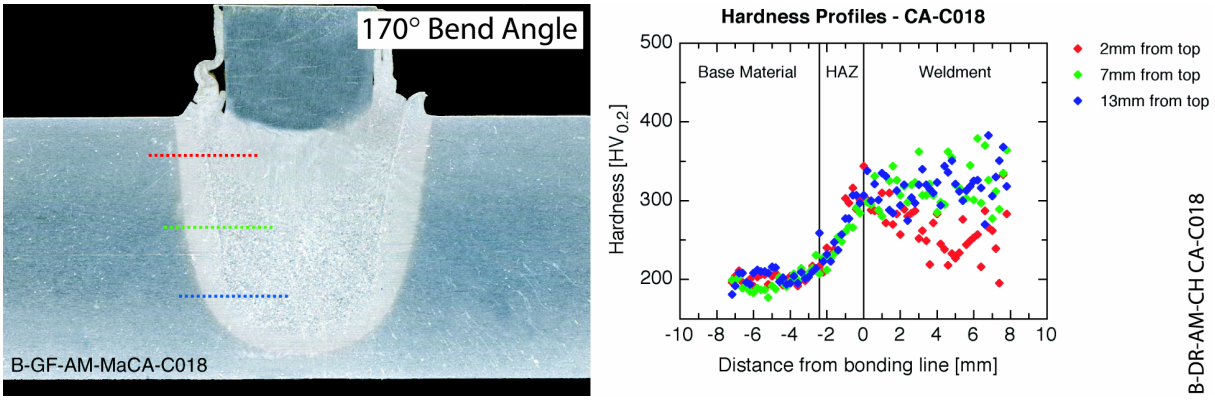

Figure 7-31: Macrograph, hardness measurements and bend test results of geometry type C (CA-C018).

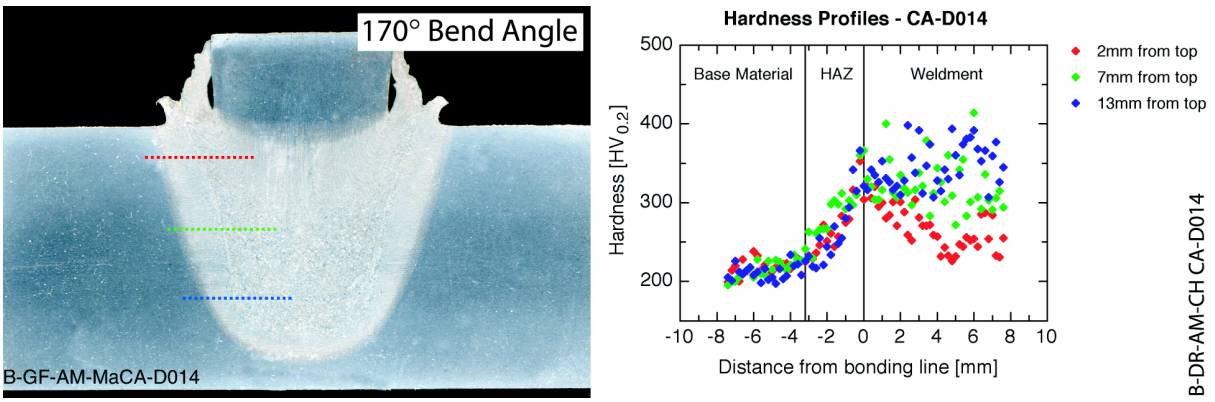

Figure 7-32: Macrograph, hardness measurements and bend test results of geometry type D (CA-D014).

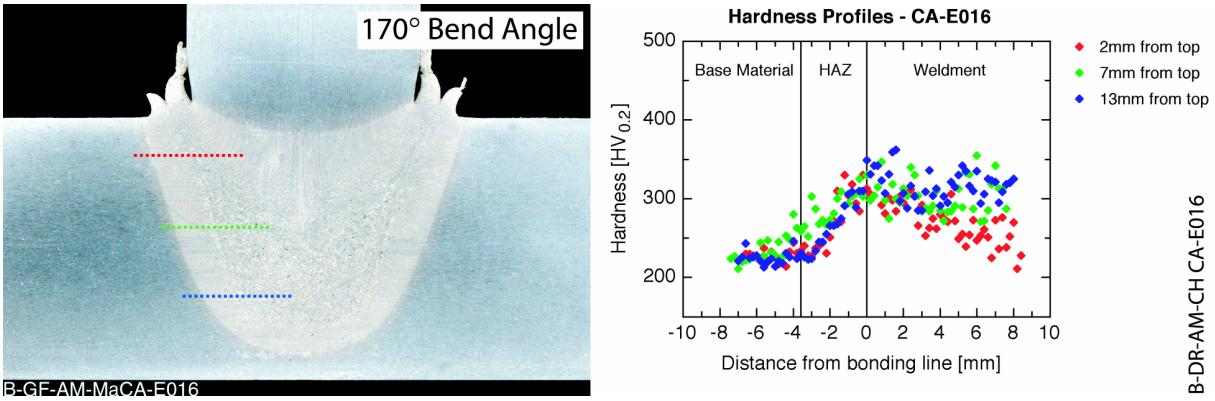

Figure 7-33: Macrograph, hardness measurements and bend test results of geometry type E (CA-E016).

The results of the Charpy impact tests are shown in Figure 7-34. All Charpy tests were performed at -20 °C with the notch at the bonding line. The type C welds show the lowest values with a mean value of 53 J, while type A shows 81 J, the highest measured mean value. Macrographs in the area of the notch of tested Charpy specimens are shown in Figure 7-35.

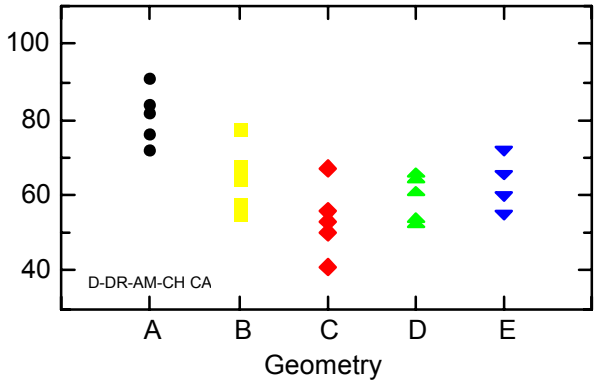

Figure 7-34: Results of Charpy impact tests for different geometries. All tested at -20 °C.

Those macrographs have been taken from the middle of the Charpy specimens and show the side with the weld. Specimens with impact values near to the respective mean values were chosen. The position and size of the notch is indicated in the figures, and it can be seen that the notch was accurately positioned in the bonding line. It should also be noticed that in all but two cases the crack deviated towards the HAZ (base material) where propagation took place, indicating the superior properties of the bonding interface.

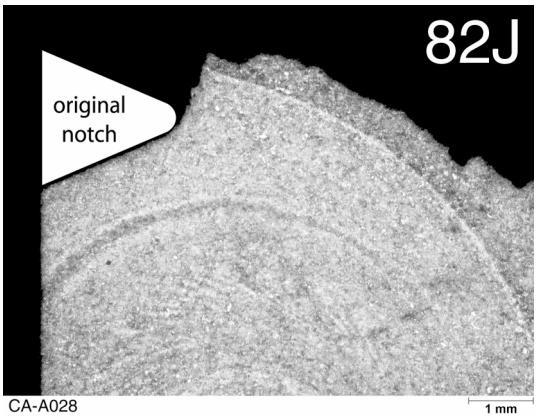

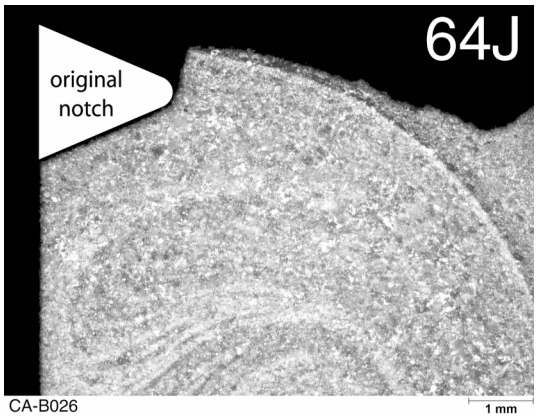

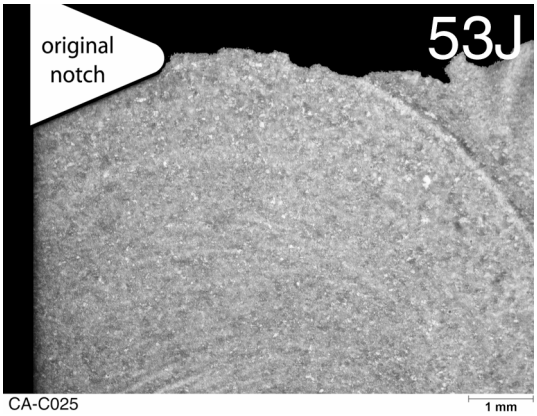

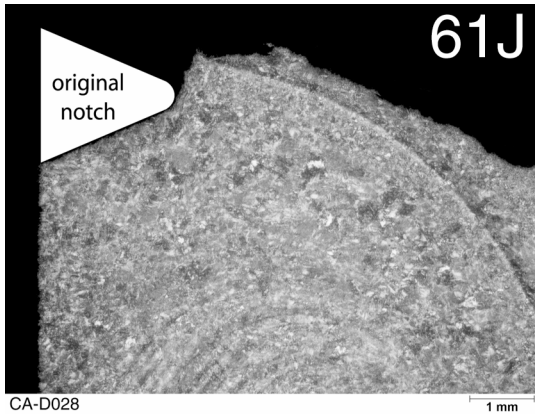

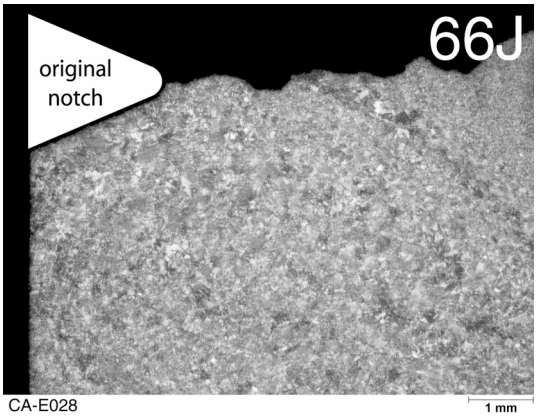

Figure 7-35: Macrographs of tested Charpy specimens in the area of the notch. Original notch size and location illustrated with symbol. Notch location in the bonding line of all specimens with the weld in the lower part of the pictures.

Local mechanical properties across a weld were investigated with micro flat tensile tests and are exemplarily shown in Figure 7-36 for a type E weld (CA-E020). The graph clearly corresponds to the hardness profile and shows an increasing ultimate tensile strength of up to 720 MPa in the stud material. The elongation drops significantly from around 28 % in the base material to around 10 % in the consumable stud. The results of the micro flat tensile tests along the bonding line are exemplarily shown in Figure 7-37 for a type A weld (CA-A021). It can be seen that the values for the ultimate tensile strength and the yield strength do not change with the depth of the weld, only the elongation drops from base material value to around 10 % in the consumable stud. The values show the base material level as given in Figure 7-36. This indicates that the bonding line itself has higher strength than the adjacent base material also indicated by the crack path deviation in Figure 7-35. The plastification during the tensile test concentrates on the softer base material area of the specimen and thus reduces the elongation of the specimen. The results for the other welded specimens display the same behaviour and similar values and will not be shown.

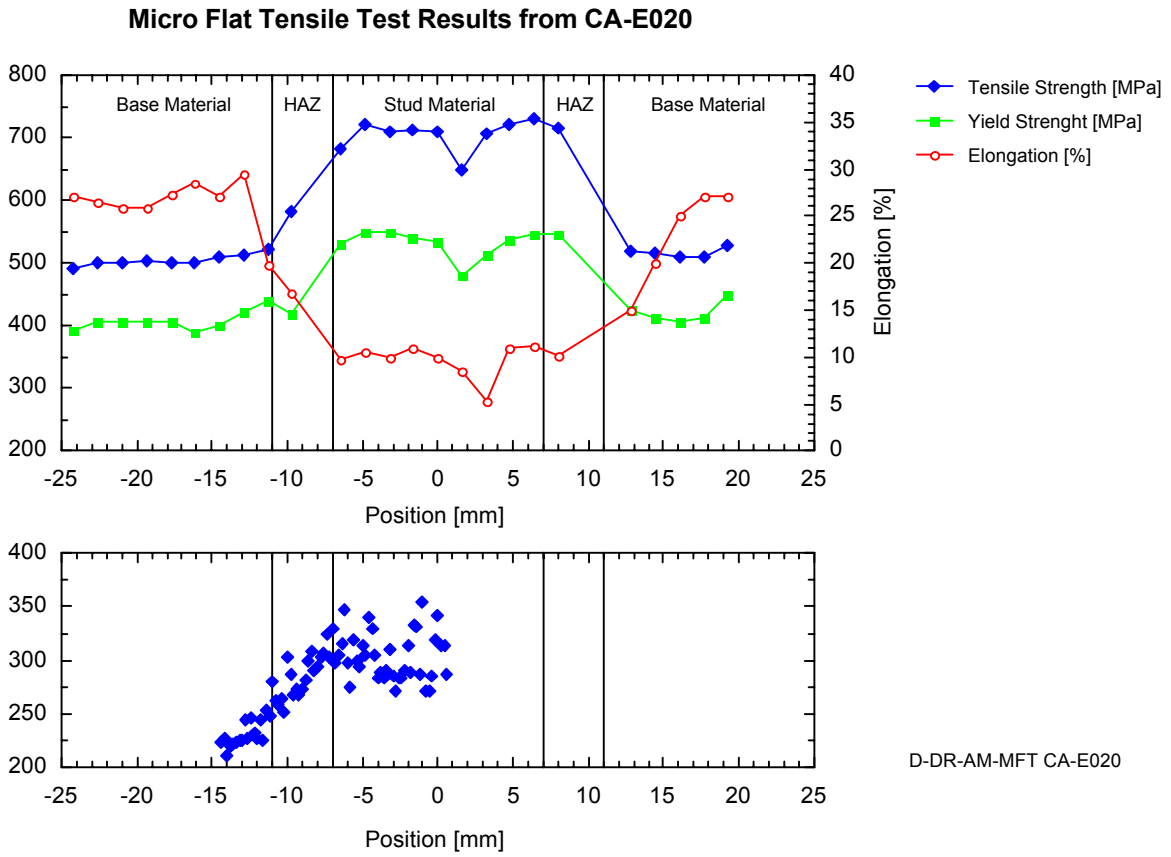

Figure 7-36: Results of micro flat tensile tests and micro hardness measurements across the weld for specimen CA-E020 (Type E).

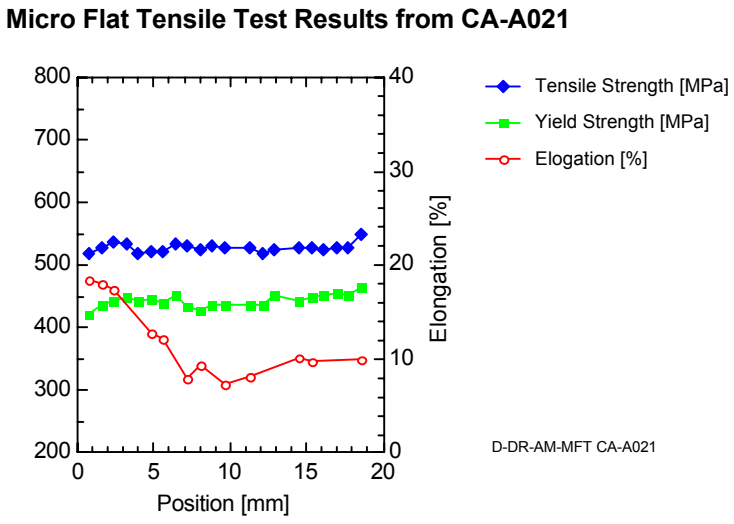

Figure 7-37: Results of micro flat tensile tests along the bonding line for specimen CA-A021 (Type A).

As shown in chapter 6.4.1 the DRS measures the differential pressure at the motor of the weld head. This pressure is directly related to the torque of the motor and thus gives the possibility to calculate energy inputs by the following equations, according to the manufacturers documentation [137]:
An effective differential motor pressure was calculated as

$$\Delta p_{eff} = \Delta p_{Motor} - \Delta p_{idle} \qquad \text{[bar]} \tag{7-1}$$

The differential pressure in the idle run of the motor was measured before for different rotational speeds to establish a value for the internal losses in the weld head and the hydraulic system. Any differential pressure measured above these values was considered to be used for the weld itself.
The actual power can be calculated as

$$P = \frac{T_K \cdot \eta_{mh} \cdot \Delta p_{eff} \cdot n}{9549} \qquad \text{[kW]} \tag{7-2}$$

with $T_K = 0.25$ – Torque constant [137]
$\eta_{mh} = 0.8$ – Estimated mechanic-hydraulic efficiency [137]
n – Rotational speed

The total kinetic energy used for a weld can then be evaluated as

$$E_{rot} = \int dt \cdot P \qquad \text{[kJ]} \tag{7-3}$$

The energy produced by the axial pressure and the corresponding forging is given by

$$E_{forge} = F_{axial} \cdot burn\text{-}off \qquad \text{[kJ]} \tag{7-4}$$

Even for a high pressure weld (30 kN) with large burn-off distance (12 mm) the energy calculates as follows

$$\begin{aligned} E_{forge} &= 30kN \cdot 0.012m \\ &= 0.36kJ \end{aligned} \tag{7-5}$$

It will be shown that this value is 0.5 % of the energy produced by the rotational speed, within the parameter envelope investigated. Hence only the energy produced by the rotational speed was calculated and used as the total energy input for the appropriate welds. Neumann and Schober [81] showed as well, that less than 1 % of the total energy input is caused by

the axial shortening and that in friction welding nearly 100 % of the energy input is transferred to heat inside the weld.
The different energy rates for welds of type A and type E with different welding parameters are shown in Figure 7-38. It can be seen that the heat generation per time is very similar for the different geometries. It is mainly dependent on the rotational speed and the axial pressure. Nevertheless the total energy produced is generally higher for type E due to the bigger diameter and the longer welding duration. The energy input rate rises with increasing axial pressure and falls with increasing rotational speed.

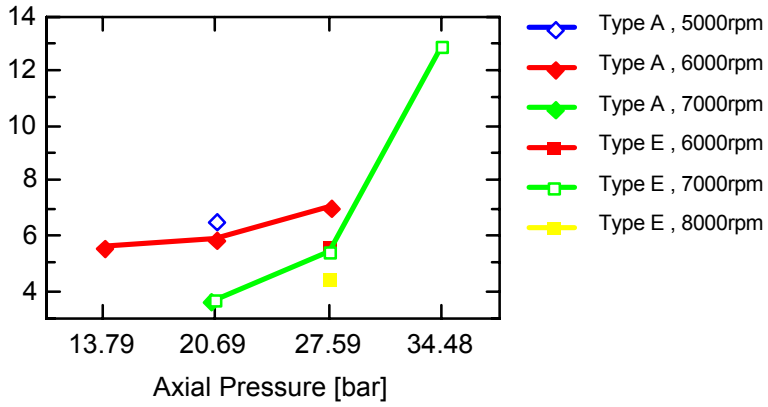

Figure 7-38: Energy input rate of type A and type E welds with different welding parameters.

Two macrographs of welded force-measurement samples (IP-A011 and IP-E010) are shown in Figure 7-39, while the force diagrams are shown in Figure 7-40 for the type A welds and in Figure 7-41 for the type E welds. The measurements started simultaneously with the DRS measurements for a duration of 30 seconds. The load cell in the bottom of the hole (Load Cell 1) gives the first response at the touch down of the stud tip on the bottom of the hole. The load cells in the side of the hole (Load Cell 2, 3 and 4) measure forces as soon as the hole is filled. The welding duration is marked in the graphs and can be seen as a sharp bend in most of the curves. As no forging pressure was applied after the weld, the maximum loads were measured during the weld. Once the weld is stopped, the particular welding force is applied for additional three seconds without rotation of the stud. After this period the axial force is completely released. During this time the measured forces further reduce and sometimes even show negative values. These negative values have been measured because the load cells were pre-loaded before the weld.

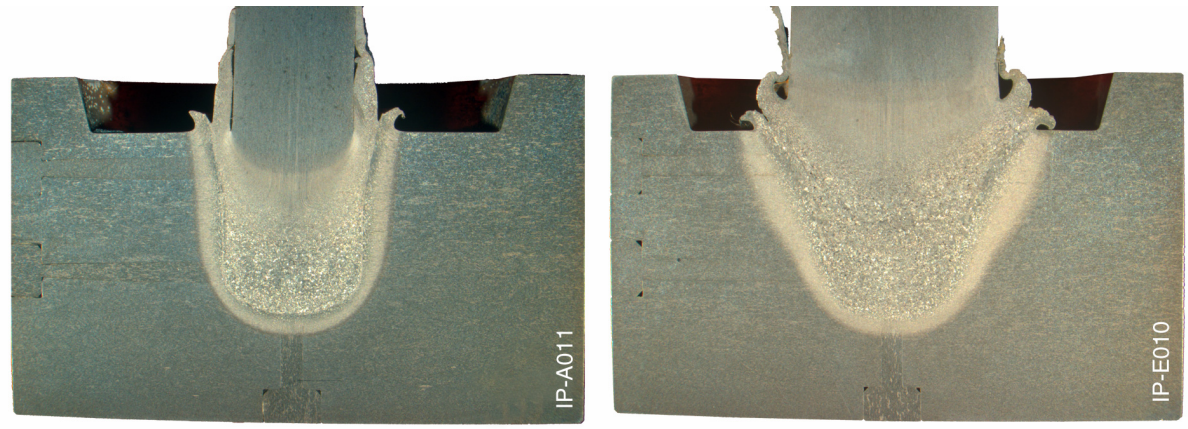

Figure 7-39: Macrographs of force-measurement samples IP-A011 and IP-E010 with three of the four pistons visible on the left sides and on the bottom.

The load cell 1 was sometimes loaded above the measuring range of maximum 2500 N. Values above this limit were not displayed correctly. It was expected, that from an axial pressure of 20.69 bar onwards this load cell might be over loaded. Unfortunately a piezo-electric load cell with higher capacity was not available in suitable dimensions.

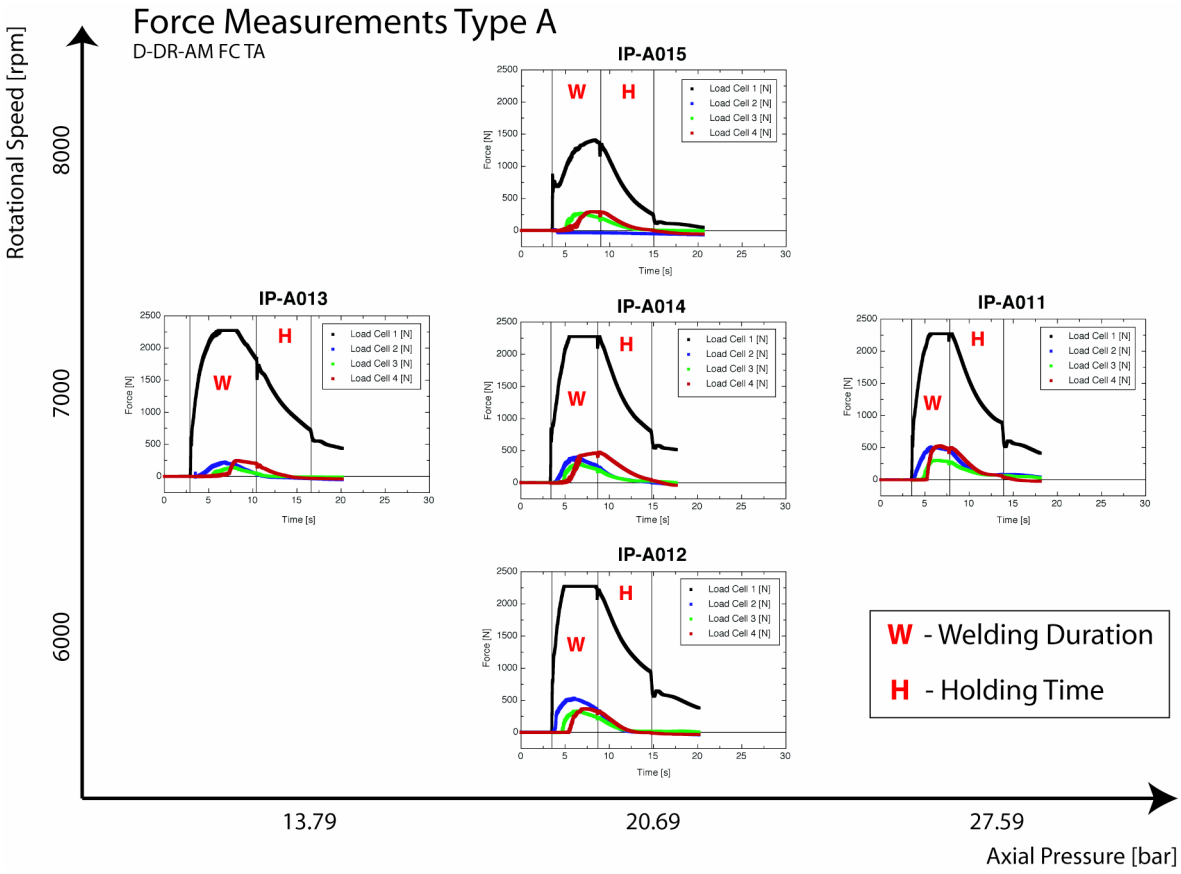

Figure 7-40: Force measurements of welding parameter matrix, Type A.

Nevertheless, the measured data of load cell 1 showed a complex behaviour in respect of maximum values, whereas the load cells 2, 3 and 4 gave reasonable results. It should be noticed that on all welds the maximum forces measured on load cell 3 (middle of the hole depth) were lower than the ones from load cell 2 and 4. The maximum values for load cell 2 and 3 rise with increasing axial pressure in type A welds (IP-A013, A014 and A011) as well as in type E welds (IP-E013, E014, E010). An influence of the rotational speed on the force measurements could not be found in type A (IP-A012, A014, A015) nor in the type E geometries (IP-E012, E014, E015). The different shape of stud and hole influences the maximum values of load cell 2 and 3 not to such an extend which should be expected based on the literature [121]. Only load cell 4 sometimes gave higher readings in the tapered geometry (type E).

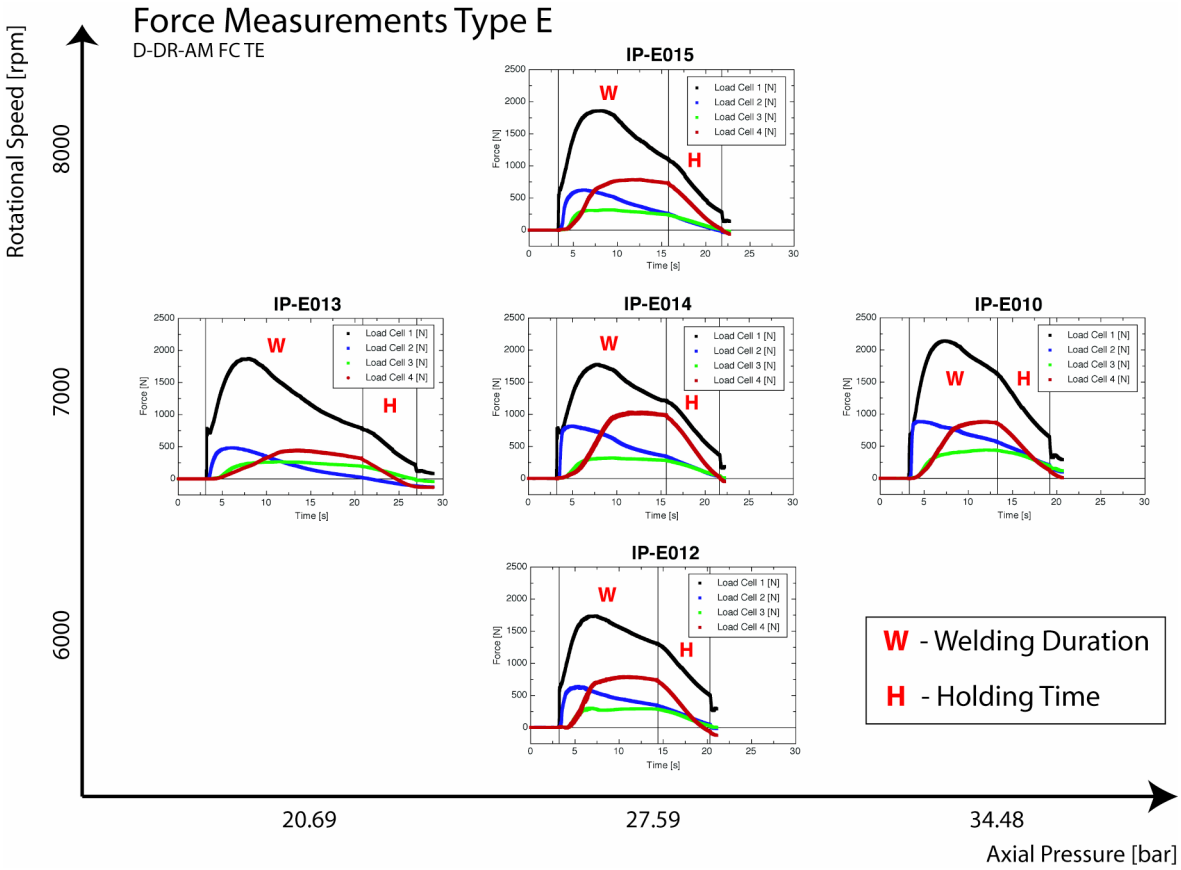

Figure 7-41: Force measurements of welding parameter matrix, Type E.

The measurements clearly demonstrated that the theory of a hydrostatic transfer of the applied axial pressure, as described in chapter 3, cannot be considered to be fully applicable. Other mechanisms have to be taken into account as well.

The development of the plastification with increasing burn-off is shown in Figure 7-42. It can be seen, that the shape of the frictional plane changes within the duration of the weld. At the beginning it starts with a relatively flat shape across the stud tip, while it changes to a conic shape at the middle of the weld. To the end of the weld the frictional plane is significantly flatter again, as soon as the plasticised material can exit the hole forming the flash. As the

pictures all have 1 mm distance in burn-off, it can be seen that in the beginning the frictional plane rises the hole much faster than to the end. This means, that in the beginning the plasticised material is deposited inside the hole to a greater rate than to the end of the weld, were most of the plasticised material is pressed in the flash.

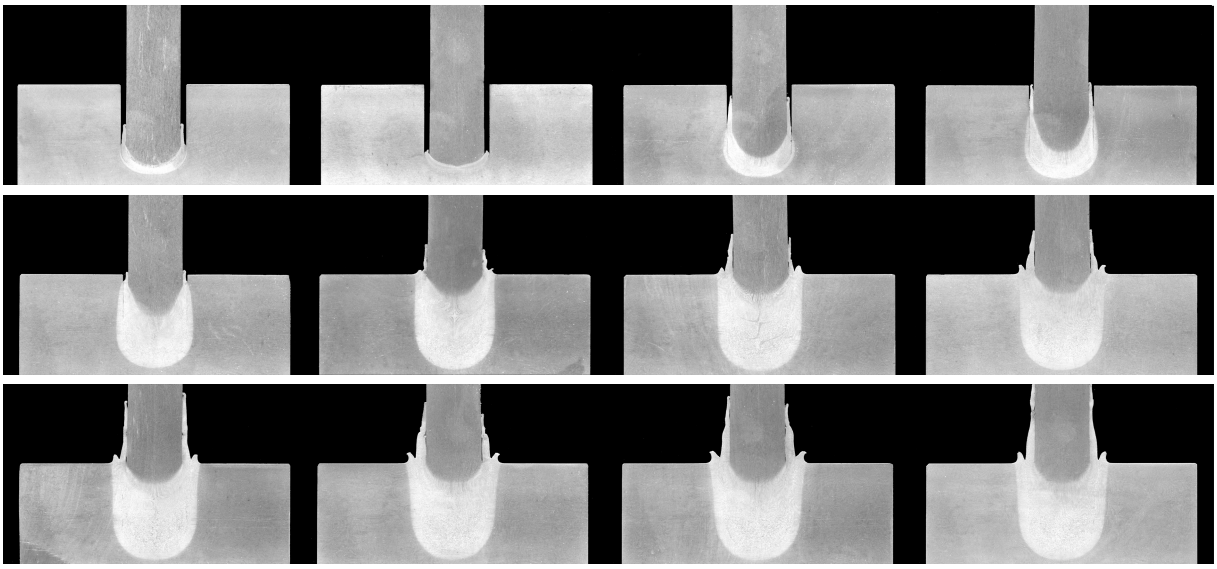

Figure 7-42: Sequence of cylindrical FHPP macrographs. Welds with increasing burn-off (1 to 12 mm) illustrate the development of plasticised material and change in shape of the frictional plane.

7.5 Mechanical Properties of FHPP Welds in High Strength - Low Alloy Steel (API 5L X65)

A comprehensive presentation of the achievable mechanical properties of single FHPP welds in high strength – low alloy steel (API 5L X65) is presented in the following chapters. The results are based on the process optimisation presented in the previous chapters and state the optimum properties achievable with the described welding system. The material combination was base material 02 for the studs and base material 03 for the plates (see chapter 6.1.2 and 6.1.3).

7.5.1 Microstructure

The microstructural examination was focused on the following specimens, which represent the two extremes in geometry:

– CA-A016: Cylindrical geometry, 3.8 s welding duration with 7.05 kJ/s energy input resulting in a total energy of 27 kJ. The top temperatures in the HAZ were up to 900 °C with a $\Delta t_{8\text{-}5}$= 3.1 to 3.6 s.

– CA-E016: Tapered geometry, 7.4 s welding duration with 12.91 kJ/s energy input resulting in a total energy of 96 kJ. The top temperatures in the HAZ were up to 1100 °C with a $\Delta t_{8\text{-}5}$= 6.9 to 8.7 s.

The following abbreviations were uses according to IIW sub-commission IX-J [138]:

F	Primary ferrite
GF	Grain boundary ferrite
PF	Intragranular polygonal ferrite
AF	Acicular ferrite (Widmanstätten and isolated laths of high aspect ratio)
AC	Ferrite with aligned MAC (Martensite, austenite or carbide)
FC	Ferrite-carbide aggregate (Pearlite or ferrite with interphase carbides)
M	Martensite

Although the terminology proposed above [138] has been specially devised for deposited ferritic weld metals, it has been shown to serve as a basis to describe the microstructures observed in this work.

In general the microstructure of specimen CA-A016 shown in Figure 7-43 consists of a homogenised area in the lower consumable stud and a region of plastically deformed stud material in the upper part.

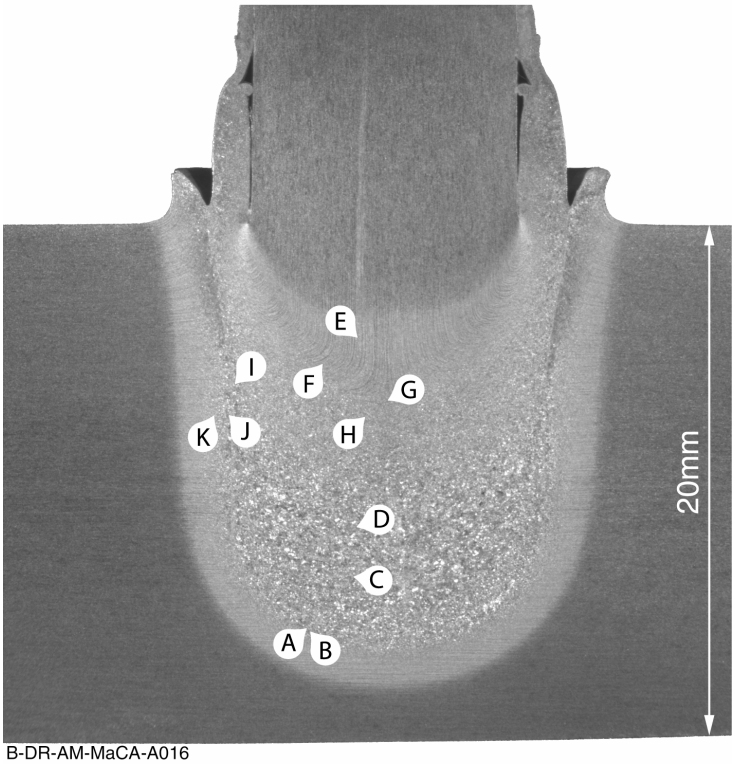

Figure 7-43: Regions of microstructural analysis on specimen CA-A016.

Figure 7-44: Microstructure in region A, bonding line indicated with arrows (original magnification: 500x).

Figure 7-47: Microstructure in region D (original magnification: 500x).

Figure 7-45: Microstructure in region B, bonding line indicated with arrows (original magnification: 1000x).

Figure 7-48: Microstructure in region E (original magnification: 500x).

Figure 7-46: Microstructure in region C (original magnification: 500x).

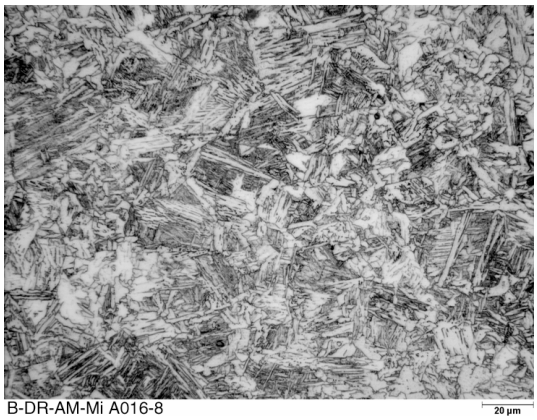

Figure 7-49: Microstructure in region F (original magnification: 500x).

Figure 7-50: Microstructure in region G (original magnification: 500x).

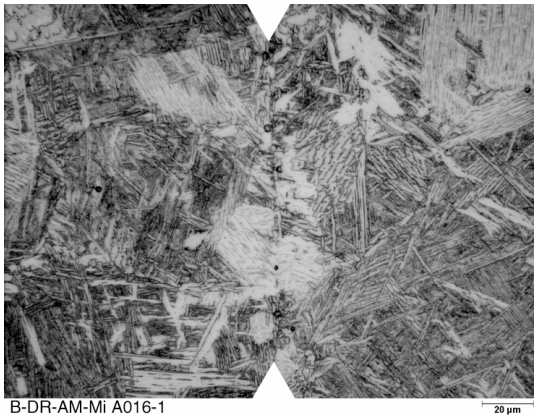

Figure 7-53: Microstructure in region J, bonding line indicated by arrows (original magnification: 500x).

Figure 7-51: Microstructure in region H (original magnification: 500x).

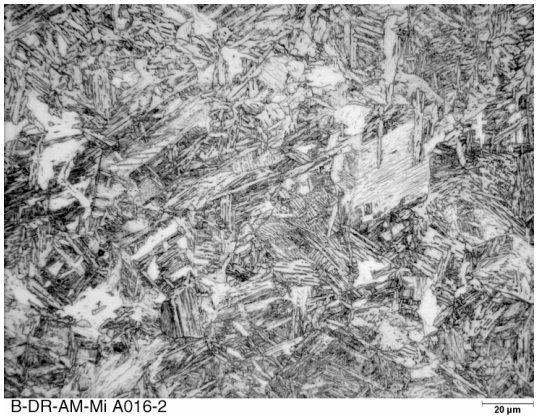

Figure 7-54: Microstructure in region K (original magnification: 500x).

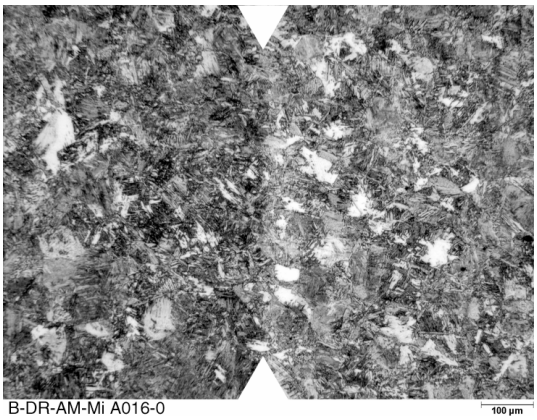

Figure 7-52: Microstructure in region I, bonding line indicated by arrows (original magnification: 100x).

The bonding line at the bottom of the hole cannot be clearly identified even at high magnifications (Figure 7-44 and Figure 7-45). The microstructure in the bonding area consists of a mixture of AC and M, as a result of the relative high cooling rates at the beginning of the weld. The homogenised region mainly contains finer AC colonies and M (Figure 7-46). Moving up the consumable stud, the structure becomes coarser as shown in Figure 7-47. The globularisation of the pearlite in the segregation bands is shown in Figure 7-48 in the stud-HAZ with equi-axed ferrite grains in between. Close to the final frictional plane the structure changes to fine-grained F and AF (Figure 7-49). In the centre of the final frictional plane, where almost no relative movement occurred, a region of AF with fine AC can be found (Figure 7-50). The grain size changes from fine, possibly dynamic re-crystallised grains in the area of frictional contact (Figure 7-51) to coarser grains in the homogenised regions in the lower consumable stud area (Figure 7-47).

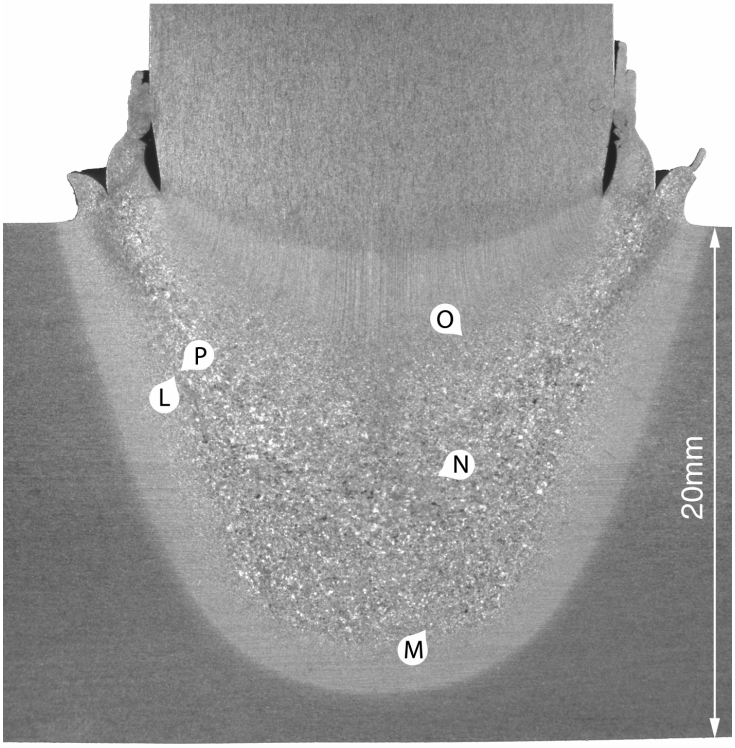

B-DR-AM-MaCA-E016

Figure 7-55: Regions of microstructural analysis on specimen CA-E016.

A clear carbon depleted band along the bonding line to the side of the hole is shown in Figure 7-52, which might be caused by carbon loss at elevated temperatures. Contrary to the bonding line at the bottom, the bonding line to the side can be observed in some areas (Figure 7-53). The HAZ of the base material shows AC and M near the bonding line (Figure 7-53) and a mixture of AC, AF and FC further away (Figure 7-54) as a result of the less harsh cooling conditions.

Figure 7-55 shows a macrograph of specimen CA-E016 with areas indicated for microstructural analysis.

Owing to the approximately three times higher heat generation and flatter thermal cycle, the AC and GF grains in the HAZ (Figure 7-56) and the stud material itself (Figure 7-57) are significantly bigger. The constitution in the stud material near the bottom bonding line is mainly AC with AF and M (Figure 7-57). The grain size increases at the upper part of the homogenised region where larger primary ferrite and AC can be found (Figure 7-58). The microstructure corresponds well with the micro hardness results which did not exceed

350 $HV_{0.2}$ (Figure 7-62). The grain size reduces significantly when crossing the final frictional plane in the upper weld area, showing AF in Widmanstätten configuration and AC (Figure 7-59).

The side bonding line (Figure 7-60) reveals a combination of AF, FC and M due to the high maximum temperatures and faster cooling rates in this region. The adjacent base material HAZ (Figure 7-56) depict coarser grain structures than in specimen CA-A016 (Figure 7-54) with GF and AC.

It was tried to establish a comparison between the found microstructure with the associated measured cooling times and a CCT diagram. The required CCT diagram for the API 5L X65 material could not be provided by the manufacturer nor found in the literature.

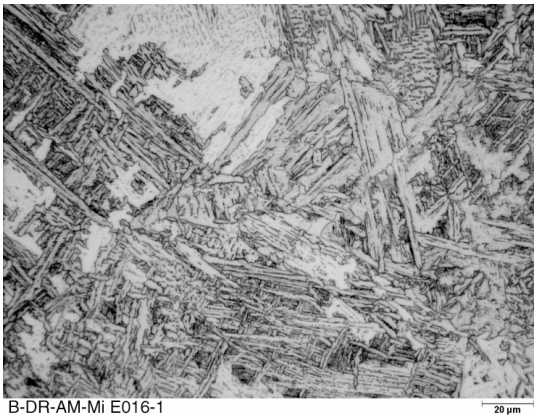

Figure 7-56: Microstructure in region L (original magnification: 500x).

Figure 7-58: Microstructure in region N (original magnification: 500x).

Figure 7-57: Microstructure in region M (original magnification: 500x).

Figure 7-59: Microstructure in region O (original magnification: 500x).

Figure 7-60: Microstructure in region P (original magnification: 500x).

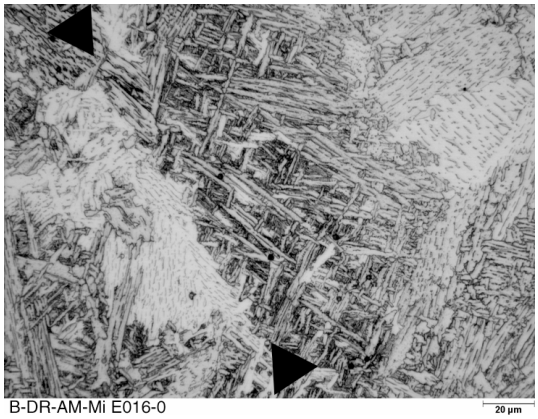

7.5.2 HARDNESS

All welds show increased hardness values in the HAZ and the consumable stud, while the maximum values were observed in the consumable stud itself. The hardness profiles of the two specimens subjected to the microstructural analysis presented in the chapter before are shown in Figure 7-61 and Figure 7-62. Owing to the relatively flat temperature cycle the tapered specimen (Type E, Figure 7-62) shows the lowest hardening in the HAZ and the consumable stud. The maximum hardness values were measured in the consumable stud area with around 360 $HV_{0.2}$ for the tapered geometry, while hardness values of up to 460 $HV_{0.2}$ were measured for the cylindrical specimen A016 (Figure 7-61). Further hardness profiles for the different geometries can be found in Figure 7-29 to Figure 7-33.

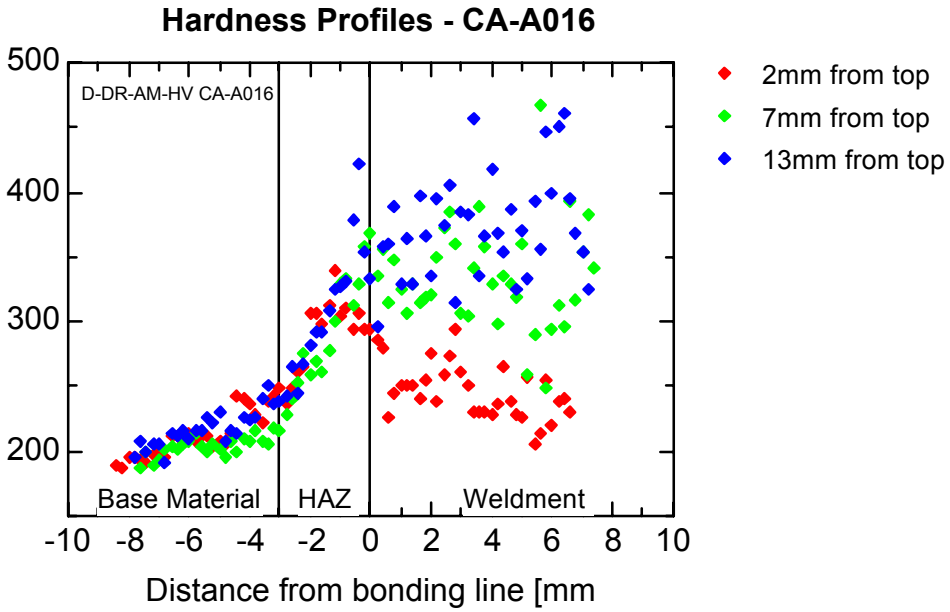

Figure 7-61: Hardness profiles of cylindrical specimen CA-A016.

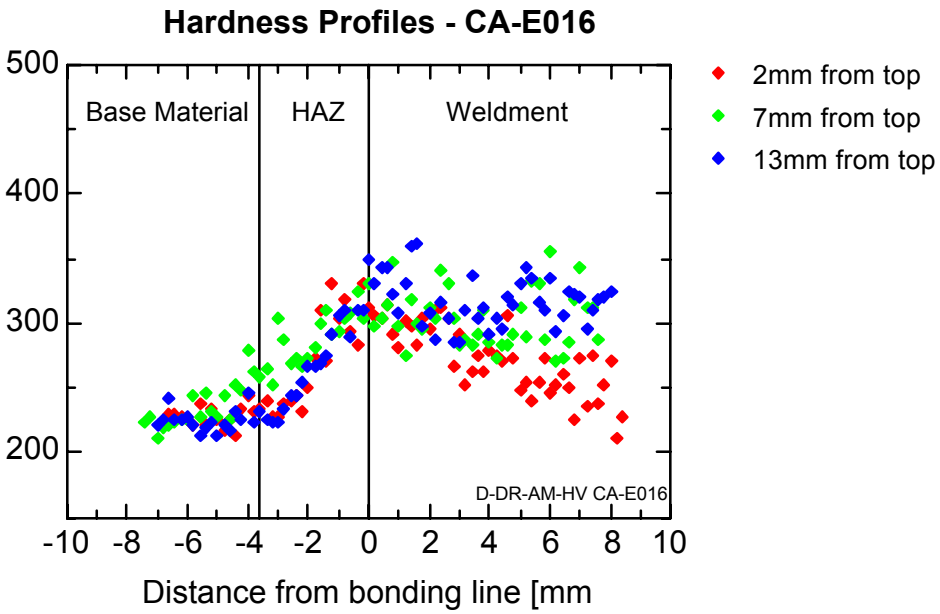

Figure 7-62: Hardness profiles of tapered specimen CA-E016.

7.5.3 Tensile Strength

Tensile tests in round specimens were performed to evaluate the bonding properties and the quality of the joint as described in chapter 6.5.5. These results have already been presented in chapter 7.4, Table 7-4.

It can be seen that all specimens almost reach the base material values in yield and tensile strengths. The reduced elongation of the welded specimen is mainly due to the concentration of deformation in soft regions present in the gauge length of the tensile specimen. Failure always occurs in the base material outside the HAZ.

7.5.4 Bending Test Results

The bend tests show, that with optimised geometry combinations and welding parameter 170° bend angle can be achieved. Bend test specimen with the tapered hole geometry as well as with the cylindrical hole shape pass the bend tests without any defects, as shown in Figure 7-63.

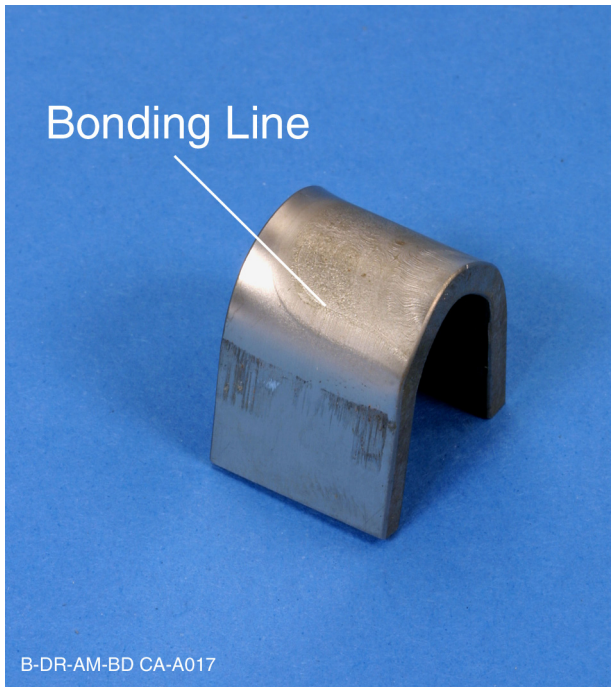

Figure 7-63: Bend test specimen CA-A017 (Cylindrical hole geometry).

7.5.5 Charpy Impact Toughness

As presented in chapter 7.4, all geometries showed relative high Charpy toughness values (Figure 7-34). A mean value of 81 J was achieved with the cylindrical geometry (Type A) at –20 °C. The notch was machined in the bonding line along the plate thickness. The problems associated with the notch positioning were discussed in detail in chapter 7.4. Nevertheless, all geometries would pass the requirements of relevant codes and standards for welding of steel pipelines [139], with a required minimum value of 40 J at -10 °C.

7.6 Summary & Discussion on Mechanisms, Control and Thermal Processes of FHPP

The results presented in chapters 7.1 to 7.3 are summarised and discussed in detail below. The knowledge gained is then used to propose a bonding mechanism for FHPP welds in steel at the end of this chapter.

7.6.1 General Influence of Process Parameters

As a result of the limited literature available on FHPP, the results can mostly be only compared to standard rotational friction welding where possible.

As observed by Vill [79] and Voinov [99] in standard rotational friction welding of steels, increasing rotational speed led to wider HAZs. The same behaviour has been found by subjective observation in the presented work. As shown in Figure 7-64 the size of the HAZ

increases with higher rotational speeds. A change in the shape of the HAZ due to the rotational speed as reported by Ellis [85] could not be observed. This phenomenon is only related to standard rotational friction welding, where the frictional plane stays on position and the plasticised material which is pressed in the flash is no longer part of the actual friction process. This plasticised material actually removes a large quantity of heat energy out of the frictional interface [140], whereas in FHPP the frictional plane moves up the hole and the plasticised material stays in contact with the frictional plane. The shape of the HAZ is therefore influenced by the rotational speed, as the source of energy, and the burn-off rate. The burn-off rate reduces when the frictional plane reaches the top of the hole and the hole diameter virtually increases. At this stage the FHPP process changes to almost standard friction stud welding and the frictional plane almost stays at one level near the plate surface. Owing to this the shape of the HAZ widens at the top.
Higher rotational speeds should also give lower burn-off ratios and longer heating times as reported by Lucas [100], which can be found in Figure 7-3 and Figure 7-4. The higher rotational speeds combined with the higher heating times give a higher total heat generation as found in the sizes of the HAZs in Figure 7-64.

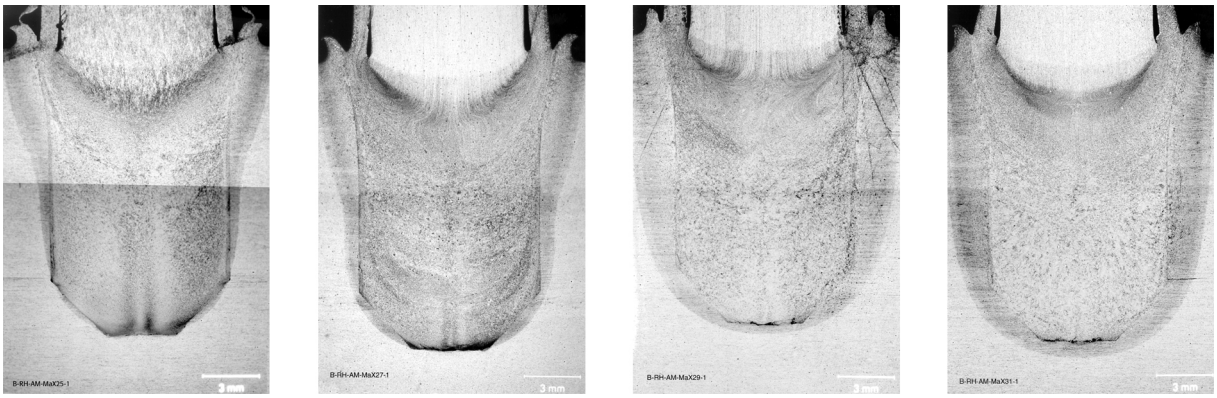

Figure 7-64: Macrographs with constant axial force, but increasing rotational speed (4000, 5000, 6000 and 7000 rpm).

However, the hardness measurements presented in Figure 7-65 do not show a clear difference in the maximum values as a function of the rotational speed. The maximum values in the consumable stud vary from 300 to 400 $HV_{0.2}$. Lower rotational speeds are more likely to produce lower hardness values. These results exhibit a tendency similar to that reported by Ellis [85]: While varying rotational speed from 975 to 1825 rpm the maximum hardness values in mild steel only change from 190 to 205 HV_{20}.

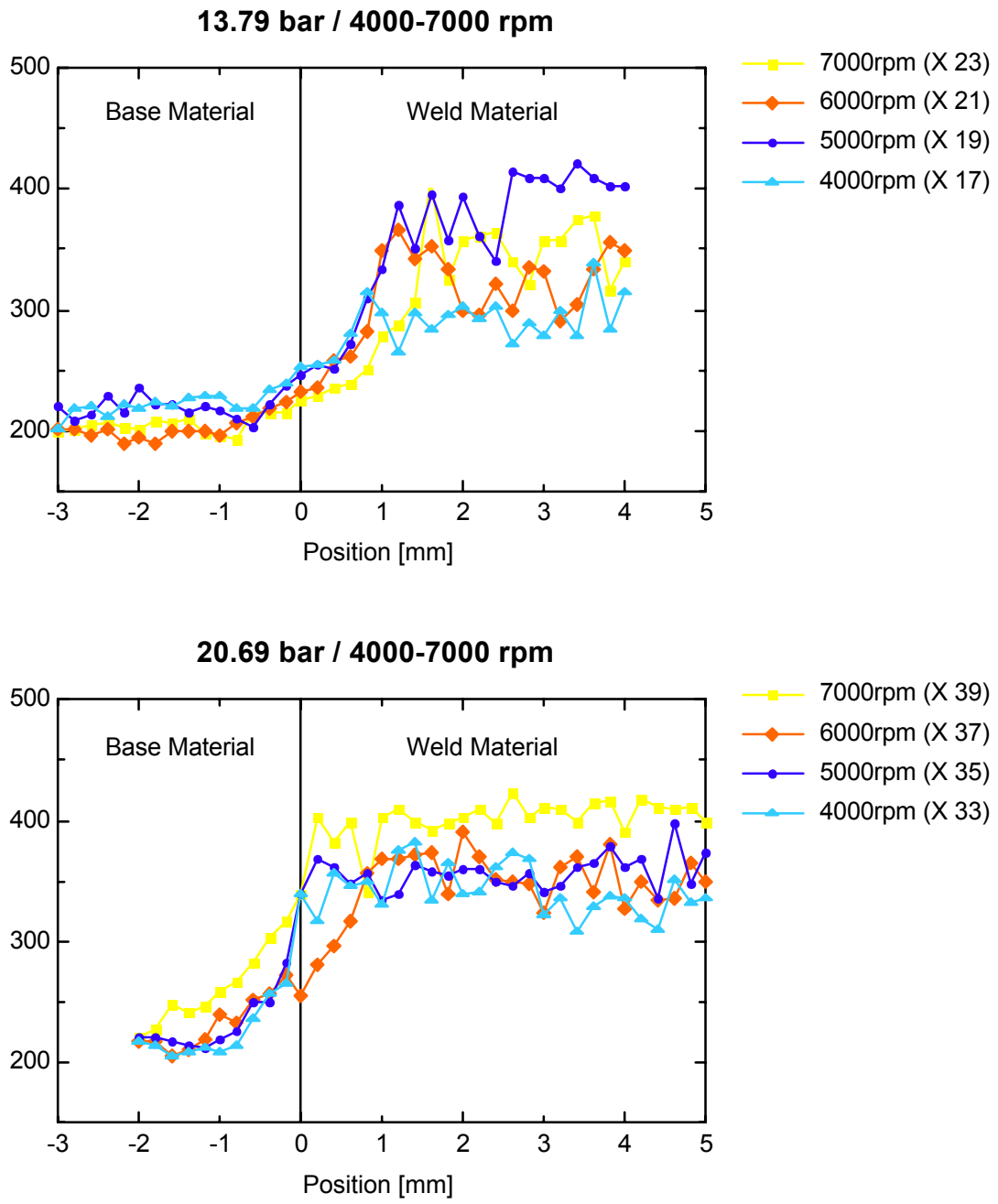

Figure 7-65: Hardness profiles for 13.79 and 20.69bar axial pressure and different rotational speeds.

Ellis [85] described the relationship between axial pressure and burn-off rate as a linear correlation, were the burn-off rate rises with increasing axial pressure. The same correlation was found in the present study as shown in Figure 7-4. Increasing axial pressure clearly increases the burn-off ratio, which results in shorter heating times and narrower HAZs. It should be mentioned that the influence of the axial force in the examined parameter ranges is more significant than the rotational speed. Ellis [85] reported no changes in hardness values due to the axial pressure, only the shape of the hardness profile changed in the reported experiments from an almost parallel sided boundary at low pressures to a more pinched or double coned profile at the centre of the bar at the highest pressures.

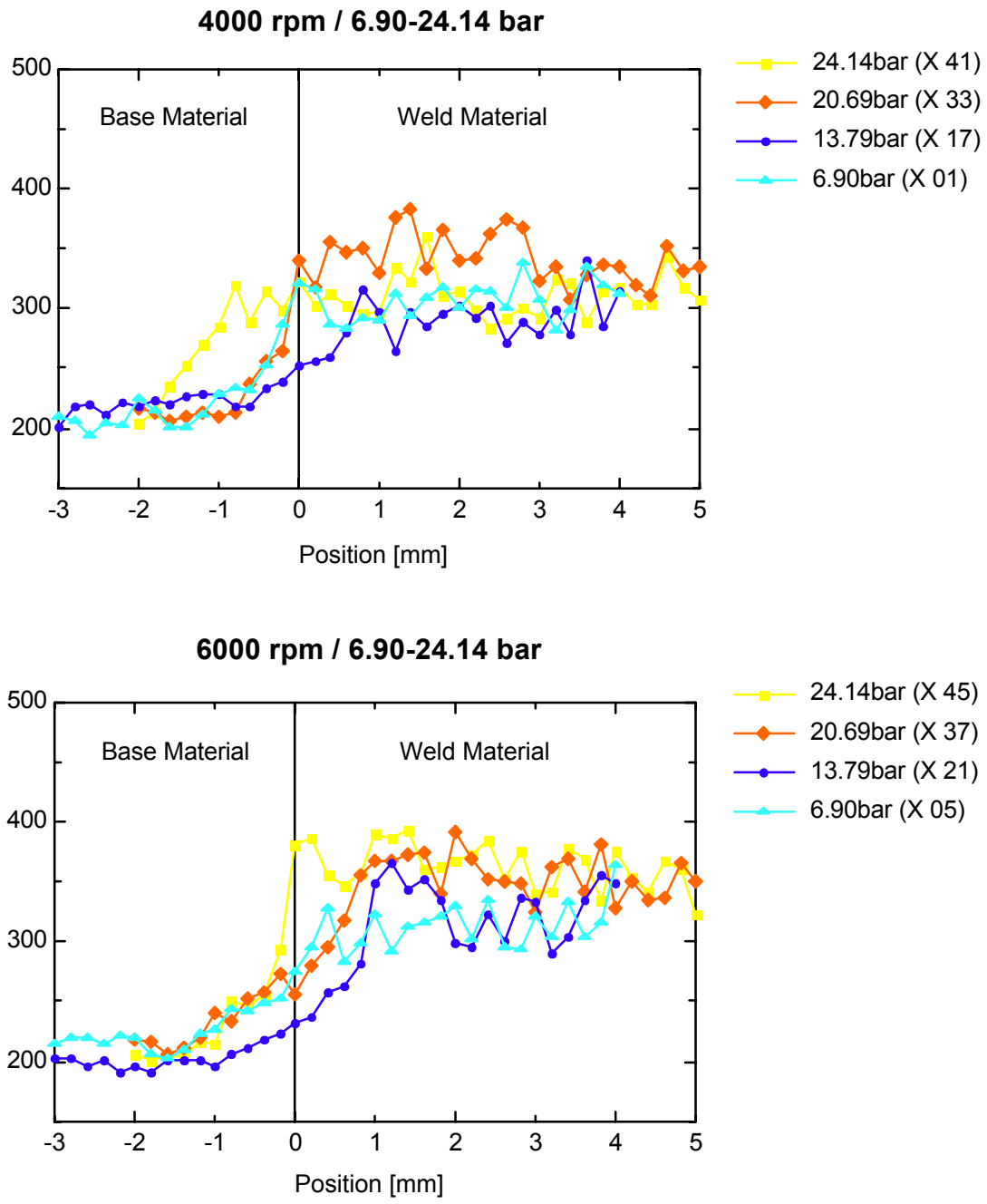

Figure 7-66: Hardness profiles for 4000 and 6000 rpm rotational speed and different axial pressures.

The macrographs presented in Figure 7-2 and Figure 7-64 show clearly that an optimised geometry combination of stud and hole is essential for sound bonding all around the interface. In all welds the transition from the bottom of the hole to the sides shows significant lack of bonding. This emphasises the requirements for a detailed investigation on material transport during FHPP and development of a suitable stud and hole shape.

7.6.2 Plastification and Material Transport

The experiments with different cone angles at the tips of the studs, combined with the results of the chamfered geometry experiments showed that the quality of the bonding at the bottom area of the weld is mainly influenced by the geometry of the hole. The bonding at the flat part of the hole bottom is only depending on the welding parameters and does not change as a function of the different cone angles at the tip of the studs. The fact that the axial pressure significantly influences the quality of the bonding is well-known from standard rotational friction welding [85]. The chamfered geometry experiments showed, that if the initial contact area is too large, the torque peak at touch down might shear off parts of the stud without plastification. Specimen N04 (Figure 7-12) showed that the whole tip sheared off without significant plastification briefly after the initial contact of the stud with the hole bottom. This only happened with the geometry where the stud and the hole had the same chamfer angle. The welds with a certain difference in the chamfer angle (N06 and N08) showed different behaviour (Figure 7-12). If the initial contact area is reduced to the flat bottom only, the torque peak is reduced when the cold surfaces make first contact. Owing to the difference in chamfer angle the size of the contact area of the stud gradually increases. The production of plasticised material decreases the frictional torque as well. On the other hand with decreasing initial contact area, the rotational speed at touch down has to be increased to ensure the required relative velocity.

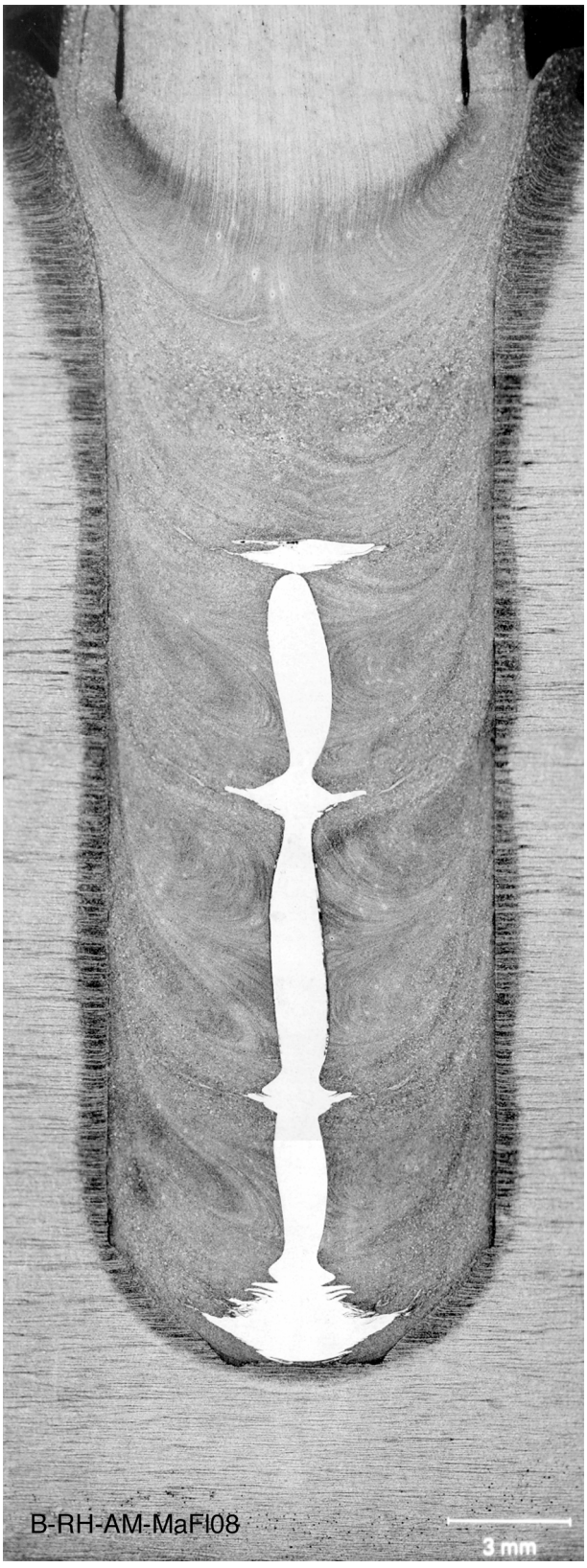

Figure 7-67: Macrograph of specimen Fl08, welded with nickel tracer rod in API 5L X65 base material.

Nevertheless the chamfered geometry experiments showed unexpectedly that the supposed contact on the chamfer angles of the hole is not enough to create sufficient heating and bonding.

The shear planes mentioned by Nicholas [112] could be perfectly visualised with the nickel tracer rods (Figure 7-13). Based on this work [112] the welds Fl01, Fl04 and Fl07 should have given optimum results, as the plastification gradually rises in the hole without significant distances between shear planes. Unfortunately those welds show almost no HAZ at the sides of the hole and correspondingly no bonding. This might be a result of the different stud diameters (20 mm) and machine concepts applied. Nicholas [112] used big stationary workshop machines limited to low rotational speeds, applying high axial pressures, while the system employed for the presented work makes use of high rotational speeds and low axial pressures.

Figure 7-67 shows weld specimen Fl08 welded with 5000 rpm and 20.69 bar. The nickel tracer shows, that at the beginning of the weld a significant amount of stud material is plasticised and pressed in the gap between stud and hole. Only in the bottom area the nickel tracer is moved out of the centre over a bigger area. This happened another three times along the weld with reduced amount of nickel material. Those three areas depict shear planes. Between the shear planes the plastification of the nickel is considerably less. This means that after a certain amount of plasticised material is produced at the beginning of the weld, it is pressed up the gap between stud and hole. Owing to the frictional heat the stud material is heated as well. The plasticised material in the gap cools down in contact with the cold plate and increases the torque on the stud. As reported by Nicholas [112], this results in shearing of a certain amount of stud material. After this the process continues on top of the sheared stud material, creating a new HAZ, which can be seen in Figure 7-67 in the curved border of the HAZ. The number of shear planes and the distance in between depends on the process parameters and the material properties (i.e. tensile strength at elevated temperatures).

The improved design of the bottom of the hole with a rounded transient showed as expected, that only after increasing the stud diameter to 10 mm the quality of the bonding improved. With 8 mm diameter studs the initial contact area was too small and the maximum rotational speed of the welding system was not high enough to create the required relative velocity. This geometry gave the first fully bonded and defect free FHPP-welds with this system. Further experiments with this geometry and different hole diameters showed that sound welds could be produced with this geometry over a wide range of hole diameters. The 12 mm hole diameter was selected for the further investigations based on the good bend test results (158°) and the good overall system behaviour (i.e. limited rotational speed variations). After a welding parameter optimisation a window of appropriate welding parameters was established for this geometry and material combination. The hardness survey in Figure 7-20 shows an increased hardness of around 300 $HV_{0.2}$ in the consumable stud area. The profile in 2 mm distance from the surface clearly shows an increased hardness in the HAZ, and values of around 200 $HV_{0.2}$ in the consumable stud area again. This is caused by the fact that the final frictional plane (when the weld was stopped) is below this line. The vertical hardness profile

shows this fact as well. Owing to this profile the final frictional plane was in around 5mm distance below the plate surface (measured at the centre line of the stud).
Additional experiments with tapered stud and hole geometry showed very good bend test and Charpy impact properties (Table 7-2). This is probably due to the same bottom design as used for the parallel-sided ones, and the additional forces to the wall of the hole by the taper angle. Unfortunately, this geometry is limited to reasonable shallow holes, as with increasing hole depth the top diameter of the stud increases as well. The maximum stud diameter is limited by the machine capabilities. With increasing stud diameter the required axial force increases, which might limit the stud size for certain applications.
The hardness survey for specimen TS20 presented in Figure 7-22 shows the same characteristics as the one for the parallel-sided specimen in Figure 7-20. The microstructural and mechanical properties of these tapered welds in S235 material will be discussed in more detail in chapter 7.6.1.

7.6.3 THERMAL PROCESSES

Vill presented in 1959 a relation for the heat generation N during friction welding [92]:

$$N \approx 2\pi p \frac{K}{n} r \cdot 10^{-6} \qquad \text{[kW]} \tag{7-6}$$

p – Axial pressure [kg/mm^2]
K – Material dependent constant [mm^2/min^2]
n – Rotational Speed [1/min]
r – Radius of the cross section [mm]

It can be clearly seen that the heat generation should be higher with low rotational speeds n and higher axial pressures p. Figure 7-25 showed that with higher axial pressure (specimen TC-A001) the temperature rises with about 270 °C/s (100 °C to max. temperature), while lower axial pressure (specimen TC-A003) results in a heating rate of 140 °C/s. This is caused by the relative higher heat generation with higher axial pressure. The maximum temperatures observed vary only between 800 °C and 950 °C without a clear correlation to the welding parameters (Figure 7-26). Similar temperatures were measured by Suga et al. [31] for friction welding of carbon steel. Temperatures between 800 and 1100 °C were measured in 0.5 mm distance to the faying surfaces, while higher axial pressures led to higher temperatures [31]. Nevertheless at 6.90 bar axial pressure the heating gradient reduces from 177 °C/s at 100-700 °C, to 46 °C/s near the maximum temperature (700-800 °C). This indicates that an equilibrium stage is almost achieved. Compared to the high axial pressures (27.59 bar) the heating rate indicates that an equilibrium stage is not yet reached and the temperature would rise, if the process would continue (117 °C/s at 700-888 °C). Figure 7-26 shows as well that higher rotational speeds give lower heating rates and lower maximum temperatures, which correlates with the relation of Vill presented above. Although the total energy rises with increasing rotational speed, the converted heat energy reduces due to the changed friction conditions [79, 99]. The reduced heat production at

higher rotational speeds results in longer welding durations as the rate of plastification depends on the heat generated.
The influence of the geometry combination and especially the stud diameter can be seen in Figure 7-27. The maximum temperature rises with the stud diameter from 800 °C with 10 mm diameter (type A) to 1100 °C with 18 mm diameter (type E) on the tapered stud owing to the increased surface of the frictional interface. All curves showed the phenomenon that the temperature in the middle of the plate thickness (N°3 + N°4) is approximately 200 °C higher than at the bottom (N°5) or at the top of the plate (N°1 + N°2). This could be explained by the fact that the plate and the stud materials are cold at the beginning of the process and more energy is needed to heat up the stud and the plate. In addition to this the cold welding rig dissipates heat especially in the bottom region as well. Owing to this the temperature at the bottom position (N°5) is mainly controlled by heat dissipation from the weld after it already passed the level of this thermocouple (N°5). Shternin [140] reported that the plasticised material takes most of the heat when it is pressed in the flash. Thus the lower temperatures of thermocouple N°1 and N°2 might be caused by the fact, that the plasticised material, can no longer be held inside the gap between the stud and the hole and just passes by the positions N°1 and N°2 without significantly heating the base material. In addition some of the plasticised plate material is pressed out and forms the smaller flash on the plate surface, called secondary flash. This leads as well to the problem, that thermocouple N°1 and N°2 can be plastically deformed during the weld and the distance to the frictional plane might change. The only area where the heat could be held for a while is the middle area of the weld (N°3 and N°4).

7.6.4 Bonding Mechanism

The results presented in chapter 7.4.2 clearly showed, that the bottom geometry developed before (see chapter 7.2) could be used for a variety of hole shapes providing defect free welds in all geometry combinations. The bend and tensile tests proved the sound bonding to the sides of the holes in all cases. The results of the round tensile tests shown in Table 7-4 clearly depict the overmatch condition of the consumable stud material. The tensile strength is for all geometry configurations in the level of the base material, while the elongation reduces with increasing amount of weld material in the gauge length of the tensile specimen.
An influence of the geometry was markedly shown in the Charpy impact test results (
Figure 7-34) and the hardness profiles (Figure 7-29 to Figure 7-33). With increasing heat generation and welding duration as discussed in chapter 7.6.3 and shown in Figure 7-38 the maximum hardness reduces from about 460 $HV_{0.2}$ with specimen CA-A016 to about 360 $HV_{0.2}$ with the tapered specimen CA-E016. It should be noted, that with all specimens the hardness tests near the bottom and in the middle (13 and 7 mm from the top) show the highest values in the consumable stud material. The measurements near the surface (2mm from the top) give maximum values in the bonding line and a reduced hardness in the weld material again. This is caused by the fact, that the final frictional plane is somewhere below the plate surface and the line of indentations crosses the HAZ of the base material, the bonding line and goes in the HAZ of the stud again.

Comparing the hardness measurements of specimen CA-A016 in Figure 7-29 with the ones of an earlier weld with the same material combination and welding parameters in Figure 7-20 clearly shows a significant difference in the hardness values in the weld material. While the first weld shows a maximum hardness of around 330 $HV_{0.2}$ in the lower weld area, the weld CA-A016 resulted in a maximum hardness of around 460 $HV_{0.2}$. The only difference between the two welds is, that in the meantime the welding rig was changed. On the first rig, the specimens were held in a vice and the plates were only supported partially from underneath, whereas in the new welding rig, the specimens are supported underneath the full plate. Due to the enlarged contact area to the solid welding rig, specially in the close contact to the weld at the bottom, the heat conduction should be significantly increased. Thus the cooling conditions in the new weld rig should be more severe than in the former vice. This clearly demonstrates the importance of considering the cooling conditions in the respective applications in order to achieve the required properties. Temperature measurements under different cooling conditions could help to establish this influence in more detail.

The Charpy impact tests proved the good bond quality of all geometry combinations. Although the notches were positioned precisely in the bonding line the results differ unexpectedly at a first glance. The general difficulties in testing inhomogeneous specimen with this test method coincide with the problems in testing friction welds as described by Neumann and Schober [81] and Eckel [141]. Only with the cylindrical geometry (type A) the notch can be properly positioned in the bonding line, resulting in testing the aimed region. As soon as the holes have a taper angle, the notch starts to be placed partially in the consumable stud, the bonding line, and the HAZ of the base plate (Figure 6-15). Owing to this, the results do not show the properties of the aimed region, but a combination across the bonding line. Although some macrographs in Figure 7-35 show either a failure along the HAZ of the base plate (specimens CA-B026 and CA-D028) or directly along the bonding line and across the HAZ and base material (specimens CA-C025 and CA-E028), the measured impact energy was comparable. For the given size of the plates it was not possible to place the Charpy specimens with the notch parallel to the bonding line.

The micro flat tensile tests showed an increased tensile strength in the consumable stud material of up to 300 MPa compared to the base material. This correlates with information from Gibson [123] who stated an increase of 100-200 MPa when FHPP welding mild steel studs in carbon manganese steel plates due to the thermo mechanical phenomena in the consumable stud.

It could be demonstrated that the experiments for the measurements of local forces resulted in valuable information for the understanding of the FHPP mechanisms. The unexpected behaviour of the measurements of load cell 1 is probably caused by the fact, that this load cell not only measures the load applied on the piston, but additionally the deformation of the bottom of the welding plate as well. All welding specimens showed a footprint of the load cell device on the bottom side of the plate after welding. Owing to these problems, the measurements of the load cell 1 will not be considered further. The fact that the measured forces does not significantly respond to changes of the rotational speed or changes in the geometry implies that the actual forces mainly depend on the axial pressure. The reading of

load cell 4 might be influenced by plastic deformation of the piston area, especially in the tapered geometry, and should be judged with caution. The tendency of the force measurements of load cell 4 should be correct, but the actual values should not be considered.

Assuming a hydrostatic transfer of the applied axial force F_{Weld} in the plasticised material as in an ideal liquid, the horizontal forces on the load cells $F_{LoadCell}$ can be calculated by the law of Pascal:

$$F_{LoadCell} = \frac{F_{Weld}}{A_{Friction}} \cdot A_{LoadPiston} \quad [\mathrm{N}] \quad (7.7)$$

with the cross-section areas of the frictional plane, $A_{Friction}$, and the load cell piston, $A_{LoadCell}$. The respective horizontal forces on the load cells depending on the axial pressure are given in Table 7-5.

Table 7-5: Expected and measured forces on the load cells based on hydrostatic force distribution in a cylindrical FHPP weld with 10 mm stud diameter.

Axial welding pressure [bar]	Expected force on load cells [N]	Maximum measured force on load cell 2 [N]	Maximum measured force on load cell 3 [N]	Maximum measured force on load cell 4 [N]
13.79	367	228	144	251
20.69	548	406	301	477
27.59	730	513	304	530
34.48	910			

As shown in Figure 7-40, Figure 7-41 and Table 7-5 the measurements correlate with the calculated values only for the load cell 2. The measured values are all 100-200 N lower than calculated. This difference is probably caused by the friction on the surface along the pistons (see Figure 7-28).

All force measurements show app. 60 % smaller maximum force for load cell 3 compared to load cells 2 and 4. This correlates with the temperature measurements presented in chapter 7.3, where thermocouple No. 3 shows the highest maximum temperatures. Load cell 3 and thermocouple No. 3 are both on 7 mm distance to the top of the plate. From the temperature measurements in Figure 7-27 one can see that the maximum difference between thermocouple No. 5 (bottom) and No. 3 (middle) is around 200 °C. As shown in Figure 7-26 it is possible to achieve a similar temperature difference at thermocouple No. 3 by varying the rotational speed as well. If the low force reading of load cell 3 is mainly caused by the higher temperature, force measurements with different rotational speeds should result in significantly different force values. Increasing rotational speed decreases the maximum temperature and should then result in higher force measurements. As shown in Figure 7-40 with specimen IP-A012, A014 and A015 changes in the rotational speed do not change the

measured forces at load cell 3 in the expected way and proportion. As a consequence, the low forces at load cell 3 throughout the various welds cannot be caused by the different temperature conditions in the course of a weld.
It can be seen from macrographs of welds that were stopped before reaching the full burn-off (Figure 7-42) that the plane of friction changes during the weld. At the beginning it is almost flat across the whole stud diameter. At this stage a hydrostatic distribution of the axial force could be assumed and respective forces can be measured. The stud presses on a “pillow” of plasticised material in the bottom of the hole (Figure 7-68).

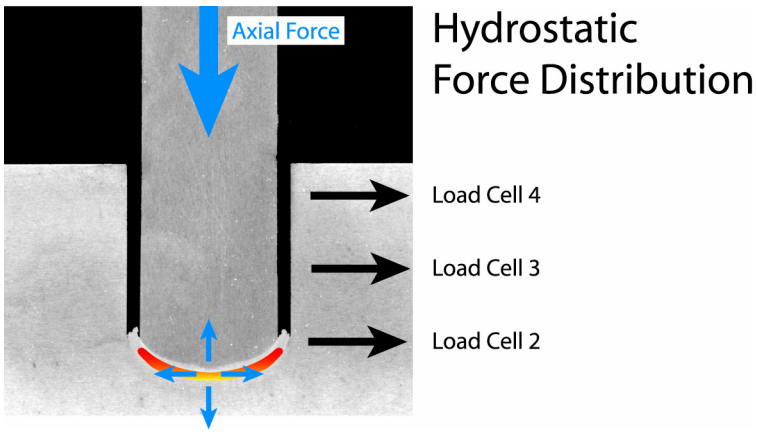

Figure 7-68: Hydrostatic force distribution in a cylindrical hole at the beginning of a weld.

After some millimetres of burn off the shape starts to change from the flat plane to a conic/hemispherical shape. Now a hydrostatic distribution of the axial force could not be assumed any more, as implied by the force measurements. If a solid body force distribution is supposed the applied axial force is diverted according to the orientation of the frictional plane. Figure 7-69 superposes the schematic force distribution and the macrograph.

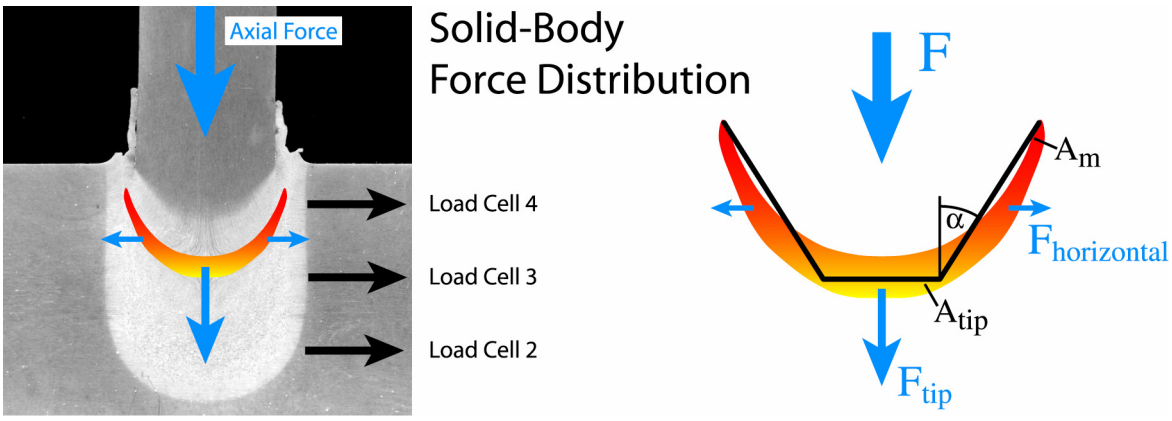

Figure 7-69: Solid-body force distribution in a cylindrical hole at the middle of a weld.

According to the shape of the frictional plane the axial force can be divided in one part which just pushes axially on the flat tip area in the centre (A_{tip}, equation 7.8) and one part that is split vectorially, first in a force normal to the frictional plane and later in a horizontal and a vertical force (equation 7.9).

$$F_{tip} = \frac{F}{A_{stud}} \cdot A_{tip} \quad [N] \tag{7.8}$$

$$F_{horizontal} = \left(F - F_{tip}\right) \cdot sin\,\alpha \cdot cos\,\alpha \quad [N] \tag{7.9}$$

The horizontal force is transferred in relation to the area A_m and A_{piston} to the force on the load cell (equation 7.10).

$$F_{LoadCell\,3} = \frac{F_{horizontal}}{A_m} \cdot A_{piston} \quad [N] \tag{7.10}$$

For the given welding conditions, the illustrated shape of the frictional plane ($A_m = 184\ mm^2$) and the described basic estimation, a force on the load cell 3 can be calculated as:

$$F_{LoadCell\,3} = 194N$$

This is just 35 % of the force calculated for the hydrostatic distribution (see Table 7-5) and approximately 100 N below the measured values.
This implies that the force distribution in the middle of the weld is mainly driven by solid body vectorial force separation with additionally hydrostatic aspects.

The welding conditions at the end of the weld (load cell 4) are very difficult to follow, as the hole itself is plastically deformed in the upper region and the frictional plane changes back to a more flat surface. This change is caused by the fact that the plasticised material is no longer retracted in the hole, but can move up the stud on top of the plate surface. This can be noticed in the relative velocity of the frictional plane as well. The velocity of the frictional surface moving up the hole is much slower near the surface as most of the plasticised material is pressed in the flash and not deposited in the hole.

Figure 7-70: Plastic deformation of piston 4 (2 mm diameter) at the bonding line interface in a tapered weld. Owing to the welding forces and temperatures associated the tip of the piston is plasticised and deformed.

The plastic deformation of the pistons in the upper hole area makes it impossible to draw any conclusions from the measured data (Figure 7-70).

It could be supposed that the force distribution reverts back to a more hydrostatic driven separation to the end of the weld, as the frictional plane reverts back to a more flat shape again (Figure 7-71). The plasticised material is mainly underneath the straight stud again and no longer on the sides of a taper-shaped stud. Forces are therefore only transmitted via the flat tip of the stud, similar to the conditions at the beginning of the weld.

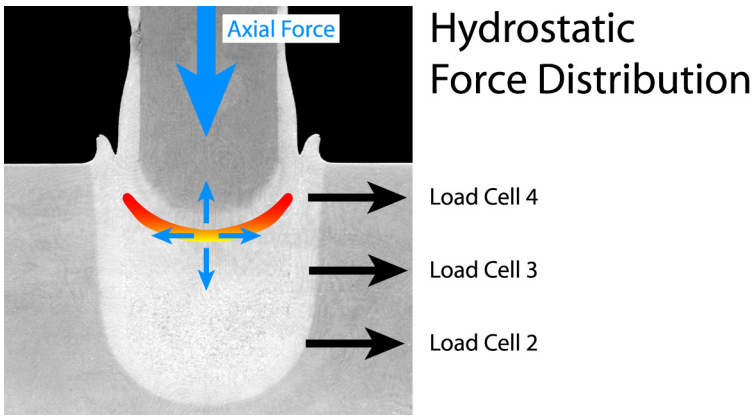

Figure 7-71: Hydrostatic force distribution in a cylindrical hole at the end of a weld.

Bearing in mind the different frictional areas, the different temperatures measured along the hole depths (as described above) can be better understood. The temperature development changes not only due to the different cooling conditions along the weld (see chapter 7.6.3), but the heat generation changes as well. The frictional plane (the area in direct contact and relative movement) changes from the basic stud diameter at the beginning of the weld to a cup and cone shaped surface in the middle of the weld. Owing to the increased contact area the heat production is higher at this stage. Combined with the lower heat dissipation at this time it results in the highest maximum temperatures in the middle area of the weld. To the end of the weld the size of the frictional plane reduces again, giving a reduced heat generation as well.

The force measurements in Figure 7-41 imply that the geometry of the stud and hole does not influence the maximum values as expected. A significant increase of the forces on the sides of the hole due to the tapered shape of the stud and the hole is not verifiable. For the same axial pressures the maximum values are similar for type A and type E geometries. The only difference is in the period of time for which the forces are applied, as the welding durations are up to three times longer than with the type A geometry. As illustrated in Figure 7-72, the shape of the frictional plane during a tapered FHPP weld is the same as during a cylindrical FHPP weld. This means that the same mechanisms can be applied to the tapered welds as found for the cylindrical welds. The axial force is split into a vertical and a horizontal part based on the shape of the frictional plane and not based on the taper angles. These forces are than transferred by a combination of solid and hydrostatic conditions via the plasticised material to the pistons in the sides of the hole. Owing to the described force transmissions the load cells only measure the horizontal part of the applied axial forces, although the piston tips follow the taper angle of the hole.

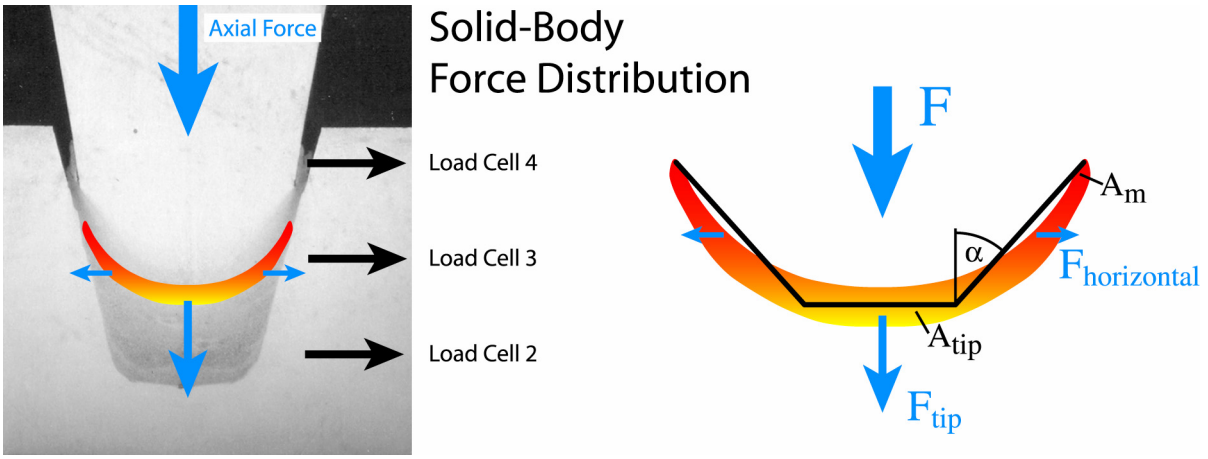

Figure 7-72: Solid-body force distribution in a tapered hole at the middle of a weld.

Using equations 7.8 to 7.10 for the tapered welding conditions at the middle of the weld and 20.69 bar axial pressure gives a calculated force on load cell 3 ($F_{LoadCell3}$) of:

$$F_{LoadCell3} = 173N$$

This is almost the same as for a comparable weld with cylindrical shape as presented above. Therefore the measured differences in the mechanical properties and the observed microstructures between the examined geometry combinations are mainly influenced by the differences in the welding durations and the thermo-cycle. This explains as well that contrary to expectations the parameter window for sound welds in tapered geometry starts at similar axial pressures as the one for cylindrical geometries, as shown in chapter 7.2. With the tapered geometry it is possible to apply higher axial loads to improve the bond quality without increasing the burn-off ratio too much. Owing to the bigger stud diameter the welding duration is longer with higher heat generation as well. The bonding surfaces stay longer at elevated temperatures and the normal forces on these surfaces are applied for a longer time as well.

The measured forces on the load cells 2, 3 and 4 (Figure 7-40 and Figure 7-41) give a pressure on the bonding line of 80-160 MPa with a maximum of 320 MPa in some cases. Comparing this to the values found in the literature for friction and forging pressures in standard rotational friction welding of mild steels (Table 2-1) shows that similar pressure ranges are used. Nevertheless 2-3 times higher rotational speeds are needed for FHPP to compensate the relatively high heat dissipation in the surrounding base plate. The fact that with FHPP a relatively small stud is welded inside a bigger base plate gives a heat flow totally different from standard rotational friction welding (i.e. bar-to-bar welds, Figure 2-1) were similar material volumes are welded onto each other.

8 Stitch Welding of Mild Steel

After characterising preliminary FHPP welds in mild steel (S235) based on the investigations presented in chapter 7.2, long stitch welds have been produced for detailed characterisation of friction stitch welds in S235 steel (base material 04 and 06).

8.1 The Stitch Welding Process

The Stitch Welding Process is basically the application of the FHPP process where a number of single FHPP welds are performed along a welding path overlapping each other for a given distance. As shown in Figure 8-1, the bore hole for the following weld is drilled partially in the consumable stud of the prior weld. Friction Stitch Welding is used for the repair of longer defects and joining plates in butt or overlap configuration.

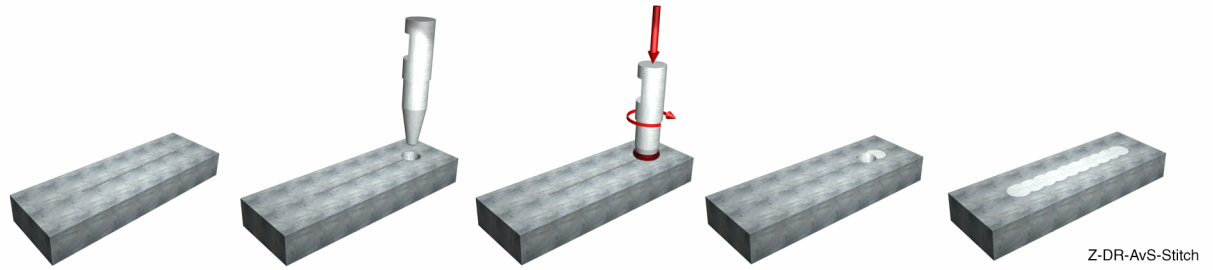

Figure 8-1: Schematic illustration of the friction stitch welding process.

Figure 8-2 shows video still images of stitch welding during the production of plates for mechanical testing for this study.

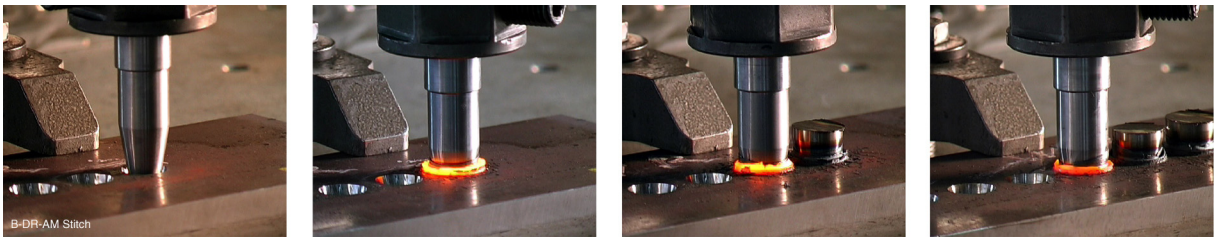

Figure 8-2: Stitch welding of a mild steel plate (taken during the production of stitch welded plates for Charpy impact testing).

As shown in Figure 8-2 the stitch welds have been produced in a special sequence to minimise the machining times. First a number of welds were produced along the welding path with a certain distance among each other. After machining off the remains of these studs, the holes for the following welds were machined with an offset of 6mm to the prior welds. The first welds have been placed in 24 mm distance to each other, which requires 4 welds to be placed in between to close the welding path. The benefit of this procedure is that a couple of holes can be machined in one machining cycle and a number of welds can be

placed in one plate before the next machining is required. All machining required within the presented work was done on a standard CNC milling machine.
Owing to the machining and transfer times involved in this procedure, the interpass temperature was effectively room temperature for all welds. Only the first welds can be considered to be the same as single FHPP welds. The following ones were welded partially in the weld material of the first welds, resulting in re-heating of this area.

8.2 Preliminary Investigations with Single FHPP Welds

A number of tapered FHPP welds (Type E geometry) were produced in DIN S235 material with optimised welding parameters as presented in chapter 7.1. The results will be used for comparison with the stitch welds performed with the same welding parameters.

8.2.1 Experimental Procedure

The welds were produced in DIN S235 base material 05 with welding studs machined from base material 04 (see chapter 6.1.4 and 6.1.5). The welding parameters used were 7000 rpm rotational speed and an axial pressure of 27.59 bar. The characterisation was performed with visual examination on an optical microscope and hardness measurements (HV_1) in 7 mm distance to the plate surface across the whole weld. Additionally some weld specimens were used for bend tests and Charpy impact tests at -20 °C. The notch was placed in the bonding line (T-position). All procedures for the characterisation are described in more detail in chapter 6.5.

8.2.2 Results

As illustrated in Figure 8-3 the examined cross sections show defect-free welds all around the bonding line. The hardness measurement demonstrates an increased hardness in the consumable stud of maximum 280 HV_1 compared to approximately 180 HV_1 in the base material.

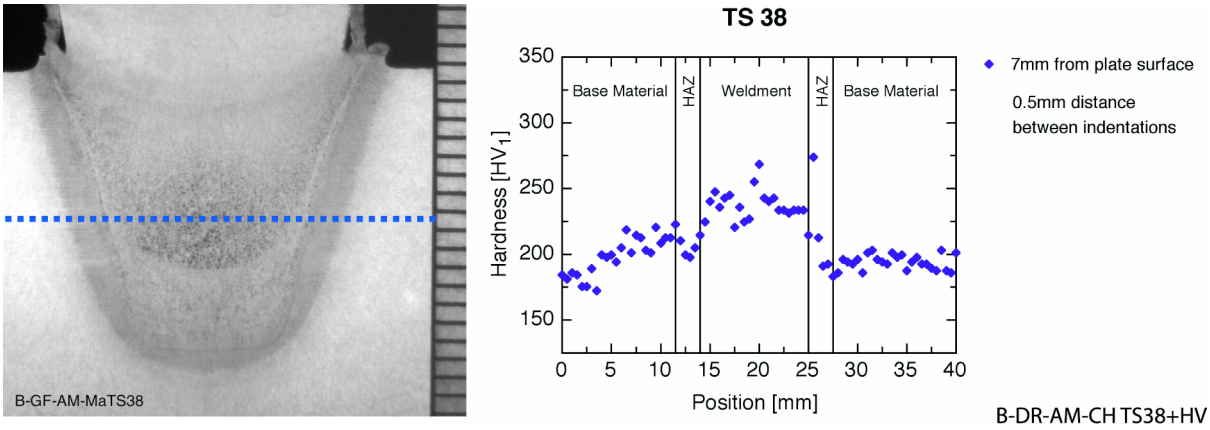

Figure 8-3: Macrograph and hardness profile of mild steel weld TS 38.

The bend specimen achieved an angle of 115° before a small crack started in the upper part of the bonding line. Charpy tests at -20° on four standard specimens with the notch in the bonding line (T-position) gave a mean value of 107 J with the minimum value at 90 J.

8.2.3 DISCUSSION

The increase in hardness in the weld material is comparably low due to the material composition and the flat temperature cycle with the tapered geometry. The thermal cycle and the process induced deformation resulted in an overmatching joint although plate and stud base materials have the same chemical composition.
The bend and Charpy tests showed that sufficient bonding to the sides could be achieved with the selected welding parameters.

8.3 MECHANICAL PROPERTIES OF STITCH WELDS IN MILD STEEL (S235)

As shown in Figure 8-2 a number of plates were produced with stitch welds for further analysis. 150 individual welds were performed according to the procedure described in chapter 8.1 above. The hole depth was 15 mm in 20 mm thick plates. Besides microstructural analysis and hardness measurements on cross sections, tensile tests and Charpy impact tests were performed. Studs were machined from base material 04, while the plates were made of base material 06 (see chapter 6.1.4 and 6.1.6).

8.3.1 MICROSTRUCTURE

The same abbreviations as in chapter 7.5.1 were used according to IIW sub-commission IX-J [138] to describe the observed microstructure.
A section of a tapered stitch sequence with four welds was examined on an optical microscope. The specimen was first cut vertically in the centre line along the weld (plane I, Figure 8-4) and later on cut horizontally for preparation of plane II (near the plate surface) and plane III at 7 mm distance to the surface.

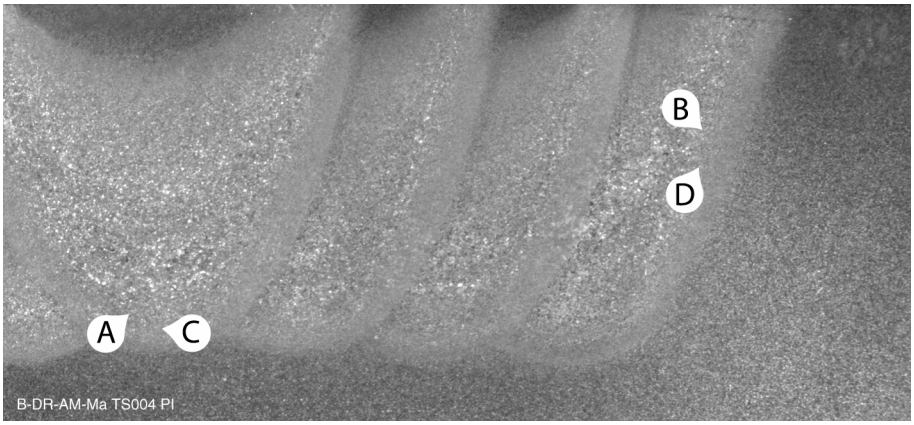

Figure 8-4: Regions of microstructural analysis on plane I (vertical in the centre of the welding path) in specimen TS-A004.

Microstructural examination of the vertical plane I revealed a martensitic structure with AC and FC in the stud material near the bonding line (Figure 8-5) at the bottom as well as to the side (Figure 8-6), while more M can be found in the bottom area due to the high cooling rates

at the beginning of the weld. The bonding line itself appears as a band of fine globular ferrite grains at the bottom area (Figure 8-7) as a result of the relative movement and the generated mechanical grain refining. Owing to the limited relative movement at the bonding line to the side, only a few fine F grains can be found (Figure 8-8), while AC and FC dominate the microstructure with few M islands.

Figure 8-5: Microstructure in region A (original magnification: 500x).

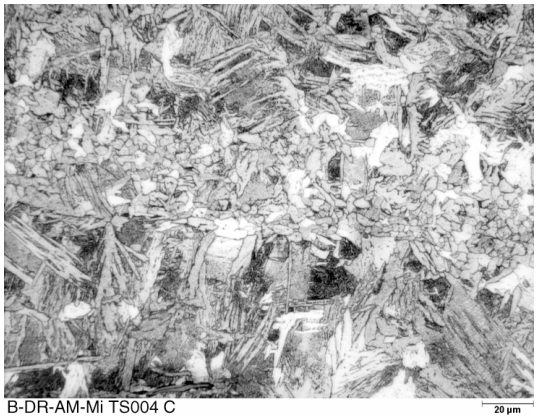

Figure 8-7: Microstructure in region C (original magnification: 500x).

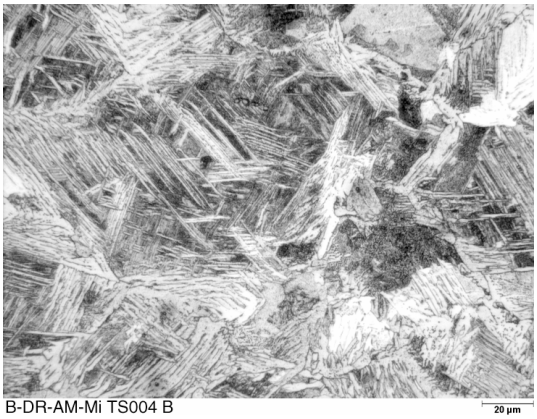

Figure 8-6: Microstructure in region B (original magnification: 500x).

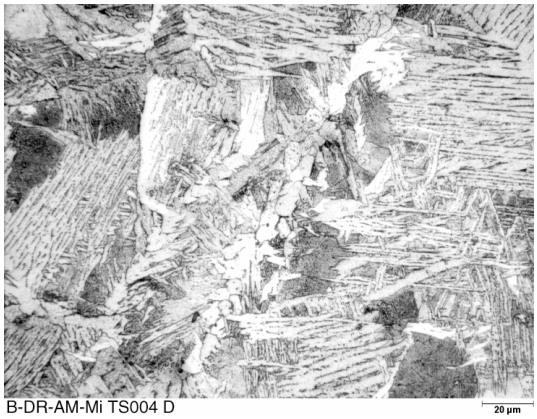

Figure 8-8: Microstructure in region D (original magnification: 500x).

In the horizontal planes II and III (Figure 8-9 and Figure 8-10) the main interest is on the change in microstructure due to the heat treatment of the following welds.

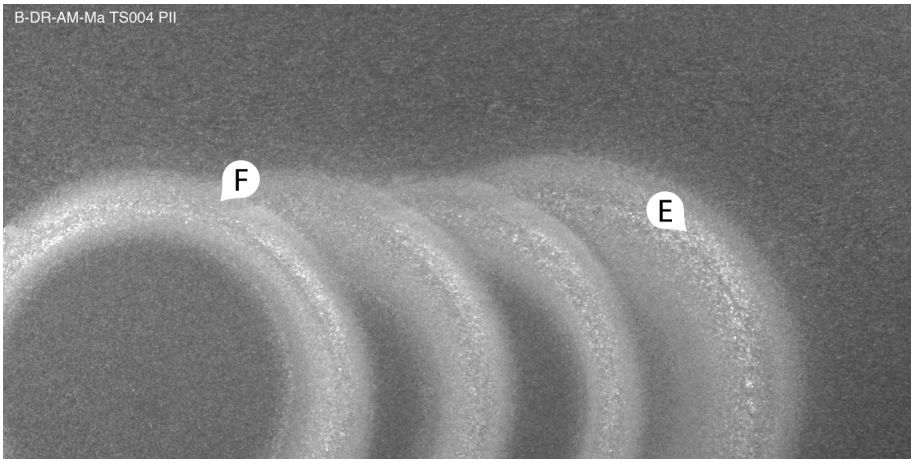

Figure 8-9: Regions of microstructural analysis on plane II (horizontal near the plate surface) in specimen TS-A004.

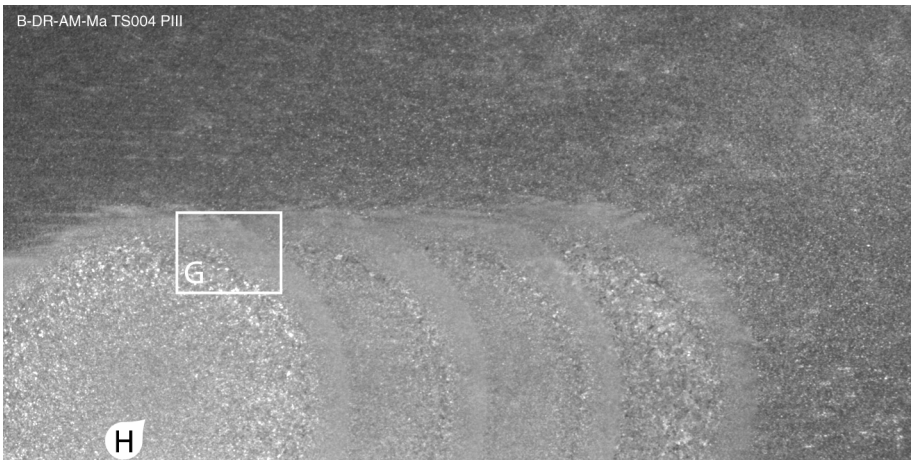

Figure 8-10: Regions of microstructural analysis on plane III (horizontal at 7 mm distance to the plate surface) in specimen TS-A004.

The primary HAZ in the base material (Figure 8-11) shows AF and AC in an F matrix as a result of heating above Ac_1 and fast cooling. If this structure is re-heated by a following weld, this secondary HAZ in the base material reveals grain growth and homogenisation (Figure 8-12). The parallel carbides in the AC decompose resulting in bigger FC and more rounded F and AF grains.

Similar transformations can be noticed in plane III in 7 mm distance to the plate surface. The main difference to plane II is that while un-affected stud material can be found in the centre of the studs in plane II, the microstructure in plane III reveals heat-treated base material in the centre of the studs (Figure 8-13). This can be found on the vertical cross section (plane I) as well. Few AF grains in Widmanstätten structure are placed in an F/FC matrix as a result of

the reasonable mild cooling conditions. It can be demonstrated, that the presented microstructure in the centre of the stud is part of the HAZ in the stud material above the final frictional plane. Figure 8-14 shows the area where the bonding line of the final weld meets the bonding line of the prior weld with the primary HAZ and the secondary re-heated HAZ in the base material. A band of finer grains along the bonding line on the stud material side is surrounded by bands of larger grains on both sides. This band depicts the plasticised stud material which is pressed in the gap between the stud and the hole walls. Figure 8-15 illustrates the microstructure and HAZs of Figure 8-14 in the interface between two welds. Common grain growth areas in the HAZs are shown in Figure 8-16 for the stud material and Figure 8-17 for the base material zone. M and AC can be found in both areas as a result of the high cooling rates leading to hardness values around 330 HV_1. The band of finer grains along the bonding line exposes no M, less AC in a matrix of mainly AF and FC, which should result in significantly lower hardness values (Figure 8-18). This area is the former gap between the stud and the hole, which is filled with plasticised stud material.
Further away from the bonding line, a fine-grained area can be found in the base material HAZ (Figure 8-19) composed of fine-grained globular F and FC.
The re-heated HAZ at plane III is similar to the one found on plane II with a homogenised matrix of AF and FC (Figure 8-20).

Figure 8-11: Microstructure in region E (original magnification: 1000x).

Figure 8-12: Microstructure in region F (original magnification: 1000x).

Figure 8-13: Microstructure in region H (original magnification: 500x).

Figure 8-16: Microstructure in region I (original magnification: 500x).

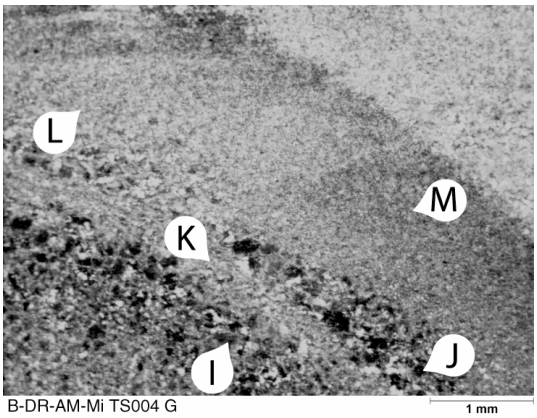

Figure 8-14: Microstructure in region G (original magnification: 20x).

Figure 8-17: Microstructure in region J (original magnification: 500x).

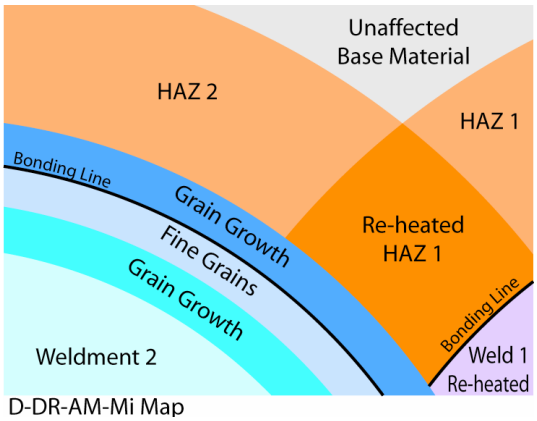

Figure 8-15: Schematic illustration of microstructure and HAZ of Figure 8-14.

Figure 8-18: Microstructure in region K (original magnification: 500x).

Figure 8-19: Microstructure in region L (original magnification: 500x).

Figure 8-20: Microstructure in region M (original magnification: 500x).

8.3.2 HARDNESS

The hardness profile (HV_1) was measured on a stitch-welding specimen as shown in Figure 8-21. Two rows, in 3.5 and 10 mm distance from the top of the plate, were produced across four welds with 0.5 mm distance between the indentations. Figure 8-21 clearly depicts the four welds in the hardness profiles with the maximum hardness values in the bonding lines. The hardness in the HAZ is highest in the last weld and decreases towards the initial welds.

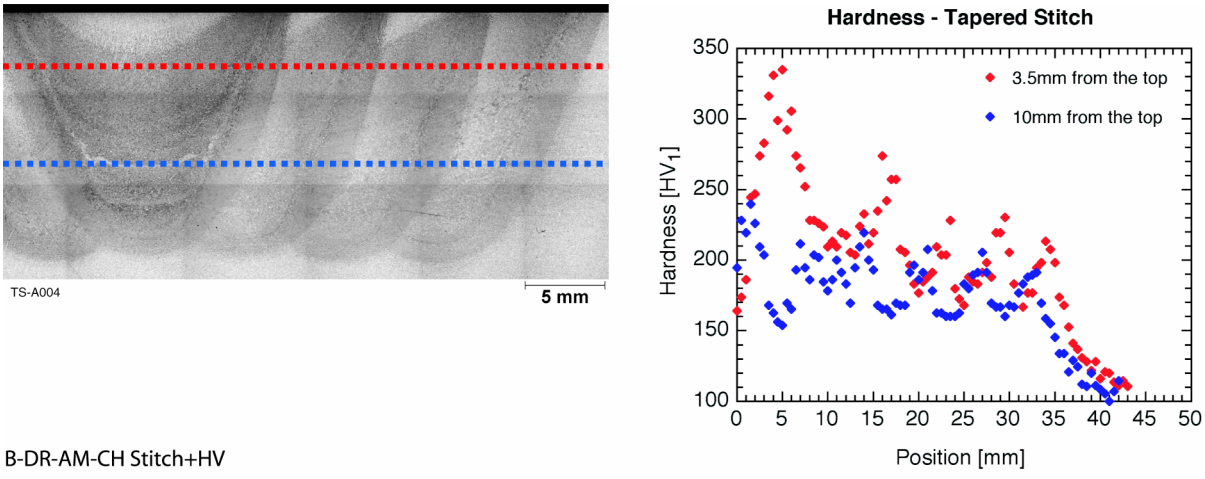

Figure 8-21: Macrograph and hardness profiles of tapered stitch welds in mild steel (DIN S235). The reduction of the maximum hardness values results from the re-heating by the following welds.

8.3.3 Tensile Strength

Full scale flat tensile tests were performed 90° to the welding direction with cross sections of 17x25 mm to establish the global properties of the stitch weld. In addition to this, micro flat tensile specimens were taken across the stitch weld to evaluate the local tensile properties.

As shown in Figure 8-22 all flat tensile specimens broke in the base material far away from the consumable stud and the HAZ. The appropriate stress-strain diagram shows the welded specimen compared to base material properties (Figure 8-23).

As in the tensile tests on single welds, the plastification concentrates on the base material areas outside the consumable stud due to the overmatching of the FHPP welds.

The micro flat tensile tests presented in Figure 8-24 show the same behaviour as known from the single FHPP welds. A clear overmatch with 600 MPa tensile strength and reduced elongation can be found in the consumable stud.

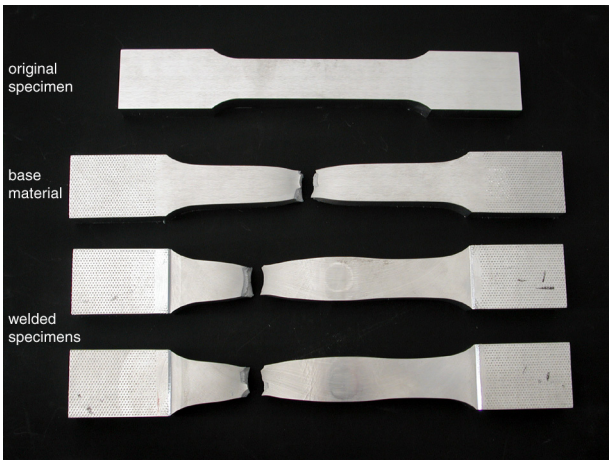

Figure 8-22: Flat tensile specimens for characterisation of stitch welds.

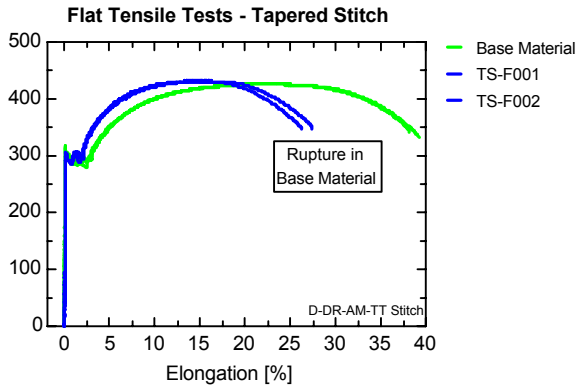

Figure 8-23: Stress-Elongation diagram for flat tensile tests in mild steel (DIN S235).

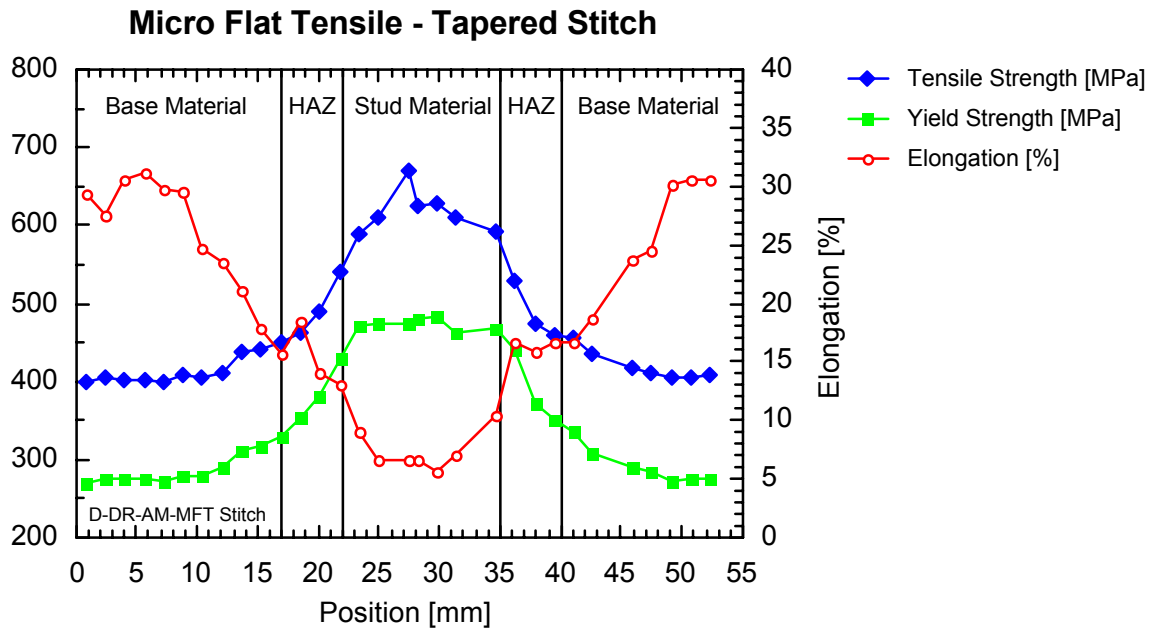

Figure 8-24: Micro flat tensile test results for tapered stitch weld in mild steel (DIN S235).

8.3.4 TOUGHNESS

The results of the Charpy impact tests compared to the base material values can be found in Figure 8-25. The notch was placed in the centre line of weld for some specimens, and in the bonding line as in the previous tests. The identification of the bonding line position was very difficult, as the bonding is curved in three-dimensions. On the one hand it has an inclination in the vertical direction and on the other hand it follows the hole shape in the horizontal direction. Hence the deviation of the measured energy absorption is relatively high. It can be seen, that both notch positions (bonding and stud material) depict a plateau between +20 °C and -10 °C, while the energy absorption in the stud area is much higher than in the bonding line.

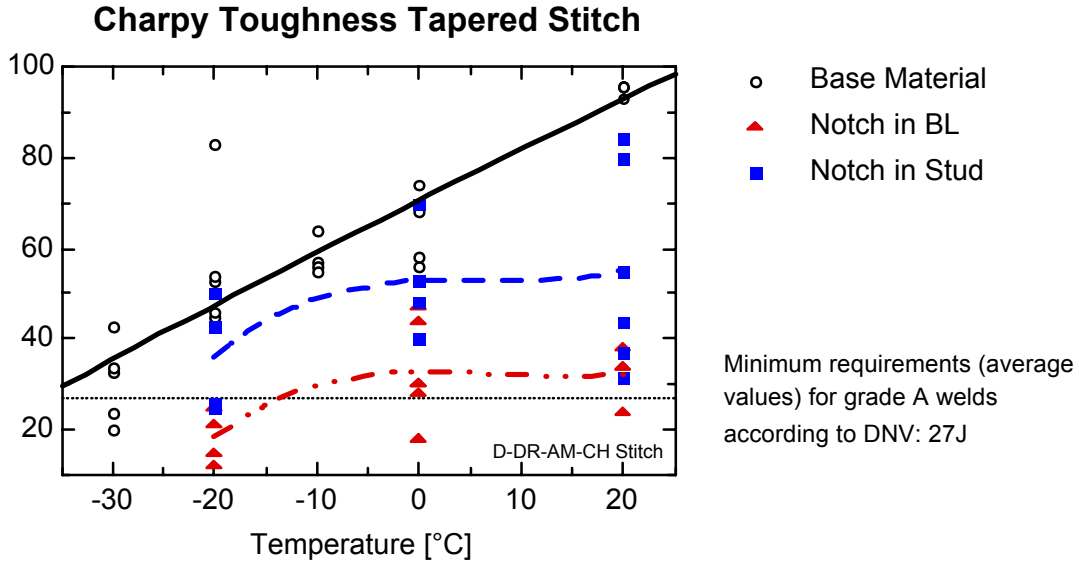

Figure 8-25: Charpy toughness values of tapered stitch welds in mild steel (DIN S235).

8.4 SUMMARY & DISCUSSION ON STITCH WELDING OF MILD STEEL (S235)

The microstructural analysis showed that the welding sequence results in a heat treatment of the former welds with significant change in the microstructure and consequently in the hardness values as well (Figure 8-21). Hardness peaks in the weld material decrease due to the homogenisation during the following welds.
Flat tensile tests revealed the same behaviour as the smaller round tensile tests in HSLA steel (chapter 7.5.3) with ultimate tensile strength values as the base material. Micro flat tensile tests across the weld show increased tensile strength values in the weld material of up to 230 MPa compared to the base material values. This illustrates the overmatch condition of the weld. Similar overmatch ratios were found in the HSLA welds presented in chapter 7.4.2. The very low elongation values measured in the weld material and the HAZ (Figure 8-24) together with the high hardness values (Figure 8-21) result in generally lower Charpy impact values. The Charpy impact test results show a wide scatter of the absorbed energy when testing the consumable stud as well as the bonding line properties. The fracture surfaces of the consumable stud specimens indicate that the Charpy test method could be applied to test consumable stud properties. The fracture surface propagates straight through the specimen starting from the notch with no visible influence of other material areas. However, the specimens with the notch in the bonding line failed very irregularly. Most of the specimens showed a fracture path deviation right at the tip of the notch with the final facture occurring somewhere away from the initial notch location. Similar behaviour was already discussed in chapter 7.6. Eckel [141] also reported fracture path deviation in toughness testing friction welds in low-alloy steel. Moreover the measured toughness values (60-80 J at 20 °C) were significantly below the base material properties with 283 J at 20 °C [141]. Eckel [141] described that identical welds and same notch positions resulted in totally different failure behaviour. Some of the specimens showed fracture path deviation, which results in testing different microstructures, while the rest of the specimens showed a straight fracture. This results in a large scatter band making it difficult to draw meaningful conclusions. Nevertheless, the current results would fulfil the classification society requirements for repair welds in ship hulls (i.e. Det Norske Veritas (DNV) [142]), as indicated in Figure 8-25. A minimum absorbed energy of 27 J is required for grade A (general constructions, i.e. ships hull) repairs. As shown in Figure 8-25 this can be guaranteed down to -10 °C, which might be sufficient for most of the applications.

It could be demonstrated that defect free FHPP welds with good mechanical properties can be produced with a portable welding system in mild steel. Moreover, the mechanical properties approved the FHPP process for the classification society requirements.
It should be emphasised that the mechanical properties of a stitch weld can be significantly improved by selecting a suitable welding sequence. The fact, that the process related re-heating of the following welds reduces the maximum hardness values should be considered when selecting the welding sequence for a given application.

9 FINAL CONCLUSIONS & DISCUSSION

The experiments carried out in this study allow the following conclusions:
Comparing the influence of the stud and hole geometries on the bonding properties, it could be clearly shown, that the hole shape has a major influence. The shape of the stud is generally of minor influence, as specially the tip is completely plasticised.
The influence of process parameters on heat generation and bonding quality is similar to that observed on conventional friction welding in most aspects. In qualitative terms the relative influence is different. The influence of the rotational speed is significantly lower in FHPP compared to conventional friction welding. Besides, the forging force, which has a major influence on the weld properties in conventional friction welding, has no influence on most of the weld in FHPP. It only affects the upper area near the surface, but cannot improve the properties in the lower area.
It could be demonstrated, that the shape of the frictional plane defines the axial force distribution and the temperature development during welding. The measurements showed, that bonding takes place at lower compression forces than estimated.
The quality of the bonding of the five geometry combinations examined was demonstrated by bend and tensile testing. All welds showed overmatching condition with failure in the base material. Single FHPP welds performed in API 5L X65 material showed sufficient toughness to fulfil the requirements of relevant codes and standards for welding of steel pipelines.
Besides the fundamental experiments on single FHPP welds in a HSLA steel, mechanical properties have been investigated for a simulated repair application in mild steel. FHPP stitch welds were performed in S235 mild steel and subjected to hardness, Charpy impact and tensile testing. The microstructural analysis revealed martensitic structures in the weld material near the bonding line, while the rest of the weld material shows acicular ferrite in a ferrite/ferrite carbide matrix. This microstructure is reflected in the measured hardness profiles . Up to 350 HV_1 could be measured near the bonding line, while the rest of the weld material shows hardness values around 200 HV_1. It was demonstrated that the welding sequence in stitch welding has a very important influence on the joint properties, as the following welds re-heat the former ones and improve the mechanical properties.
The measured tensile properties showed base material properties due to the overmatching condition of the weld material. Toughness properties have been measured which fulfil classification society requirements for marine applications.
The motivation behind this study was to perform a systematic analysis of the FHPP process to establish the possible bonding mechanisms and their influences on the microstructural and mechanical properties of single FHPP welds. Moreover, microstructural and mechanical properties of friction stitch welds in mild steel should also be determined. The experimental methodology adopted at the onset of this work and the systematic approach in which the scientific challenges of the subject matter have been addressed, proved to be successful. The results of this work have provided the basis for the industrial use of a repair technology which in many aspects provided an attractive alternative to conventional fusion welding processes.

10 RECOMMENDATIONS FOR FUTURE WORK

The recommendations for further work concentrate on the following two aspects:

1. Widening the detailed understanding and description of the process.
2. Additional investigations for a widespread application of FHPP in industry.

10.1 PROCESS

The experiments performed with the load cell system proved the significance of the applied measurement concept. This system could be used for a number of further experiments. On the one side it could be used to evaluate the influence of the holding force on the microstructural development of the consumable stud after the rotation stopped. The measurements indicated, that after a hold time of three seconds all load cells still reacted on the pressure release. An optimum duration could be established with these experiments. On the other hand, the load cell device could be used to gain first information on the residual stresses after the weld. If a reasonable high pre-load of the load cells is applied and the stud is immediately retracted after the weld without a holding time, it should be possible to measure the shrinkage of the consumable stud.

With the bonding mechanism in mind, a further investigation on the optimised stud and hole diameter relation should be performed. It might be possible to use a very narrow gap with low axial forces applied. A significant change in the force distribution might be possible as well by the use of profiled studs. The profile could be thread-like in order to apply an additional downward force on the plasticised material and by this increasing the load on the bonding surfaces.

Finally a detailed microstructural investigation of material transport could be performed to visualise the three-dimensional material flow. The concept with Nickel tracer should be further improved with smaller Nickel marker at different places in the stud. Several cross sections vertical and horizontal might then help to fully describe the material flow. Nickel tracer in the sidewalls of the hole could help to determine whether there is direct friction on the side of the hole in cylindrical geometries, or not.

10.2 APPLICATION

For a wider industrial application of the process additional information on the fatigue properties and fracture mechanics of welded joints would be needed.

Further information on the machining tolerance and surface requirements, as well as the cleanness of the hole and the stud would help to transfer the process from the experimental stage into industrial applications.

For special fields such as the offshore and marine industry the influence of the environment (i.e. water, water pressure) on the properties of the weld might be an issue as well.

11 REFERENCES

[1] Grigorian, H., I. Scherf, W.C. Yu and Ø. Christensen. *"Cost-Effective Structural Upgrade and Life Extension of Ekofisk Platforms with Use of Modern Reassessment Techniques"*. in Offshore Technology Conference. 30.4.-3.5.2001, Huston: OTC, Richardson, 2001

[2] Tebbet, L.E. *"Low Cost Jacket Repairs using new shear connection techniques"*. in International Offshore Inspection Repair and Maintenance ConferenceAberdeen, Scotland, 1988

[3] MMS, *"Assessment of Deepwater Pipeline Repair in the Gulf of Mexico"*. United States Department of the Interiour Minerals Management Service, Final Report, 2000

[4] Pope, A.M., J.C.G. Teixeira, M.P. Paes, V.R.d. Santos, D. Ros and J.R. Domingues. *"Influence of Water Depth on Microstructure and Mechanical Properties of Wet Welds"*. in The 16th International Conference on Offshore Mechanics and Arctic Engineering. 13.-17.4.1997, Yokohama, Japan: American Society of Mechanical Engineers, 1997

[5] Delauze, H.G. *"Welding in Difficult Conditions for the Offshore and Nuclear Industries"*. in IIW Conference on Welding Under Extreme Conditions. 4.-5.9.1989, Helsinki: IIW, 1989

[6] Nicholas, E.D. *"Underwater Friction Welding for Electrical Coupling of Sacrificial Anodes"*. in 16th Offshore Technology Conference. 7-9.5.1984, Houston, USA: Offshore Technology Conference, 1984

[7] Carlton, J.S., *"Marine Propellers and Propulsion"*. 1994, Oxford: Butterworth-Heinemann. (0 7506 1143 X)

[8] Miyashita, T. and H. Hino, *"Friction Welding Characteristics of TiAl intermetallic Compound"*. in Nihon-Kinzoku-Gakkai-Shi - Journal of the Japan Institute of Metals, 1994. 58(2): p. 215 - 220.

[9] Shinoda, T., K. Ito and C. Hayashi. *"Friction Welding og TiAl intermetallic compund"*. in Welding International, 1997

[10] Blakemore, G.R. *"Friction Welding - Technology for the new millennium"*. in Offshore Technology ConferenceHouston, USA, 1999

[11] Blakemore, G.R. *"Back to the future - underwater repair by friction welding"*. in Underwater Intervention 2000. 24-26.1.2000, Houston, USA, 2000

[12] Streeter, J. *"Friction Welding Underwater: a Description of the Development, Process and Future"*. in ASME, NY - 7th International Conference on Offshore Mechanics and Arctic Engineering, 1988

[13] Spindler, D.E. *"Anwendung der Reibschweißtechnik in den USA"*. in 12. Erfahrungsaustausch Reibschweißen. 4.-5.3.2002, Munich: SLV München, 2002

[14] Steve, C., *"Ramforce Portable Friction Stud Welder"*. Ramforce Services Ltd., Product Information, 1988

[15] Blakemore, G.R. *"Design and Implementation of a total control system for portable friction welding machines"*. in Computer Technology in Welding. 3-4. June 1992: TWI, 1992

[16] Thomas, W., D. Nicholas, S.B. Jones, R.H. Lilly, C.J. Dawes and R.E. Dolby, *"Friction Forming"*. TWI, Cambridge, Patent No.: EP 0 602 072 B1, 1992

[17] Meyer, A., A. Roos, J.F.d. Santos, D. Gibson, G. Blakemore and R. Hammerin. *"Subsea Robotic Friction-Welding-Repair System"*. in Offshore Technology Conference. 30.4. - 3.5.2001, Houston: OTC, 2001

[18] Meyer, A., D. Pauly, J.F.d. Santos, G. Pinheiro, A. Roos, D. Gibson and G.R. Blakemore. *"Considerations on Robotic Friction Stitch Welding for the Repair of Marine Structures"*. in 20th International Conference on Offshore Mechanics and Arctic Engineering. June 3-8, 2001, Rio de Janeiro, Brazil: The American Society of Mechanical Engineers, 2001

[19] Gibson, A., *"Robots and the end of the weld"*. in *The Daily Telegraph*. 2001.

[20] Gibson, D., A. Meyer, O. Vennemann, J.F.d. Santos and G.R. Blakemore. *"Engineering Applications of Friction Stitch Welding"*. in 20th International Conference on Offshore Mechanics and Arctic Engineering. June 3-8, 2001, Rio de Janeiro, Brazil: The American Society of Mechanical Engineers, 2001

[21] *"Friction stitch welding for subsea welded joints"*. in Offshore, 1999(November): p. 110 + 147.

[22] *"Project Information "Friction Stitch Welding Repairs of Pipelines - STITCHPIPE""*, Web Page, 12.11.1999, CORDIS Project Information, http://dbs.cordis.lu/EN_PROJI_search.html,

[23] Crossland, B., *"Friction Welding - Recommended Practices for Friction Welding"*. in Contemporary Physics, 1971. 12(6): p. 559-574.

[24] Klopstock, H. and A.R. Neeland, *"An improved Method of Joining or Welding Metals"*. Patent No.: GB-00572789, 1941

[25] Reiter, T., P. Dinsdale and D.E. Spindler. *"Reibschweißen in der Massenfertigung an Airbag-Gasgeneratoren"*. in 11. Erfahrungsaustausch Reibschweißen. 6.3.2001, Munich: SLV München, 2001

[26] AWS, *"Welding Handbook"*. 8th ed, ed. R.L. O'Brien. Vol. 2. 1991, Miami: American Welding Society. p. 955. (0-87171-354-3)

[27] Wichelhaus, G., *"Berechnung der Stoßflächentemperatur beim Reibschweißen"*. in Schweißen und Schneiden, 1975. 27(1): p. 9-10.

[28] Adam, P., *"Ablauf der Verbindungsbildung beim Schwungradreibschweißen von hochwarmfesten Legierungen - Temperaturverlauf und Wulstbildung"*. in Schweißen und Schneiden, 1979. 31(7): p. 279-283.

[29] Cheng, C.J., *"Transient temperature distribution during friction welding of two similar materials in tubular form"*. in Welding Research Supplement, 1962: p. 542s-550s.

[30] Cheng, C.J., *"Transient Temperature Distribution during Friction Welding of two dissimilar materials in tubular form"*. in Welding Journal, 1963. 42(5): p. 233s-240s.

[31] Suga, Y., S. Miyakawa and K. Ogawa, *"Estimation of temperature distribution in the friction weld of carbon steel by the finite element method"*. in Welding International, 1999. 13(4): p. 262 - 269.

[32] Spindler, D.E., *"What Industry Needs to Know about Friction Welding"*. in Welding Journal, 1994. March: p. 37-42.

[33] *"Recommended Practices for Friction Welding"*. AWS Committee on Friction Welding, Standard, ANSI/AWS C6.1-89, 1989

[34] Sergin, S.A., *"The distribution of temperature along the length of a bar in relation to the speed of rotation in the friction welding of steels"*. in Welding Production, 1977(1): p. 37-39.

[35] Smarzynski, S., *"Determination of Temperature in the Plane of Friction Welding during Welding and Forming"*. in Welding International, 1997. 11(10): p. 774-778.

[36] Knap, I. and R. Krawczyk. *"Temperature Measurement on the Interface of a Friction-Welded Joint"*. in Welding International, 2000

[37] Kreye, H. and I. Wittkamp, *"Gefügeänderung und Bindemechanismus beim Reibschweißen"*. in Zeitschrift für Metallkunde, 1977. 68(4): p. 253-259.

[38] Wang, K.K. and P. Nagappan, *"Transient Temperature Distribution in Inertia Welding of Steels"*. in Welding Journal, 1970. 49(9): p. 419s-426s.

[39] DVS, *"Merkblatt DVS 2909, Teil1, Reibschweißen von metallischen Werkstoffen"*. Deutscher Verband für Schweißtechnik e.V., 1989

[40] *"Radial friction welding machine developed for offshore pipelaying"*. in Pipe Line Industry, 1984. July: p. 36-37.

[41] Dunkerton, S.B., A. Johansen and S. Frich, *"Radial friction welding for offshore pipelines"*. in Welding Journal, 1987(July): p. 40 -47.

[42] Leeuwen, W.H.v. and S. Frich. *"Mechanised ultrasonic inspection of radial friction welds"*. in 3rd International Conference "Welding Performance of Pipelines". 18-21 November 1986, London, 1986

[43] Nicholas, E.D., *"Radial Friction Welding"*. in Welding Journal, 1983(July): p. 17-29.

[44] Torster, F., J.F.d. Santos, G. Hutt and M. Koçak. *"Metallurgical and Mechanical Properties of Radial Friction Welded Ti-6Al-4V-0.1Ru Risers"*. in 17th International Conference on Offshore Mechanics and Arctic Engineering. July 5-9, Lisbon, Portugal: The American Society of Mechanical Engineers (ASME), 1998

[45] Appel, L. *"Untersuchungen zum Linearreibschweißen von Metallen"*, Web Page, 3. April, http://www.slv-muenchen.de/fue/veroeff.htm, 2001

[46] Nicholas, E.D. *"Friction surfacing and linear friction welding"*. in 24th International SAMPE Technical Conference, Advanced Materials: meeting the economic challenge. 1992, Toronto, 1992

[47] Nicholas, E.D. and W.M. Thomas, *"Review of friction processes for aerospace applications"*. in International journal of materials & product technology, 1998. 13(1/2): p. 45 - 55.

[48] Vairis, A., *"High Frequency Linear Friction Welding of a Titanium-Alloy"*. in Wear, 1998. 217(1): p. 117-131.

[49] Vairis, A. and M. Frost, *"On the extrusion stage of linear friction welding of Ti 6Al 4V"*. in Materials Science and Engineering, 1999. A271: p. 477-484.

[50] *"Leading Edge - Friction Surfacing Advances"*. in TWI Connect, 1991(March).

[51] Batchelor, A.W., S. Jana, C.P. Koh and C.S. Tan, *"The effect of metal type and multi-layering on friction surfacing"*. in Journal of materials processing technology, 1996. 57(12): p. 172-181.

[52] Bedford, G.M. and P.J. Richards. *"On the absence of dilution in friction surfacing and lateral friction welding"*. in International Conference on Surface Engineering. 1986: TWI, 1986

[53] Bedford, G.M., *"Friction surfacing for wear applications"*. in Metals and Materials, 1990. 6(11): p. 702-705.

[54] Bedford, G.M., *"Friction Surfacing a Rotating Hard Metal Facing Material onto a Substrate Material with the Benefit of Positively Cooling the Substrate"*. Frictec Limited, UK, Patent No.: 5,077,081, 1991

[55] Chandrasekaran, M., A.W. Batchelor and S. Jana, *"Study of Interfacial Phenomena During Friction Surfacing of Aluminium with Steels"*. in Journal of Materials Science, 1997. 32(22): p. 6055 - 6062.

[56] Chandrasekaran, M., A.W. Batchelor and S. Jana, *"Friction Surfacing of metal coatings on steel and aluminium substrate"*. in Journal of Materials Processing Technology, 1997. 72(3): p. 446 - 452.

[57] Chandrasekaran, M., A.W. Batchelor and S. Jana, *"Study of Interfacial Phenomena During Friction Surfacing of Mild Steel with Tool Steel and Inconel"*. in Journal of Materials Science, 1998. 33(10): p. 2709 - 2717.

[58] Irving, B., *"Sparks begin to fly in Nonconventional Friction Welding and Surfacing"*. in Welding Journal, 1993. 72(5): p. 37 - 40.

[59] Jenkins, B.M. and E.D. Doyle, *"Hardfacing by low pressure friction surfacing"*. in Transactions of the Institution of Engineers, Australia, 1989. 14(3): p. 178 - 185.

[60] Kalken, A.M.v., *"Friction Surfacing of Stainless Steel on Mild Steel with a Robot".* MSc, Delft University of Technology, Laboratory of Material Science and Engineering, 2001

[61] Kallee, S., *"Leading Edge - Friction seam welding"*. in TWI Connect, 1996(April).

[62] Lambrineas, P. and P. Hewsbury, *"Areal coverage using friction surfacing"*. in Journal of Ship Production, 1992. 8(3): p. 131 - 136.

[63] Li, J.Q. and T. Shinoda, *"Underwater friction surfacing"*. in Surface Engineering, 2000. 16(1): p. 31-35.

[64] Li, J.Q. and T. Shinoda, *"Eigenschaften reibauftraggeschweißer Scheidenkanten"*. in Schweissen & Schneiden, 2000. 52(5): p. 278-281.

[65] Nicholas, E.D., *"Friction Surfacing"*, in *ASM Handbook*. 1993. p. 321 - 323.

[66] Shinoda, T., O. Okamoto, S. Takemoto, Y. Katoh and T. Shimizu, *"Deposition of hard coating layer by friction surfacing"*. in Yosetsu-gakkai-ronbunshu / Quarterly journal of the Japan Welding Society, 1995. 13(3): p. 432 - 437.

[67] Shinoda, T., J.Q. Li, Y. Katoh and T. Yashiro, *"Effect of process parameters during friction coating on properties of non-dilution coating layers"*. in Surface Engineering, 1998. 14(3): p. 211-216.

[68] Shinoda, T., Y. Mizung, J.Q. Li and T. Saito, *"Friction Welding Phenomena in Aluminium"*. in Welding International, 2000. 14(6): p. 425-430.

[69] Thomas, W.M. *"An Introduction to Friction Surfacing"*. in The First International Conference on Surface Engineering. 25-28 Jan., Brighton, 1985

[70] Bedford, G.M. and P.J. Richards. *"Recent developments in friction coating"*. in Repair and Reclamation Conference. Sept 1984, 1984

[71] Strombeck, A.v. *"Bruchmechanische Untersuchungen an reibrührgeschweißten Aluminiumlegierungen"*. in Werkstoffwoche 1998. 12.-15.10.1998, München, 1998

[72] Strombeck, A.v., *"Bewertung von Friction Stir Welding geschweißten Verbindungen von Al-Legierungen".* GKSS Forschungszentrum, 1998

[73] Strombeck, A.v., J.F.d. Santos, F. Torster, P. Laureano and M. Kocak. *"Fracture toughness behaviour of FSW joints on aluminium alloys"*. in 1st International Symposium on Friction Stir WeldingCalifornia, USA, 1999

[74] Schilling, C., *"Einsatz von Friction Stir Welding zum Schweißen von Kraftfahrzeugstrukturen"*. GKSS Forschungszentrum, Internal Report, 1999

[75] Strombeck, A.v., *"Verfahrens- und Werkzeugentwicklung zur Umsetzung und Anwendung des Friction-Stir Welding Verfahrens mit einem Roboter"*. GKSS Forschungszentrum, Internal Report, 1999

[76] Strombeck, A.v., C. Schilling and J.F.d. Santos. *"Robotic Friction Stir Welding - Tool Technology and Applications"*. in 2nd International Symposium on FSWGothemburg, 2000

[77] DVS, *"Merkblatt DVS 2909, Teil2, Reibschweißen von metallischen Werkstoffen"*. Deutscher Verband für Schweißtechnik e.V., 1993

[78] DVS, *"Merkblatt DVS 2909, Teil3, Reibschweißen von metallischen Werkstoffen"*. Deutscher Verband für Schweißtechnik e.V., 1994

[79] Vill, V.I., *"Friction Welding of Metals"*, ed. I.P. Baykova. 1962, New York: American Welding Society, Inc.

[80] ASM, *"Welding Handbook"*. Vol. 06. 1993, USA: American Society of Metals.

[81] Neumann, A. and D. Schober, *"Reibschweißen von Metallen"*. 1 ed. 1991, Berlin: Verlag Technik GmbH. (3-341-00904-3)

[82] Pauly, D., *"Process development on an experimental Friction Hydro Pillar Processing system"*. GKSS Forschungszentrum, Internal Report, 1999

[83] Böhme, D. and F.D. Hermann, *"Handbuch der Schweißverfahren Teil II: Autogentechnik, Thermisches Schneiden, Elektronen -/ Laserstrahlschweißen, Reib -, Ultraschall - und Diffusionsschweißen"*. 1992, Düsseldorf: DVS - Verlag.

[84] Nentwig, A.W.E., W. Welt and H.M. Tensi, *"Analyse des Reibschweißablaufes beim Rotationsreibschweißen von metallischen Werkstoffen gleicher und unterschiedlicher Warmfestigkeit"*. in DVS Berichte, 1991(139): p. 10-14.

[85] Ellis, C.R.G., *"Continuous Drive Friction Welding of Mild Steel"*. in Welding Journal, 1972(April): p. 183s-197s.

[86] Bethlehem, W., *"Schmelzpunkt wurde nicht erreicht"*. in Schweißen und Schneiden, 1984. 36(10): p. 479-483.

[87] Eichhorn, F., *"Beitrag zu den Vorgängen an der Verbindungsstelle beim konventionellen Reibschweißen von Stahl"*. in Schweißen und Schneiden, 1968. 20(11): p. 563-570.

[88] Wichelhaus, G., *"Messen der Stoßflächentemperatur beim Reibschweißen"*. in Schweißen und Schneiden, 1974. 26(3): p. 97-100.

[89] Kreye, H. *"Verbindungsbildung beim Reibschweißen"*. in 2. Aachener Reibschweiß-Kolloquium. 10. + 11.3.1982, Aachen, 1982

[90] Schaefer, R., *"Beitrag zum Reibschweißen von Metallen unter besonderer Berücksichtigung der Energieumwandlung während des Schweißprozesses"*. 1971, Aachen.

[91] Bethlehem, W., *"Geeignet zur Prozeßüberwachung: Störungen des Momentenverlaufs lassen fehlerhafte Reibschweißungen erkennen"*. in Schweißen und Schneiden, 1984. 36(1): p. 23-28.

[92] Vill, V.I., *"Friction Welding"*. in Welding production, 1959. 10: p. 31-41.

[93] Futamata, M. and A. Fuji, *"Friction Welding of Titanium and SUS 304L Austenitic Stainless Steel"*. in Welding International, 1990. 4(10): p. 768-774.

[94] AWS, *"Welding Handbook"*. 7th ed. Engineering, Costs, Quality, and Safety. Vol. 5. 1984, Miami: American Welding Society.

[95] Grewe, K.J., *"Friction Welding Takes On New Applications"*. in Welding Journal, 1997. Sep: p. 39-40.

[96] Grünauer, H., *"Reibschweißen von Metallen"*. 1987: expert Verlag. (3-8169-0117-4)

[97] Dennin, G., *"Optimierung von Einstellwerten für das Reibschweißen mit kontinuierlichem Antrieb"*. in Schweißen und Schneiden, 1979. 31(7): p. 283-289.

[98] Mazac, K. *"Parameterfindung und Parameterüberwachung beim Reibschweißen"*. in 10. Erfahrungsaustausch Reibschweißen. 29.3.2000, Munich, Germany: SLV München, 2000

[99] Voinov, V.G., *"Mechanism of Joint Formation in Friction Welding"*. in Welding Production, 1968. 15: p. 8-13.

[100] Lucas, W., *"Process Parameters and Friction Welds"*. in Metal Construction and British Welding Journal, 1973. 5(8): p. 293-297.

[101] Petrucci, L.G., *"Temperature distribution in friction welding"*. in General Engineer, 1978(July & August): p. 178-184.

[102] Lebedev, V.K. and I.A. Chernenko, *"Friction Welding"*. 1992, USA: Harwood Academic Publishers GmbH.

[103] Eberhard, B.J., B.W. Schaaf, JR. and A.D. Wilson, *"Friction weld ductility and toughness as influence by inclusion morphology"*. in Welding journal, 1983. 1983(july): p. 171-s - 178-s.

[104] Manteghi, S., *"Some fatigue tests on friction welded steel bars"*. TWI, 485/1994, 1994

[105] *"Schweißen - Reibschweißen von metallischen Werkstoffen"*. European Committee for Standardization, Standard, DIN EN ISO 15620, 2000

[106] Bhole, S.D., *"Interface Properties in Friction Welding - Technical Note"*. in Welding Journal, 1991(July): p. 168s-170s.

[107] Weiss, R., *"Residual Stresses and Strength of Friction Welded Ceramic/Metal Joints"*. in Welding Journal, 1998(March): p. 115s-122s.

[108] Weiss, R. and F. Sassani, *"Strength of Friction Welded Ceramic-Metal Joints"*. in Material Science and Technology, 1998. 14(6): p. 554-560.

[109] Baeslack, W.A., *"ASM Handbook, Vol. 6, Welding, Brazing, and Soldering"*, ed. D.L. Olson. Vol. 6. 1995: ASM. 507-523. (0-87170-382-3)

[110] Blakemore, G.R. *"Friction Welding on Live Pipelines"*. in Pipeline Technology: Elsevier Science B.V., 1995

[111] Nicholas, E.D. *"Friction Welding Under Water"*, 1984

[112] Nicholas, E.D. *"Friction Hydro Pillar Processing"*. in 11th Annual North American Welding Research Conference. 7-9.11.95, 1995

[113] Andrews, R.E., *"Underwater repair by friction stitch welding"*. in Metals and Materials, 1990(Dec): p. 796-797.

[114] Thomas, W. and D. Nicholas, *"Friction Hydro Pillar Processing (FHPP)"*. in TWI Connect, 1992(June).

[115] Thomas, W., *"The need for gas shielding - positive advantages for two friction processes"*. in TWI Bulletin, 1997(Sep/Oct): p. 84-88.

[116] dos Santos, J.F., A.v. Strombeck and C. Schilling. *"Reibrührschweißen Verfahren und Stand der Technik"*. in 2. GKSS Workshop - Reibrührschweißen. 22-23.01.02, Geesthacht, Deutschland: RIFTEC/GKSS, 2002

[117] dos Santos, J.F., A.v. Strombeck, C. Schilling, M. Kocak and F. Torster, *"Fracture toughness characterization of electon beam and friction stir welded Al-Alloys"*.

[118] Strombeck, A.v., Schilling, C., dos Santos, J.F. *"Robotic Friction Stir Welding"*. in 2. GKSS Workshop - Reibrührschweißen (Friction Stir Welding). 22.-23.01.02, Geesthacht, Deutschland: RIFTEC/GKSS, 2002

[119] Blakemore, G., *"Friction Stud Welding in Hazardous Areas"*. in Welding & Metal Fabrication, 1993(Nov/Dec): p. 429-430.

[120] Shinoda, T., H. Endo and K. Kato, *"Friction welding of cast iron and stainless steels"*. in Welding International, 1999. 13(2): p. 89-95.

[121] Thomas, W. and D. Nicholas, *"Leading Edge - FHPP"*. in TWI Connect, 1992(June).

[122] Thomas, W. and D. Nicholas, *"On trial - a new thick plate joining technique"*. in TWI Connect, 1993(April).

[123] Gibson, D., Personal Communication, 1997-2001, Aberdeen

[124] Blakemore, G.R. *"Applications of State of the Art Portable Friction Welding Equipment"*. in EUROJOIN 2. 16/18 May 1994, Florence, Italy, 1994

[125] Nentwig, A. and A. Jenicek, *"Research into the Possible Applications of Friction Stud Welding"*. in Welding Research Abroad, 1996. 42(2): p. 36-40.

[126] Moldskred, S. and J.F.d. Santos. *"Friction Stitch Welding Repair of Cracks in Ships, Offshore Steel Structures and Nuclear Power Stations"*. in 7nd ECNDT ConferenceCopenhagen, 1998

[127] Blakemore, S., *"ROV Deployment of a Hydraulic Friction Stud Welding Machine"*. Hydro Marine Systems, Case Study,

[128] Blakemore, G.R. *"Underwater Application of State of the Art Portable Friction Stud Welding Equipment"*. in International Workshop on Underwater Welding of Marine Structures. December 7-9, New Orleans, Louisiana, USA: American Bureau of Shipping, 1994

[129] *"Härteprüfung, Teil 2: Mikrohärteprüfung an Schweißverbindungen"*. European Committee for Standardization, Standard, DIN EN 1043-2, 1996

[130] *"Biegeprüfungen"*. European Committee for Standardization, Standard, DIN EN 910, 1996

[131] *"Specification for Underwater Welding"*. American Welding Society / American National Standards Institute, Standard, AWS D3.6M:1999, 1999

[132] *"Querzugversuch"*. European Committee for Standardization, Standard, DIN EN 895, 1999

[133] *"Zugproben"*. European Committee for Standardization, Standard, DIN EN 10 002, 1991

[134] *"Kerbschlagbiegeversuch"*. European Committee for Standardization, Standard, DIN EN 875, 1995

[135] *"Kerbschlagbiegeversuch nach Charpy"*. European Committee for Standardization, Standard, DIN EN 10 045, 1990

[136] Çam, G., S. Riekehr and M. Koçak. *"Determination of Mechanical Properties of Laser Welded Steel Joints with Microtensile Specimens"*. in ASM International European Conference on Welding and Joining Science and Technology. 10.-12.03.1997, Madrid: ASM International, 1997

[137] *"Konstantmotor A2FM"*. Mannesmann Rexroth - Brueninghaus Hydromatik GmbH, Product Documentation, RD 91001/01.97, 1997

[138] *"Compendium of Weld Metal Microstructures and Properties"*, ed. R.E. Dolby. 1985, Cambridge: The Welding Institute. (0 85300185 5)

[139] *"Specification for Welding of Steel Pipelines on Land and Offshore - Part 1: Carbon and Carbon Manganese Steel Pipelines"*. British Standard Institution, British Standard, BS 4515-1:2000, 2000

[140] Shternin, L.A., *"The calculation of temperature distribution in friction welding"*. in Welding Production, 1966. 13(3): p. 11-14.

[141] Eckel, C. *"Zähigkeit von Reibschweißverbindungen"*. in Schweißtechnische Perspektiven, DVS Report 120. 20.+21.6.1989, Braunschweig: DVS-Verlag, 1989

[142] *"Rules for Classification of Ships - Newbuildings, Materials and Welding"*. Det Norske Veritas, Standard, 1996